UNIVERSITY OF SOUTHAMPTON

Faculty of Engineering, Science and Mathematics

Institute of Sound and Vibration Research

Measurements of Sub-Surface Bubble Populations and the Modelling of Air-Sea Gas Flux

David Geoffrey Halstaff Coles

Thesis for the degree of Doctor of Philosophy

March 2010

UNIVERSITY OF SOUTHAMPTON

ABSTRACT

FACULTY OF ENGINEERING, SCIENCE AND MATHEMATICS
INSTITUTE OF SOUND AND VIBRATION RESEARCH

Doctor of Philosophy

MEASUREMENTS OF SUB-SURFACE BUBBLE POPULATIONS AND THE MODELLING OF AIR-SEA GAS FLUX

by David Geoffrey Halstaff Coles

Bubbles, formed by breaking waves, play an important role in the transfer of gases between the Earth's oceans and atmosphere and have been shown to increase the flux of gases during periods of heightened sea state. Having been formed, these bubble clouds evolve through the effects of buoyancy, gas exsolution and dissolution, and the fragmentation and coalescence of bubbles. A number of experimenters have successfully measured sub-surface bubble clouds using a variety of acoustic and optical techniques, although data over a wider range of bubble radii are required for fuller comparison with models of how these clouds evolve and contribute to air-sea transfers of mass, momentum and energy. This study details the design of an acoustic system deployed on an 11 metre spar buoy during two sea trials in the Atlantic Ocean. Through the measurement of the additional attenuation due to bubbles, bubble size distributions were inferred over the broadest range of bubble radii ever measured using active acoustics in the open ocean. The volumetric backscatter strength from the bubble clouds were also measured to gain a profile of these bubble populations. A gas transfer model was then developed, with the measured data used as an input to calculate the associated fluxes. With this method, bubble-mediated transfer velocities and equilibrium supersaturations were found for the first time based on experimental work. These parameters aid the characterisation of air-sea gas transfer and therefore help improve the accuracy of existing climate models.

Contents

List of Figures

List of symbols

A	acoustic attenuation in decibels per unit length
A_1	amplitude of plane wave
A_{excess}	excess attenuation due to bubbles
A_{i}	attenuation measured in the i^{th} position
A_{IES}	raw inverted echo sounder amplitude
A_{s}	surface area of a sphere
A_{uncert}	uncertainty in attenuation value
B	bulk modulus
B_{c}	bulk modulus of the bubble cloud
B_{g}	bulk modulus of gas within a bubble cloud
B_{j}	linear B-splines
B_{w}	bulk modulus of water within a bubble cloud
c_{c}	speed of sound in a bubble cloud
c_{w}	speed of sound in water
C_{a}	concentration of gas in air
C_{bub}	concentration of gas in a bubble
C_{w}	concentration of gas in water
ΔC	concentration difference
D_{g}	thermal diffusivity
D_{mol}	molecular diffusivity
e_{I}	error associated with inversion solution
$\mathbf{e}_{\text{k}}$	unit vector in the direction of propagation
e	base of the natural logarithms (2.71828)

f	frequency
f_{frac}	fraction of gas in dry air
f_{fact}	scaling factor
Δf_{nb}	component of n^{th} resonance width due to bubbles
f_{i}	imaging frequency
f_{no}	width of n^{th} resonance in bubble free water
f_{p}	pump frequency
F	air-sea gas flux
$F_{1000,\mathrm{N}}$	gas flux of nitrogen associated with an input of 1000 bubbles
F_{b}	air-sea gas flux associated with bubbles
$F_{\mathrm{b}}^{\mathrm{N}}$	air-sea gas flux of nitrogen associated with bubbles
g	gravitational acceleration
g_1	scattering strength
H	Henry's Law constant
H_{s}	significant wave height
i	imaginary constant ($i = \sqrt{-1}$)
i	integer
I	number of bubbles in volume element
$\mathbf{I}_0$	identity matrix
I_{b}	intensity of acoustic beam
j	integer
J	number of discrete radius bins
$J_{\mathrm{bub,i}}$	flux of gas into a bubble
k	wavenumber
k_{c}	wavenumber for bubble cloud
k_{L}	vertical repetition length of Langmuir cells
K	inversion kernel matrix
K_{ab}	absorption coefficient
K_{b}	bubble-mediated gas transfer velocity
K_{cal}	calibration factor for inverted echo sounder
K_{o}	direct gas transfer velocity

K_{T}	total gas transfer velocity
K_{v}	turbulent diffusion coefficient
$K_{\mathrm{v}}^{\mathrm{z}}$	depth dependent turbulent diffusion coefficient
K_{w}	transfer velocity of gases in the water phase
l_{D}	thickness of thermal boundary layer
l_{L}	horizontal repetition length of Langmuir cells
n^0	zeroth-order bubble density
n_{b}	number of bubbles per unit volume
n_{j}	total number of bubbles per unit volume in the j^{th} bin
$n^0(R_{\mathrm{n}})$	zeroth-order bubble density at frequency f_{n}
N_{j}	total number of bubbles in each radius bin
Nu	Nusselt number
p	pressure
p_0	hydrostatic liquid pressure outside the bubble
p_{atm}	atmospheric pressure
p_{bub}	pressure in a bubble
p_{l}	driving pressure per unit volume
p_{L}	liquid pressure at the bubble interface
p_{nb}	n^{th} resonance height in the presence of bubbles
p_{no}	n^{th} resonance height without bubbles
p_{p}	partial pressure
$p_{\mathrm{p,w}}$	partial pressure of a gas in water
p_{v}	vapour pressure
P	pressure at the position occupied by the bubble if the bubble were absent
P_{+}	pressure amplitude at the sum frequency
$P_{\mathrm{alt_base,i}}$	alternative baseline value at the i^{th} hydrophone
$P_{\mathrm{alt_base,i+1}}$	alternative baseline value at the $i^{\mathrm{th}}+1$ hydrophone
P_{A}	amplitude of driving pressure
P_{base}	baseline pressure for excess attenuation
$P_{\mathrm{base,i}}$	baseline pressure for the i^{th} hydrophone
$P_{\mathrm{base,i+1}}$	baseline pressure for the $i^{\mathrm{th}}+1$ hydrophone

$P_{\mathrm{b-s}}$	backscattered pressure at the receiver
P_{i}	pressure at the imaging frequency
$P_{\mathrm{m-rat}}$	ratio of measured pressures
P_{meas}	pressure measured at hydrophone
$P_{\mathrm{meas,i}}$	pressure measured at the i^{th} hydrophone
$P_{\mathrm{meas,i+1}}$	pressure measured at the $i^{\mathrm{th}} + 1$ hydrophone
P_{p}	pressure at the pump frequency
P_{pi}	pressure of the incident wave at the receiver
Pe	Peclet number
r	distance
R	instantaneous bubble radius
R_{g}	universal gas constant
R_0	equilibrium bubble radius
Re	Reynolds number
s_{e}	extinction cross section per unit volume
s_{v}	volumetric backscatter strength per unit volume
$s_{\mathrm{v,ref}}$	reference value for volumetric backscatter strength
S	solubility
S_{v}	volumetric backscatter strength per unit volume in decibels
$S_{\mathrm{v,K}}$	volumetric backscatter strength before calibration factor is applied
t	time
T	temperature
T_{z}	wave period
u	real part of the complex ratio of sound speeds
U	insonified volume
$\mathbf{U}$	orthonormal matrix
v	imaginary part of the complex ratio of sound speeds
v_0	prescribed velocity related to the turbulent diffusion coefficient
v_{k}	kinematic viscosity
V	volume
$\mathbf{V}$	orthonormal matrix

V_c	volume occupied by a bubble cloud
V_L	maximum downwelling/upwelling velocity of Langmuir cell
V_w	volume of water within a bubble cloud
V_g	volume of gas within a bubble cloud
w_b	bubble rise velocity
$\langle W \rangle$	time averaged power
$\mathbf{W}$	diagonal matrix containing singular values of $\mathbf{K}$
W_{10}	wind speed corrected to 10 metres
W_c	whitecap coverage
x	distance in x direction
x_m	mole fraction
x_V	voltage per unit pressure
y	distance in y direction
z	depth
α	acoustic property representing attenuation and phase speed
α_ab	acoustic absorption
α_E	exact attenuation, without noise
β	regularisation parameter
β_tot	total damping constant
β_th	thermal damping constant
β_vis	viscous damping constant
β_rad	radiation damping constant
δ	equilibrium supersaturation
δ_D	damping constant
δ_n	noise on an attenuation measurement
δ_R	logarithmic decrement of a bubble's resonance decay divided by π
Δ_0	combined equilibrium supersaturation for air-sea gas flux
η	shear viscosity
$\mathcal{F}$	value proportional to the energy flux per unit area
$\mathcal{F}_0$	value proportional to the energy flux per unit area in the incident wave

$\mathcal{F}_{\text{tot}}$	value proportional to the total energy flux
γ	ratio of specific heats
κ	polytropic index
ω	angular frequency
ω_0	bubble resonant frequency
ω_{p}	angular frequency of pump signal
$\Omega_{\text{b-s}}$	backscattering cross section
Ω_{e}	extinction cross section
$\Omega_{\text{e}}^{\text{res}}$	resonance value of the extinction cross section
$\Omega_{\text{e}}^{\text{c}}$	extinction cross section for a bubble cloud
Ω_{scat}	scattering cross section
ϕ_{sat}	saturation of gas
ψ	acoustic field
ψ_0	plane wave function
ψ_{s}	part of acoustic field resulting from a scatterer
Ψ	bubble size distribution function
Ψ_{L}	Langmuir stream function
Ψ_{opt}	optimal solution for the bubble size distribution
ρ_{c}	density of the bubble cloud
ρ_{g}	density of gas
ρ_{w}	density of water
σ	surface tension
τ	pulse duration
φ	equivalent solid angle
ξ_{c}	representation of sound speed in bubble cloud
ξ_{cl}	representation of sound speed per unit volume in bubble cloud
ζ_{ccf}	composite cost function

DECLARATION OF AUTHORSHIP

I, ...,
declare that the thesis entitled '*Measurements of Sub-Surface Bubble Populations and the Modelling of Air-Sea Gas Flux* ' and the work presented in the thesis are both my own, and have been generated by me as the results of my own original research. I confirm that:

- this work was done wholly or mainly while in candidature for a research degree at his University;
- where any part of this thesis has previously been submitted for a degree or any other qualification at this University or any other institution, this has been clearly stated;
- where I have consulted the published work of others, this is always attributed
- where I have quoted from the work of others, the source is always given. With the exception of such quotations, this thesis is entirely my own work;
- I have acknowledged all main sources of help;
- where the thesis is based on work done by myself jointly with others, I have made clear exactly what was done by others and what I have contributed myself;
- none of this work has been published before submission.

Signed: .....
Date: .....

Acknowledgements

My greatest thanks goes to God who is so amazing in the way that He cares about me and sustains me. Thank you God! I couldn't do it without you.

My supervisor, Professor Tim Leighton, has been a fountain of knowledge and wisdom and I really appreciate his input into the work I've been doing. I've also enjoyed his cringey jokes and the '2001: A Space Odyssey' quotes, and it's been great getting to know him more and see the amazing love he has for his family.

My secondary supervisors, Dr David Woolf and Dr Meric Srokosz, have always been ready to answer any questions I had for them even though they have at times been geographically distant, so thank you to them. I especially appreciate the guidance Dr Woolf has given me through the gas modelling stage.

I want to thank Robin Pascal, Dan Comben, Ben Moat and Margaret Yelland for all the work they've done on the buoy (they've all done so much) and generally being flexible when it came to the many re-tests of the buoy in the docks. It was a pleasure to work with them all.

It's been a real pleasure working with Paul Doust on the technical elements of transducer matching and power amplification. His work ethic is impressive and his attention to detail inspiring. He achieved what at first sight might have seemed impossible.

The ISVR technicians, Ant, Alan, Andy and Rob, have been a great help over the past couple of years. It's been so useful being able to chat to them about ideas and they've always managed to produce, even when the

timescales have been very short!

My colleagues have made a real difference to my sanity in the midst of all the hard work. Chris Powles has been an immense help with so many tricky mathematical problems. Working in the tank with Dan Finfer was one of the highlights of the last 3 years - we had some good times, thanks so much Dan. I want to thank all the others who helped me at various times in the tank - Geun-Tae Yim, Martin Cooling and Ping-Chang Hsueh, who was also very helpful on the ship.

My thanks goes to Prof. Paul White and Dr Gary Robb for their invaluable help with the MATLAB® inversion code. It made such a difference to have some working code so early on in the project to experiment with.

This research was carried out under NERC Grant NE/C001834/1 and none of this could have happened without that funding so I am very grateful to the Natural Environment Research Council for that. I'd especially like to thank the coordinators of the two DOGEE cruises I was a part of.

I would like to thank my amazing parents for all the love and encouragement they've given me throughout my life. I will always appreciate the sacrifice and investment they made in my education. And of course, thank you to my beautiful wife who has been so patient with me and supportive and just generally made my life better. Life is brilliant with you Katie.

I want to end with a somewhat relevant excerpt from Psalm 107:

Out at sea you saw God in action,
saw His breathtaking ways with the ocean:
With a word He called up the wind -
and ocean storm, towering waves!
You shot high in the sky, then the bottom dropped out;
your hearts were stuck in your throats.
You were spun like a top, you reeled like a drunk,
you didn't know which end was up.
Then you called out to God in your desperate condition;
He got you out in the nick of time.

He quieted the wind down to a whisper,
put a muzzle on all the big waves.
And you were so glad when the storm died down,
and He led you safely back to harbour.

Chapter 1

Introduction

We live on a planet with a changing climate. Since the industrial revolution some 200 years ago, the global climate system, and in particular the global carbon cycle, have been heavily impacted by large increases in atmospheric CO_2. The concentration of atmospheric CO_2 has risen at a rate at least 10 and possibly 100 times faster than any other time in history [1].

The ocean has always played a vital role in atmospheric CO_2 concentrations, acting as a reservoir absorbing and re-releasing the gas from the atmosphere [2–4]. Carbon dioxide is continuously exchanged between the atmosphere and the upper ocean by a number of biogeochemical processes. Characterising these processes, and their effect on the carbon cycle, is crucial in predicting how the Earth's climate may change in the coming century.

It is with this in mind that the Natural Environment Research Council (NERC) launched the UK SOLAS (Surface-Ocean Lower-Atmosphere Study) programme. The aim of the programme was to understand interactions between the atmosphere and the ocean, specifically those of environmental importance. It focussed on material exchanges which affect ocean productivity, atmospheric composition, and climate.

The Deep Ocean Gas Exchange Experiment (DOGEE) was started as part of the SOLAS programme. This experiment would involve two sea trials and would look at a number of ocean processes including gas, heat and

momentum flux; gas transfer through surfactants; and more importantly for this thesis, sub-surface bubble populations caused by breaking waves.

Air-sea gas flux is usually parameterised using the gas-transfer velocity and the air-sea concentration difference in what is known as a thin-film model [5]. This approach, however, does not take into account additional gas-flux through air bubbles produced by breaking waves. In a letter to Nature, Wallace and Wirick [6] presented evidence that in periods of surface wave activity, there is an increase in the amount of O_2 that is dissolved into the ocean. However, a lack of vertical resolution in the measurements they made meant that water advection and entrainment could not be ruled out as the cause of this increased flux. Farmer *et al.* [7] later presented evidence that this increased gas transfer was in fact due to air bubbles entrained by breaking waves. They suggested that existing transfer coefficients were in fact an underestimate for periods of wave activity.

Acoustics has been used to measure oceanic bubble populations for several decades [8–12]. One such technique is to measure attenuation as a function of frequency, and these measurements can then be inverted to give the number of bubbles over a range of bubble radii. If such data could be measured alongside auxiliary data (for example wave height and wind speed, but also gas-flux measured by other DOGEE participants [13]) then it could further our understanding of the impact of sub-surface bubble plumes on air-sea gas transfer. This thesis reports on experiments undertaken over two sea trials (D313 in November/December 2006 and D320 in June/July 2007) and the resulting data that can be extracted from these measurements. The bubble size distributions measured in the ocean are used as the basis for a gas-flux model and produce values for the bubble-mediated transfer velocity, K_{b}, and equilibrium supersaturation, δ, for the four major constituents of the Earth's atmosphere - nitrogen, oxygen, carbon dioxide and argon. Previously, these parameters have been estimated through modelling alone [14, 15]. The work carried out here is the first time that values for these parameters have been calculated using a strong basis of experimental work.

The following chapter reviews some of the literature relevant to this thesis and the work that has been carried out during this PhD. Chapter 3 explains the theory used throughout the thesis and lays a foundation to the experimental work, which is outlined in chapter 4. The analysis of the experimental data is detailed in chapter 5. These results then form the basis of a gas flux model, developed and presented in chapter 6. The major conclusions of this work are detailed in chapter 7.

Chapter 2

Literature Review

This chapter presents a review of some of the key papers relevant to the topics discussed in this report. The chapter begins with a discussion of bubble inversion theory and backscatter theory. A brief background of air-sea gas exchange is then presented, and the chapter finishes by discussing papers focussed on sub-surface bubble cloud modelling and air-sea gas transfer models.

2.1 Theory and computational techniques for inferring bubble size distributions from measured acoustic attenuation

This section discusses papers regarding the relationship between acoustic attenuation measurements and bubble size distributions. The relationship between the complex ratio of sound speeds and the bubble size distribution is introduced, allowing the calculation of frequency dependent attenuation from a known bubble population. The theory is then advanced to produce an inversion allowing bubble size distributions to be calculated from measured attenuation.

2.1.1 The forward model

Commander and Prosperetti [16] presented a much cited equation for the complex ratio of sound speeds, given as

$$\frac{c_{\mathrm{w}}^2}{c_{\mathrm{c}}^2} = 1 + 4\pi c_{\mathrm{w}}^2 \int_0^\infty \frac{R_0 n(R_0) \mathrm{d}R_0}{\omega_0^2 - \omega^2 + 2i\beta_{\mathrm{tot}}\omega} \tag{2.1}$$

where c_{w} is the speed of sound in water, c_{c} is the sound speed in the bubble cloud, R_0 is the equilibrium bubble radius, ω_0 is the natural frequency of a bubble, ω is angular frequency, i is the imaginary constant ($i = \sqrt{-1}$) and β_{tot} is the damping constant. Equation (2.1) was reached by linearising an equation of motion for a bubble, given by Keller [17, 18] as

$$\left(1 - \frac{\dot{R}}{c_{\mathrm{w}}}\right) R\ddot{R} + \frac{3}{2}\left(1 - \frac{\dot{R}}{3c_{\mathrm{w}}}\right)\dot{R}^2 = \frac{1}{\rho_{\mathrm{w}}}\left(1 + \frac{\dot{R}}{c_{\mathrm{w}}} + \frac{R}{c_{\mathrm{w}}}\frac{\mathrm{d}}{\mathrm{d}t}\right)(p_{\mathrm{L}} - P) \tag{2.2}$$

where R is the instantaneous radius of the bubble, ρ_{w} is the density of water, p_{L} is the liquid pressure at the bubble interface and P is the pressure at the position occupied by the bubble if the bubble were absent.

Having derived the complex ratio of sound speeds, equation (2.1), Commander and Prosperetti showed how attenuation at frequency ω can be calculated from a known bubble size distribution using the equation

$$A = 20\log_{10}(\mathrm{e})\left(\frac{\omega v}{c_{\mathrm{w}}}\right) \tag{2.3}$$

where attenuation, A, is in decibels per unit length, and v is the imaginary part of equation (2.1).

Equation (2.1) forms the basis of inversion theory used by many in the measurement of bubble size distributions [16, 19–22]. The theory, however, assumes that the bubbles undergo steady-state monochromatic linear pulsations in a free field without interacting.

In a later advance, Leighton *et al.* [8] presented a theoretical model which does not require the assumptions of monochromaticity, steady state or lin-

earity. Leighton *et al.* first derived an equation representing the speed of sound per unit volume in the bubble cloud, given as

$$\xi_{\mathrm{cl}} \approx c_{\mathrm{w}} \left(1 - \rho_{\mathrm{w}} c_{\mathrm{w}}^2 \sum_{\mathrm{j}=1}^{J} n_{\mathrm{j}}(R_{0\mathrm{j}}) \frac{\mathrm{d}V_{\mathrm{j}}(t)}{\mathrm{d}P_{\mathrm{l}}(t)} \right)^{-1/2}, \tag{2.4}$$

where V is the volume of gas and P_{l} is the driving pressure. The bubble population, given by $n_{\mathrm{j}}(R_{0\mathrm{j}})$ (where $n(R_0)\mathrm{d}R_0$ is the number of bubbles per cubic metre having radii between R_0 and $R_0 + \mathrm{d}R_0$), is split up into J discrete radius bins. Equation (2.4) is derived without making any assumptions of small amplitude, steady-state, monochromatic or linear bubble pulsations. The equation provides a framework into which different bubble dynamics models can be inserted. Leighton *et al.* found the rate at which a bubble subtracts energy from the acoustic field by considering the relationship between the gas volume in the bubble and the applied acoustic pressure. By doing so, a forward model was completed, providing a nonlinear model of acoustic propagation through a bubble cloud.

In chapter 3, it is shown how equation (2.4) reduces to equation (2.1) under assumptions of linear, steady-state and monochromatic pulsations (see equations (3.26) to (3.32)).

2.1.2 Inverting measured attenuation to give the bubble size distribution

Commander and McDonald [23] presented a method of inverting the theory given in [16] to calculate a bubble size distribution using measured attenuation. The problem takes the form of a Fredholm integral equation of the first kind, given by

$$\alpha(f) = \int_{R_{0,\min}}^{R_{0,\max}} \Omega_{\mathrm{e}}(f, R_0) \Psi(R_0) \mathrm{d}R \tag{2.5}$$

where $\alpha(f)$ is the frequency dependent attenuation, Ω_e is the extinction cross section and Ψ is the bubble size distribution. Equation (2.5) can be solved

using a series of linear B-splines (B_j), resulting in the bubble size distribution being approximated by

$$\Psi(R_0) = \sum_{\mathrm{j}=1}^{N} \Psi_\mathrm{j} B_\mathrm{j}(R_0). \tag{2.6}$$

Substituting equation (2.6) into equation (2.5) gives

$$\alpha(f_\mathrm{j}) = \sum_{\mathrm{j}=1}^{N} K_\mathrm{ij} \Psi_\mathrm{j} \tag{2.7}$$

where K_ij is a matrix given by

$$K_{ij} = \int_{R_{0,\min}}^{R_{0,\max}} \Omega_\mathrm{e}(f_\mathrm{i}, R_0) B_\mathrm{j}(R_0) \mathrm{d}R. \tag{2.8}$$

Equation (2.7) can be written in matrix form as

$$\boldsymbol{\alpha} = \mathbf{K}\boldsymbol{\Psi} \tag{2.9}$$

and this equation can be rearranged to give a solution for bubble size distribution as

$$\boldsymbol{\Psi} = \mathbf{K}^{-1}\boldsymbol{\alpha} \tag{2.10}$$

where $\mathbf{K}^{-1}$ is the inverse matrix. Equation (2.10) is ill-conditioned since the off-diagonal values in the $\mathbf{K}$ matrix are large compared to the diagonal values. Commander and McDonald proposed a method of singular value decomposition to stabilise the solution. Using SVD, the $\mathbf{K}$ matrix is decomposed to

$$\mathbf{K} = \mathbf{U}\mathbf{W}\mathbf{V}^T \tag{2.11}$$

where $\mathbf{U}$ and $\mathbf{V}$ are orthonormal matrices and $\mathbf{W}$ is a diagonal matrix consisting of the singular values of $\mathbf{K}$.

Commander and McDonald highlighted the large effect that noise has on the solution and the requirement for regularisation of the solution. The reg-

ularisation used by the Commander and McDonald was based on subjecting the solution to a minimum curvature constraint which is a form regularly used with Fredholm integral equations [24]. The regularisation uses a regularisation parameter which is chosen by increasing the parameter until it begins to effect the larger singular values. This technique, however, simply renders the system stable. A technique for determining a suitable regularisation parameter is the L-curve method, proposed by Hansen [25] and successfully used by Leighton *et al.* [8]. This involves plotting the Euclidean norm of the regularised solution against the corresponding residual norm. This often results is a well defined 'L' shaped curve, and the optimum value for the regularisation parameter is found at the corner of the 'L'.

2.2 At-sea measurements

Since acoustic measurements form a significant part of this thesis, it is important to review historic experiments. Two different types of acoustic experiments are discussed in this section. The first are experiments to measure bubble size distributions (using a variety of techniques). The second type measure the profile of subsurface bubble clouds using inverted echo sounders.

2.2.1 The acoustic measurement of bubble size distributions

This section reviews papers describing some of the available acoustic techniques for measuring bubble size distributions in the ocean. A comparison of historic measurements is shown in figure 2.1.

Measurement of bubble populations through acoustic attenuation

The use of acoustic attenuation to infer bubble populations is a popular technique [8, 19, 28, 31] because it is a robust method capable of interrogating large volumes of liquid. For this technique, the additional attenuation due

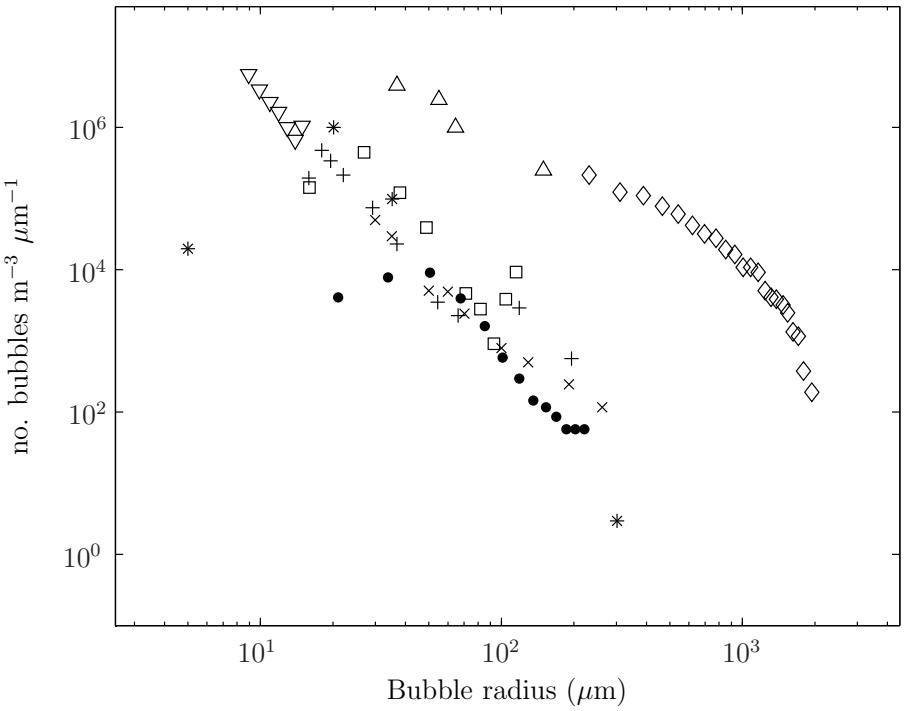

Figure 2.1: Historic bubble size distributions. These include the surf-zone measurements of Deane and Stokes [26] (diamonds), Phelps *et al.* [27] (triangles), Meers *et al.* [28] (downward pointing triangles) and Leighton *et al.* [8] (squares). Open ocean measurements were taken by Breitz and Medwin [9] (crosses), Farmer and Vagle [29] (asterisks), Johnson and Cooke [10] (dots) and Phelps and Leighton [30] (plus signs).

to bubbles is measured across a range of frequencies and this attenuation is then inverted to give bubble size distributions using the theory described in sections 2.1.1 and 2.1.2. Leighton *et al.* [8] presented an experiment undertaken at Hurst Spit, Hampshire, UK, in the surf-zone. A measurement rig measured acoustic attenuation under breaking waves with a mean height of approximately 1 metre. Measurements were made within approximately 20 metres of the water line on the beach and the mean water depth was approximately 2 metres. Bubbles with radii ranging from 16-115 μm were measured with pulses centred at single frequencies.

One of the strengths of the techniques that Leighton *et al.* [8] used in their paper was their ability to process the experimental data using both the nonlinear theory and the original theory (see section 2.1.2), thus enabling a comparison of the two techniques. Upon calculation of the bubble size distributions, it was found that there was very little difference between the two processing techniques for the 10 kPa-or-less driving pressures used in that experiment. This suggests that for low amplitude insonification, the original theoretical model can still produce accurate results.

Duraiswami *et al.* [19] successfully used acoustic attenuation measurements to calculate bubble size distributions for radii ranging from approximately 18 to 200 μm in a laboratory environment. Bubbles were generated using two techniques. Bubbles from 10 to 80 μm were generated by electrolysis at stainless steel wires. Larger bubbles (10 to 300 μm) were generated by injecting compressed air through pores in microporous tubes. A constrained minimisation procedure was used to regularise the ill-posed solutions and the results were compared and found to be in good agreement with simultaneous photographic techniques.

Measurement of bubble populations using acoustical resonators

Breitz and Medwin [9] carried out experiments in the open ocean measuring bubbles with radii from 30 to 270 μm at a depth of 25 cm using an acoustic resonator. This consisted of a flat faced transducer parallel to a plane reflec-

tor. The system worked by measuring the change in width and amplitude of several resonant modes of the resonator. These changes were predicted theoretically as well as being measured practically. In the theoretical calculations, the bubble size distribution is related to the change in width of the mode using the equation

$$n^0(R_n) = \frac{2\pi\Delta f_{\mathrm{nb}}}{c_{\mathrm{w}}\Omega_{\mathrm{e}}^{\mathrm{res}}10^6\delta_{\mathrm{R}}R_0} \tag{2.12}$$

where $n^0(R_n)$ is the zeroth-order bubble density at frequency f_{n}, Δf_{nb} is the component of resonance width due to bubbles, Ω_e^{res} is the resonance value of the extinction cross section and $10^6\delta_{\mathrm{R}}R_0$ represents the number of bubble sizes in microns whose half-power bandwidth overlaps the resonator resonance frequency.

In the experiments, the change in amplitude of the modes was measured and related to the change in width using the equation

$$(\Delta f_{\mathrm{nb}})^2 = \left(\frac{p_{\mathrm{no}}^2}{p_{\mathrm{nb}}^2}\right)(\Delta f_{\mathrm{no}})^2 \tag{2.13}$$

where p_{no}^2 is the n^{th} resonance height without bubbles, p_{nb}^2 is the height of the same resonance in the presence of bubbles and f_{no} is the width of the n^{th} resonance in bubble free water.

Experiments were carried out just outside Monterey Bay. The water depth was 120 metres with a swell of 3 metres and wind speed between 12 and 15 m s^{-1}. The acoustic resonator method was successfully used to measure bubble size distributions which strongly agreed with previous measurements [10, 32]. Breitz and Medwin [9] found a simple logarithmic fit to the average bubble densities to be

$$n(R_0) = 7.8 \times 10^8 R_0^{-2.7} \tag{2.14}$$

for bubble radii between 30 and 270 μm. Units are bubbles per m^3 per μm radius increment.

This technique was also adopted by Farmer [33–35]. In response to indication by Leighton [36] that such devices could in principle be affected by radiation loading on a bubble in a reverberant system, Farmer [35] showed that his specific design was not significantly affected by this phenomenon [37].

Measurement of bubble populations using a combination-frequency technique

The combination frequency technique uses two different frequencies to insonify bubbly water - one as a low frequency pump signal and one as a higher frequency imaging signal. One strength of the technique is that there is no ambiguity due to off-resonant scattering from large bubbles, as experienced with single frequency scattering techniques.

Newhouse and Shankar [38] first introduced the concept of using this technique to measure bubble sizes. The technique uses the principle that, as well as signals at the pump and imaging frequencies (f_p and f_i respectively), the scattered signal has sidebands at frequencies ($f_\mathrm{i} \pm f_\mathrm{p}$). For example, Chapelon *et al.* [39] gave an equation for the pressure amplitude radiated at a distance r at the sum frequency as

$$P_+ = \left[\frac{\rho_\mathrm{w} P_\mathrm{i} P_\mathrm{p}}{(\rho_\mathrm{w}\omega_0 R_0)^2}\right] X_\mathrm{p} \left(\frac{R_0}{r}\right), \tag{2.15}$$

where P_i is the pressure at the imaging frequency, P_p is the pressure at the pump frequency and

$$X_\mathrm{p} = [(1 - \omega_\mathrm{p}^2/\omega_0^2)^2 + \delta_\mathrm{D}^2(\omega_\mathrm{p}^2/\omega_0^2)]^{-1/2}, \tag{2.16}$$

where δ_D is the damping constant and ω_p is the angular frequency of the pump signal.

The aforementioned papers [38, 39], along with two subsequent papers [40, 41], presented laboratory experiments using the combination frequency technique, each showing improvements in the processing of the measured

Figure 2.2: The buoy-deployed combination frequency rig used by Phelps and Leighton [30].

data. However, although Chapelon *et al.* [39] did show very good agreement between spectra simultaneously measured acoustically and photographically, none of the papers presented absolute numbers for bubble size distributions. Oceanic bubble populations were successfully measured by Phelps and Leighton [30] who also used a sophisticated calibration method to produce absolute, not relative, numbers for the bubble size distributions. Using a rigid scaffold buoy connected to a ship through a 200 metre long umbilical, data were recorded in water depths ranging from 17-22 metres. Measurement depth was 0.5 metres and the wind speed was 10-12 m s^{-1}, gusting up to 16 m s^{-1}. The pump signal contained frequencies ranging from 17 to 200 kHz allowing the measurement of bubbles ranging in size from 16 to 192 μm. The resulting bubble size distribution followed a similar form to historic measurements (see figure 2.1) and peaked at approximately 18 μm, similar to previous findings [29].

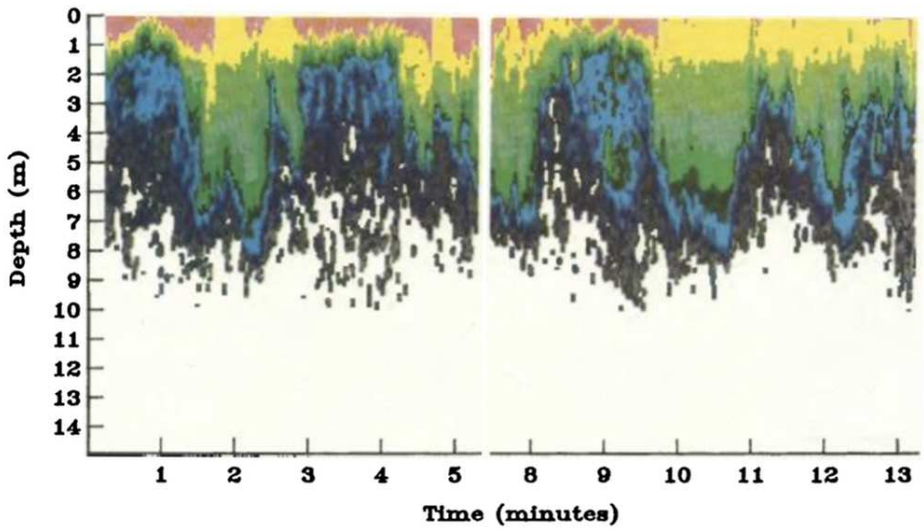

Figure 2.3: Backscatter cross section per unit volume at 200 kHz as measured by Farmer and Vagle [29] in the LA PEROUSE experiment. The data are referenced to the sea surface and corrected for vertical displacement due to wave orbital motions. The brief gap in the time series corresponds to a period when the echo sounder was switched off so as to allow uninterrupted hydrophone recordings.

2.2.2 Inverted echo sounder experiments

Inverted echo sounders (IES) send single frequency pulses upwards to the sea surface and measure the reflected pulse in order to calculate the backscatter strength of sub-surface bubble clouds.

Farmer and Vagle [29] presented experiments carried out in two locations, one 200 miles south west of Bermuda (FASINEX) and one west of Vancouver Island (LA PEROUSE), using two methods of acoustic measurement. For the FASINEX experiment, water depth was approximately 4000 metres and wind speed was 12-14 m s^{-1}. For the LA PEROUSE experiment, water depth was 140 metres and wind speed was 10 m s^{-1}.

They published results showing the backscatter cross section per unit volume at 200 kHz, for both experimental locations, giving a profile of the sub-surface bubble clouds against time. For the FASINEX (deep water)

experiment, the bubble clouds penetrated to depths of 9-13 metres with a persistent cloud depth of 2-4 metres in between the deeper portions. The LA PEROUSE (water depth = 140 metres) experiment showed more consistent bubble clouds, which on average penetrated deeper than during the FASINEX experiment, though the deepest bubble clouds were shallower than during the FASINEX experiment. The higher concentrations found in the FASINEX experiment are likely to have been caused by the higher mean wind speed increasing the whitecap coverage and number of breaking waves. The persistent band of bubbles may have been deeper in the LA PEROUSE experiment owing to the shorter wave period (3 seconds for LA PEROUSE, 5 seconds during FASINEX). This would have meant more frequent breaking waves and therefore a more persistent band of bubbles. It is also possible that in the shallower LA PEROUSE experiment, the mixed layer extended to the bottom of the water column (mixed layer depth was not stated in the original paper). This could have led to an additional source of turbulence caused by tidal currents across the sea floor, which in turn may have caused a more persistent band of bubbles.

In a detailed paper, Trevorrow [42] presented an inverted echo sounder experiment with a thorough analysis of the results and then described some of the implications of the measured bubble plumes for high-frequency sonar performance.

The IES was deployed for 81 days at Ocean Station Papa, 1400 km west of Vancouver Island in the Pacific. Water depth was 4100 metres, average wind speed was 7.5 m s^{-1} ranging up to 20 m s^{-1} and average significant wave height was 2.8 metres ranging up to 8 metres. The IES could sample at a 3 second and 30 cm resolution.

The processing of the raw waveforms was carried out using standard echo-sounder relations giving an equation for the volumetric backscatter strength per unit volume as

$$S_v(r) = 20\log_{10}[A_{\mathrm{IES}}(r)] + K_{\mathrm{cal}} + 40\log_{10}[r] + 2\cdot\alpha_{\mathrm{ab}}\cdot r - 10\log_{10}[U(r)], \quad (2.17)$$

where r is the range, A_{IES} is the raw IES amplitude, K_{cal} is a calibration factor, α_{ab} is acoustic absorption and $U(r)$ is the insonified volume.

One particular two hour period highlighted in the data showed a large number of bubble plumes reaching depths of 5 to 20 metres, much deeper than those experienced by Farmer and Vagle [29]. Trevorrow managed to extract a number of trends from the data:

- There is a relationship between the e-folding depth of the backscatter cross-section and the average bubble plume depth.
- The e-folding depth is inversely proportional to the surface bubble density.
- The plume duration generally increases with plume depth.
- There is no discernible seasonal trend.

Trevorrow then went on to study the implications of these findings to high frequency (HF) sonar performance. Historic HF reverberation models [43–45] have assumed a horizontally uniform bubble layer with an e-folding depth scale and surface bubble density dependent on wind speed alone. The IES measurements presented by Trevorrow [42] clearly showed that the e-folding depth scale and bubble concentrations are temporally and spatially variable, suggesting that previous models could be inaccurate. A model incorporating this variance was developed and compared with historic models. Trevorrow [42] found that time-averaged bubble density profiles from both models showed good agreement, suggesting that average sonar performance can be realistically predicted using horizontally uniform models. Single ping results from the new model, however, showed a variance from +8 to -30 dB when compared with the older models.

2.3 Air-sea gas flux

Gas exchange between the atmosphere and the ocean plays a major role in many biogeochemical cycles. Liss and Merlivat [5] published an excellent

paper summarising the basic principles of air-sea gas exchange. They gave a general equation for the flux, previously published by Liss [46], as

$$F = K_{\mathrm{T}}\,\Delta C, \tag{2.18}$$

where K_{T} is the total gas transfer velocity and ΔC is the concentration difference driving the gas exchange, defined as

$$\Delta C = \frac{C_{\mathrm{a}}}{H} - C_{\mathrm{w}}, \tag{2.19}$$

where C_{a} is the gas concentration in air, H is the dimensionless Henry's Law constant and C_{w} is the gas concentration in water.

The total gas transfer velocity has components for gases in the air and water phases, though Liss and Merlivat [5] show that for the majority of gases of interest, and indeed the gases examined in this thesis, the total gas transfer velocity is equal to the transfer velocity for gases in the water phase, K_{w}.

The parameterisation of this transfer velocity, K_{w}, is of the utmost importance for the understanding of air-sea gas exchange. In a series of wind/wave laboratory experiments, Jähne *et al.* [47] show that the transfer velocity is dependent on a number of factors such as Schmidt number, temperature and surface waves. However, many models define a relationship dependent simply upon wind speed [48–51]. For example, Liss and Merlivat [5] define K_{w} (for a gas with a Schmidt number of approximately 600) for a range of wind speeds, based on three water regimes, where

$$\begin{array}{lll} W_{10} < 3.6\mathrm{ms}^{-1} & K_{\mathrm{w}} = 0.17W_{10} & \text{smooth water regime} \\ 3.6\mathrm{ms}^{-1} < W_{10} < 13\mathrm{ms}^{-1} & K_{\mathrm{w}} = 2.85W_{10} - 9.65 & \text{rough water regime} \\ W_{10} > 13\mathrm{ms}^{-1} & K_{\mathrm{w}} = 5.9W_{10} - 49.3 & \text{breaking waves,} \end{array} \tag{2.20}$$

where W_{10} is the wind speed corrected to 10 metres. Figure 2.4 shows how the relationship between the transfer velocity and wind speed as found by a

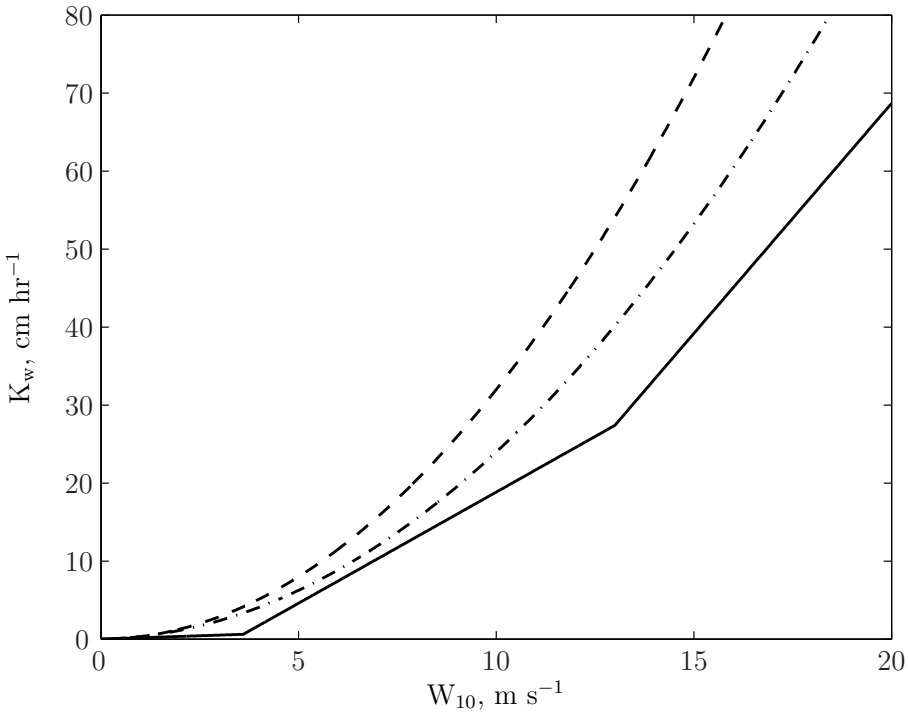

Figure 2.4: The relationship between K_w and wind speed at 10 metres elevation, W_{10}, as defined by Liss and Merlivat [5] (solid line), Wanninkhof [50] (dashed line) and Nightingale *et al.* [48] (dot-dash line).

number of experimenters. It is seen that there is some variation in the estimation of this relationship, though a quadratic proportionality is suggested by each fit. It should be noted that some experimenters have suggested a cubic fit [49].

Some experimenters have focussed on the effect of other parameters on the transfer velocity. Bock *et al.* [52] investigated the effect of the mean square slope of wind-driven waves. They found that short wind waves showed a strong, linear correlation with the transfer velocity. Asher *et al.* [53] conducted laboratory based gas exchange experiments through use of a whitecap simulation tank and found a linear relationship between the transfer velocity and whitecap coverage. Experiments were then undertaken in an outdoor surf pool to test the validity of extending this relationship to oceanic condi-

tions. The surf pool provided an order of magnitude increase in the range of available whitecap coverage compared to the whitecap simulation tank. Nevertheless, the linear relationship still held. Along with the fact that the surf pool produced waves with similar characteristics to those in the ocean, this suggests that the transfer velocity could be linearly related to whitecap coverage under oceanic conditions.

Bubbles produced by breaking waves have been highlighted as an important factor in the determination of the transfer velocity [7, 48, 53–55] and the following section reviews some of the literature relevant to this topic.

2.3.1 Bubble-mediated gas exchange

It has been shown, through both laboratory and open ocean measurements, that the onset of breaking waves significantly enhances the transfer of gas between liquid and gas phase [6, 56–58]. Through simultaneous measurement of bubble penetration, meteorological conditions and dissolved gas concentrations, Farmer *et al.* [7] confirmed the hypothesis that this increase is due to bubble-mediated gas exchange.

The transfer of gas from bubbles into the ocean is therefore an important additional means of gas flux between the atmosphere and the ocean. Woolf and Thorpe [55] showed that unlike direct transfer, bubbles can inject gas into the ocean even when the ocean is significantly supersaturated. One of the reasons bubbles can drive this supersaturation is the excess pressure within the bubbles. The pressure in a bubble is given by

$$p_{\mathrm{bub}} = p_{\mathrm{atm}} + \rho_{\mathrm{w}} g z + \frac{2\sigma}{R_0}, \tag{2.21}$$

where p_{atm} is atmospheric pressure, $2\sigma/R_0$ is the excess pressure induced by surface tension (σ), and $\rho_{\mathrm{w}} g z$ is an approximate form for the hydrostatic pressure. These give significant contributions to the pressure of the gas inside the bubble resulting in the partial pressures in the bubble exceeding the partial pressures of the same gases in air.

This significant bubble-mediated contribution to gas exchange makes parameterisation of the transfer velocity very difficult. In order to aid this characterisation, the total transfer velocity can be split into the bubble-mediated transfer velocity, K_b, and a direct transfer velocity, K_o [14, 15, 54, 59]. Using this notation, Woolf [15] defined the air-sea gas flux associated with bubbles as

$$F_\mathrm{b} = K_\mathrm{b}[C_\mathrm{w} - Sp_\mathrm{p}(1+\delta)], \tag{2.22}$$

where δ is the equilibrium supersaturation, S is the solubility and p_p is the partial pressure. This led to a newly defined total air-sea gas flux (compared to equation (2.18)) given as

$$F = (K_\mathrm{o} + K_\mathrm{b})[C_\mathrm{w} - Sp_\mathrm{p}(1+\Delta_0)], \tag{2.23}$$

where

$$\Delta_0 = \frac{\delta K_\mathrm{b}}{K_\mathrm{o} + K_\mathrm{b}}. \tag{2.24}$$

Whereas the total air-sea transfer velocity, K_T, can be readily measured [48, 60], the bubble-mediated transfer velocity, K_b, is difficult to measure directly [61]. The most common approach taken to calculate K_b is through the use of a model. The following section reviews some of these modelling techniques.

2.3.2 Bubble cloud and gas flux modelling

It has been shown that in order to produce accurate models for air-sea gas flux, it is important to know not just the bubble population, but also the life cycle history of each bubble from entrainment to dissolution [55]. In order to achieve this, modelling of the sub-surface bubble cloud evolution must be used.

Thorpe [62] detailed a model for the evolution of a sub-surface bubble cloud and showed a comparison of the model with observations of bubble clouds made by Johnson and Cooke [10]. The model took a different ap-

proach to a previously existing model [63], which was based on diffusion equations. One of the shortcomings of this previous method was the difficulty in modelling bubbles composed of more than one gas. The new model developed in Thorpe's paper took a more direct approach to the modelling of the bubbles and models each one as a particle. Modelling the bubbles in this way allows fluxes to be represented better and also allows the modelling of bubbles composed of more than one gas. Mean flows can also be incorporated though this was reported in more detail in another paper [64]. The model used by Thorpe incorporates two gases, nitrogen and oxygen.

One of the foundations of the model was the rate of change of the radius of each bubble. This is modelled using

$$\frac{\mathrm{d}R_0}{\mathrm{d}t} = \dot{R}_{0,1} + \dot{R}_{0,2}, \tag{2.25}$$

where $\dot{R}_{0,1}$ is the rate of change of radius due to gas flux, given by

$$\begin{aligned}\dot{R}_{0,1} = \frac{-3R_\mathrm{g}T}{3p_0R_0 + 4\sigma}\Bigg\{ & D_{\mathrm{mol},1}K_{\mathrm{ab},1}\mathrm{Nu}_1\left[x_\mathrm{m}\left(p_0 + \frac{2\sigma}{R_0}\right) - p_{\mathrm{p},1}\right] \\ & + D_{\mathrm{mol},2}K_{\mathrm{ab},2}\mathrm{Nu}_2\left[(1-x_\mathrm{m})\left(p_0 + \frac{2\sigma}{R_0}\right) - p_{\mathrm{p},2}\right]\Bigg\},\end{aligned} \tag{2.26}$$

where R_g is the gas constant, T is the temperature, p_0 is hydrostatic pressure, σ is surface tension, $D_{\mathrm{mol,i}}$ is molecular diffusivities, $K_{\mathrm{ab,i}}$ are absorption coefficients, $\mathrm{Nu_i}$ are Nusselt numbers (the factor by which turbulence of flow enhances the gas exchange above that expected by molecular diffusion alone [55]), x_m is mole fraction and $p_{\mathrm{p,i}}$ are partial pressures. The rate of change of radius due to pressure variation, $\dot{R}_{0,2}$, is given by

$$\dot{R}_{0,2} = \frac{-R_0^2}{3p_0R_0 + 4\sigma}\frac{\mathrm{d}p_0}{\mathrm{d}t}. \tag{2.27}$$

A number of other parameters were used in the model such as bubble rise velocity and turbulent diffusion coefficient.

With the model in place, Thorpe ran numerous tests, using both a uniform

input of bubbles and an input varying with bubble radius, and presented a comparison of the results with the observations of Johnson and Cooke. The model was run each time until steady state was reached at which point bubble size distributions, gas fluxes and acoustic scattering cross-sections were calculated. With each bubble size distribution generated, Thorpe found a bubble radius at which the distribution peaked and this peak moved to smaller bubbles with increasing depth. There was good agreement between the model results and the observations of Johnson and Cooke at different depths, though the modelled peaks tend to smaller radii as depth increases. Thorpe saw this as a discrepancy but it is interesting to note that a number of scientists have suggested that Johnson and Cooke underestimate the number of smaller bubbles in their bubble size distributions because of the limits of the photographic technique they used [7, 9, 11]. This offers a possible explanation of the discrepancies found by Thorpe.

Building on Thorpe's model, Woolf and Thorpe [55] presented an in-depth model for calculating gas flux from bubbles, focussing specifically on nitrogen, oxygen, argon and carbon dioxide (the dominant gas constituents of the Earth's atmosphere). Woolf and Thorpe showed how the composition of a bubble is a complex function of the past history of the bubble and also how the exchange of a particular gas will partly depend on the saturation level of nitrogen and oxygen in the ocean. Therefore in order to calculate gas flux correctly, it is important to take into account the change in the composition of the bubbles.

In order to calculate the amount of gas transferred by bubbles, Woolf and Thorpe developed a bubble model similar to that in Thorpe [62]. They first executed the model using an input of 1000 bubbles at a single radius, with that radius being chosen in the range of 25-800 μm. They then ran the model using an oceanic bubble size distribution (based on an R_0^{-4} relationship) as an input. For each method, they looked at the net transfer of each gas by 1000 bubbles.

The first series of tests, with single radius input, showed that small bub-

bles are important for the transfer of less soluble gases, such as nitrogen and oxygen, but not so important for more soluble gases, such as carbon dioxide, because of the gases rapid equilibration. The tests also showed that the maximum downwelling speed of the ocean water has a large effect on small bubbles but is fairly insignificant for larger bubbles.

An oceanic distribution of bubbles was produced by finding parameters for the model that produced the best fit to the bubble size distribution measured by Johnson and Cooke [10]. It was possible to match these measurements well for bubble radii ranging from 60-150 μm. The authors found a fit to the data proportional to R_0^{-4}. They then ran the model for gas flux using a number of different supersaturations for each gas, 135 permutations altogether. It was found that in many cases, the resulting gas fluxes could be described using a set of linear equations, given by

$$\begin{aligned} \mathrm{N_2\ flux\ } (\times 10^{-9}\ \mathrm{moles}),\ F_\mathrm{N} &= 16.1 - 32\delta_\mathrm{N} - 5\delta_\mathrm{O} \\ \mathrm{O_2\ flux\ } (\times 10^{-9}\ \mathrm{moles}),\ F_\mathrm{O} &= 4.5 - 10\delta_\mathrm{O} - 4\delta_\mathrm{N} \\ \mathrm{A\ flux\ } (\times 10^{-9}\ \mathrm{moles}),\ F_\mathrm{A} &= 0.199 - 0.42\delta_\mathrm{A} - 0.19\delta_\mathrm{N} - 0.08\delta_\mathrm{O} \\ \mathrm{CO_2\ flux\ } (\times 10^{-9}\ \mathrm{moles}),\ F_\mathrm{C} &= 8.0 - 50\delta_\mathrm{C} - 12\delta_\mathrm{N} - 4\delta_\mathrm{O} \end{aligned} \tag{2.28}$$

where δ_i is the fractional supersaturation of each gas. It should be noted that at low maximum downwelling speeds, the equations to describe the gas flux become more non-linear. These formulae were then combined with the equation for the bubble size distribution matching the observations of Johnson and Cooke to give the gas flux at a wind speed of approximately 12 m s^{-1}. A bubble injection rate proportional to $(W_{10})^{3.4}$ (as for whitecap coverage) was assumed which leads to an equation for the flux of each gas at any windspeed, for example

$$\text{Flux of nitrogen, } F_\mathrm{b}^\mathrm{N} = -38 \left(\frac{W_{10}}{12}\right)^{3.4} F_{1000,\mathrm{N}} \times 10^{-9}\ \mathrm{moles\ m^{-2}\ s^{-1}}. \tag{2.29}$$

In their conclusions, Woolf and Thorpe highlighted the uncertainty of the

true distribution of small bubbles and called for more accurate measurements of these bubbles since these small bubbles have a large effect on the total gas flux. The work carried out for this PhD answers this call by providing open ocean bubble size distributions over a large range of bubble radii, including radii down to less than 20 μm.

Chapter 3

Theory for Bubble Acoustics

Acoustic techniques are particularly popular in providing size distributions of gas bubbles in liquid because they operate in optically opaque conditions, can interrogate large volumes of liquid, and can detect small bubbles easily (since bubble radius varies approximately inversely with resonant frequency) [65–68]. There are many ways of using acoustics to size bubbles in liquids [9, 27, 29, 30, 38, 39, 41, 65–75]. Of the four active acoustic techniques used in the ocean [67, 68, 76], this thesis exploits the inversion of attenuation data to calculate bubble size distributions. This is a method that has been used for many years by numerous experimentalists [8, 19, 31]. The underpinning theory has remained moderately unchanged since the pioneering papers of Commander and Prosperetti [16] and Commander and McDonald [23]. Leighton *et al.* [8] highlighted some of the inherent assumptions in the theory and developed a model that does not depend upon homogeneity of the bubble cloud, nor the assumption of linear steady-state monochromatic pulsations.

The method carried out throughout this thesis uses sound pressure low enough to remain in the linear regime and therefore uses the theory described in references [16] and [23].

This chapter is split into two sections, the first describing the forward model and the inversion and the second discussing the inverted echo sounder

theory and the relationship between the volumetric backscattering strength and the bubble size distribution.

3.1 Forward model

The forward model is based upon the binomial expansion of the complex ratio of sound speeds, first presented by Commander and Prosperetti [16] as

$$\frac{c_{\mathrm{w}}^2}{c_{\mathrm{c}}^2} = 1 + 4\pi c_{\mathrm{w}}^2 \int_0^\infty \frac{R_0 n(R_0) dR_0}{\omega_0^2 - \omega^2 + 2i\beta_{\mathrm{tot}}\omega} \tag{3.1}$$

where ω_0 represents the resonant frequencies of the bubbles and is defined as [65]

$$\omega_0 = \frac{1}{R_0\sqrt{\rho_{\mathrm{w}}}}\sqrt{3\kappa(p_0 + \frac{2\sigma}{R_0} - p_{\mathrm{v}}) - \frac{2\sigma}{R_0} + p_{\mathrm{v}} - \frac{4\eta^2}{\rho_{\mathrm{w}} R_0^2}} \tag{3.2}$$

where p_{v} is the vapour pressure within the bubble, η is the shear viscosity and κ is the polytropic index which describes the nature of the reversible component of heat transfer across the bubble wall [65]. It is given by

$$\kappa = \gamma(1 + \beta_{\mathrm{th}}^2)^{-1}\left(1 + \frac{3(\gamma-1)\cdot\left[\sinh\frac{R_0}{l_{\mathrm{D}}} - \sin\frac{R_0}{l_{\mathrm{D}}}\right]}{\frac{R_0}{l_{\mathrm{D}}}\cdot\left[\cosh\frac{R_0}{l_{\mathrm{D}}} - \cos\frac{R_0}{l_{\mathrm{D}}}\right]}\right)^{-1} \tag{3.3}$$

where γ is the ratio of specific heats and l_{D} is the thickness of the thermal boundary layer which is given by

$$l_{\mathrm{D}} = \sqrt{\frac{D_{\mathrm{g}}}{2\omega}} \tag{3.4}$$

where D_{g} represents the thermal diffusivity of the gas in the bubble.

In equation (3.3), β_{th} is the thermal damping coefficient which also contributes to β_{tot} in equation (3.1) where

$$\beta_{\mathrm{tot}} = \beta_{\mathrm{vis}} + \beta_{\mathrm{th}} + \beta_{\mathrm{rad}} = \frac{2\eta}{\rho_{\mathrm{w}} R_0^2} + \frac{p_0}{2\rho_{\mathrm{w}}\omega R_0^2}\Im(\Phi) + \frac{\omega^2 R_0}{2c_{\mathrm{w}}}. \tag{3.5}$$

where β_{vis} is the viscous damping coefficient and β_{rad} is the radiation damping coefficient. $\Im(\Phi)$ represents the imaginary component of Φ, which is given by

$$\Phi = \frac{3\gamma}{1 - 3(\gamma - 1) \cdot i\chi \cdot [(i/\chi)^{1/2} \cdot \coth((i/\chi)^{1/2}) - 1]} \tag{3.6}$$

where

$$\chi = \frac{D_{\text{g}}}{\omega R_0^2}. \tag{3.7}$$

Equation (3.1) was produced using the relationship

$$c_{\text{c}} = \frac{\omega}{k_{\text{c}}} \tag{3.8}$$

and

$$k_{\text{c}}^2 = \frac{\omega^2}{c_{\text{w}}^2} + 4\pi\omega^2 \int_0^\infty \frac{R_0 n(R_0) \mathrm{d}R_0}{\omega_0^2 - \omega^2 + 2i\beta_{\text{tot}}\omega}. \tag{3.9}$$

Leighton *et al.* [8] presented an efficient method of reaching this ratio of sound speeds by considering the the volume of gas and water within a bubbly region of water, given as

$$V_{\text{c}} = V_{\text{w}} + V_{\text{g}} \tag{3.10}$$

where subscripts c, w and g represent the cloud, water and gas respectively. Differentiating equation (3.10) with respect to the incident pressure produces

$$\frac{\mathrm{d}V_{\text{c}}}{\mathrm{d}p} = \frac{\mathrm{d}V_{\text{w}}}{\mathrm{d}p} + \frac{\mathrm{d}V_{\text{g}}}{\mathrm{d}p}. \tag{3.11}$$

Multiplying through by $1/V_{\text{c}}$ gives

$$\frac{1}{V_{\text{c}}}\frac{\mathrm{d}V_{\text{c}}}{\mathrm{d}p} = \frac{1}{V_{\text{c}}}\frac{V_{\text{w}}}{V_{\text{w}}}\frac{\mathrm{d}V_{\text{w}}}{\mathrm{d}p} + \frac{1}{V_{\text{c}}}\frac{V_{\text{g}}}{V_{\text{g}}}\frac{\mathrm{d}V_{\text{g}}}{\mathrm{d}p}. \tag{3.12}$$

Using the relationship

$$B = -V\frac{\mathrm{d}p}{\mathrm{d}V}, \tag{3.13}$$

where B is the bulk modulus, equation (3.12) can be rearranged to give

$$\frac{1}{B_{\mathrm{c}}} = \frac{V_{\mathrm{w}}}{V_{\mathrm{c}}}\frac{1}{B_{\mathrm{w}}} + \frac{V_{\mathrm{g}}}{V_{\mathrm{c}}}\frac{1}{B_{\mathrm{g}}}. \tag{3.14}$$

Now using equation (3.14) and the conservation of mass, where

$$\rho_{\mathrm{c}} V_{\mathrm{c}} = \rho_{\mathrm{w}} V_{\mathrm{w}} + \rho_{\mathrm{g}} V_{\mathrm{g}}, \tag{3.15}$$

a quantity representative of the sound speed in the cloud can be defined as

$$\xi_{\mathrm{c}} = \sqrt{\frac{B_{\mathrm{c}}}{\rho_{\mathrm{c}}}} = \sqrt{\left(\frac{V_{\mathrm{c}}}{\rho_{\mathrm{w}} V_{\mathrm{w}} + \rho_{\mathrm{g}} V_{\mathrm{g}}}\right)\left(\frac{V_{\mathrm{w}}}{V_{\mathrm{c}} B_{\mathrm{w}}} + \frac{V_{\mathrm{g}}}{V_{\mathrm{c}} B_{\mathrm{g}}}\right)^{-1}}. \tag{3.16}$$

Assuming a low void fraction so that

$$\rho_{\mathrm{g}} V_{\mathrm{g}} \ll 1 \tag{3.17}$$

and

$$\frac{V_{\mathrm{c}}}{V_{\mathrm{w}}} \approx \frac{V_{\mathrm{w}}}{V_{\mathrm{c}}} \approx 1, \tag{3.18}$$

and using the relationship between sound speed, density and the bulk modulus given as

$$c_{\mathrm{w}} = \sqrt{\frac{B_{\mathrm{w}}}{\rho_{\mathrm{w}}}}, \tag{3.19}$$

equation (3.16) can be approximated as

$$\xi_{\mathrm{c}} \approx c_{\mathrm{w}}\left(1 + \frac{B_{\mathrm{w}} V_{\mathrm{g}}}{V_{\mathrm{c}} B_{\mathrm{g}}}\right)^{-1/2}. \tag{3.20}$$

The bubbly water is assumed to be inhomogeneous and therefore must be broken down into L volume elements, each one being sufficiently small so that each bubble is subjected to the same pressure change simultaneously. The bulk modulus, B_{gl}, for each element, related to the volume changes of

the I bubbles in the element can be defined as

$$\frac{1}{B_{\mathrm{gl}}} = -\frac{1}{V_{\mathrm{gl}}} \sum_{\mathrm{i}=1}^{I} \frac{\mathrm{d}V_{\mathrm{i}}}{\mathrm{d}P_{\mathrm{l}}}. \tag{3.21}$$

Substituting equation (3.21) into equation (3.20) gives

$$\xi_{\mathrm{cl}} \approx c_{\mathrm{w}} \left(1 - \frac{\rho_{\mathrm{w}} c_{\mathrm{w}}^2}{V_{\mathrm{cl}}} \sum_{\mathrm{i}=1}^{I} \frac{\mathrm{d}V_{\mathrm{i}}}{\mathrm{d}P_{\mathrm{l}}} \right)^{-1/2}, \tag{3.22}$$

which represents the sound speed in a single volume element. The continuum of bubble radii can be discretised by creating J radius bins with the width of each bin, j, usually being 1 μm. The volume of gas in each volume element can then be expressed as

$$V_{\mathrm{gl}}(t) = \sum_{\mathrm{j}=1}^{J} N_{\mathrm{j}}(R_{0\mathrm{j}}, t) V_{\mathrm{j}}(t) = V_{\mathrm{cl}} \sum_{\mathrm{j}=1}^{J} n_{\mathrm{j}}(R_{0\mathrm{j}}, t) V_{\mathrm{j}}(t), \tag{3.23}$$

where N_{j} is the total number of bubbles in each bin and

$$n_{\mathrm{j}}(R_{0\mathrm{j}}, t) = N_{\mathrm{j}}(R_{0\mathrm{j}}, t)/V_{\mathrm{cl}}, \tag{3.24}$$

which is the total number of bubbles per unit volume in the j^{th} bin. Expressing equation (3.22) using this bin scheme gives

$$\xi_{\mathrm{cl}} \approx c_{\mathrm{w}} \left(1 - \rho_{\mathrm{w}} c_{\mathrm{w}}^2 \sum_{j=1}^{J} n_{\mathrm{j}}(R_{0\mathrm{j}}) \frac{\mathrm{d}V_{\mathrm{j}}(t)}{\mathrm{d}P_{\mathrm{l}}(t)} \right)^{-1/2}. \tag{3.25}$$

The volume of each bubble is given by

$$V = \frac{4}{3} \pi R^3. \tag{3.26}$$

Differentiating equation (3.26) with respect to R gives

$$\frac{\mathrm{d}V}{\mathrm{d}R} = 4\pi R^2, \tag{3.27}$$

which, as Leighton *et al.* [8] point out, in the linear limit only reduces to

$$\frac{\mathrm{d}V}{\mathrm{d}P} = 4\pi R_0^2 \frac{\mathrm{d}R}{\mathrm{d}P}. \tag{3.28}$$

Rearranging equation (3.25), substituting in equation (3.28) and replacing the summation with an integration gives

$$\begin{aligned} \frac{c_\mathrm{w}^2}{\xi_\mathrm{c}^2} &\approx 1 - \rho_\mathrm{w} c_\mathrm{w}^2 \int_0^\infty n(R_0) \frac{\mathrm{d}V}{\mathrm{d}P} \mathrm{d}R_0 \\ &\approx 1 - 4\pi\rho_\mathrm{w} c_\mathrm{w}^2 \int_0^\infty n(R_0) R_0^2 \frac{\mathrm{d}R}{\mathrm{d}P} \mathrm{d}R_0. \end{aligned} \tag{3.29}$$

For steady state, monochromatic bubble oscillations that are driven by a constant amplitude field of the form

$$p(t) = P_A e^{i\omega t}, \tag{3.30}$$

Leighton [65] gives

$$\frac{\mathrm{d}R}{\mathrm{d}p} = \frac{-1}{R_0\rho_\mathrm{w}((\omega_0^2 - \omega^2) + 2i\beta_\mathrm{tot}\omega)}. \tag{3.31}$$

Substitution of equation (3.31) into equation (3.29) gives

$$\frac{c_\mathrm{w}^2}{\xi_\mathrm{c}^2} \approx 1 + 4\pi c_\mathrm{w}^2 \int_0^\infty \frac{n(R_0)R_0}{(\omega_0^2 - \omega^2) + 2i\beta_\mathrm{tot}\omega} \mathrm{d}R_0. \tag{3.32}$$

This is equal to the complex ratio of sound speeds given in equation (3.1).

It is assumed that the void fractions experienced would be low (typical oceanic void fractions range from approximately 10^{-4} to 10^{-6} [8, 30, 34, 42]), and therefore any $n(R_0)$ terms would be sufficiently low that the fractional term in equation (3.1) is much less than one. This permits the use of a

standard binomial expansion of the form

$$(1+x)^a = 1 + ax + \frac{a(a-1)}{2!}x^2 + \frac{a(a-1)(a-2)}{3!}x^3 + \ldots \text{for } \mid x \mid < 1. \quad (3.33)$$

Removing non-linear terms and using a binomial expansion, equation (3.1) becomes

$$\frac{c_\mathrm{w}}{c_\mathrm{c}} = 1 + 2\pi c_\mathrm{w}^2 \int_0^\infty \frac{R_0 n(R_0)}{\omega_0^2 - \omega^2 + i2\beta_\mathrm{tot}\omega} \mathrm{d}R_0. \quad (3.34)$$

If equation (3.34) is rearranged to give

$$\frac{c_\mathrm{w}}{c_\mathrm{c}} - 1 = 2\pi c_\mathrm{w}^2 \int_0^\infty \frac{R_0 n(R_0)}{\omega_0^2 - \omega^2 + i2\beta_\mathrm{tot}\omega} \mathrm{d}R_0, \quad (3.35)$$

it shows how the complex sound speed can be related linearly to the number of bubbles in the medium. This relationship can then be split into real and imaginary parts, given by

$$\frac{c_\mathrm{w}}{c_\mathrm{c}} - 1 = u - iv, \quad (3.36)$$

where u represents the phase speed in the medium and v the attenuation. Attenuation can then be calculated, as stated in equation (2.3), using

$$A = 20 \left(\frac{\omega v}{c_\mathrm{w}} \right) \log_{10}(e), \quad (3.37)$$

with attenuation being expressed in dB/m.

In the experiments reported in this thesis, only attenuation measurements are made, since measurements of phase speed were found to be very unreliable because of the sensitivity of the measurements. The following section describes the theory used to invert measured sets of attenuation in order to calculate bubble size distributions.

3.2 Inversion of the forward model

The problem of the inversion takes the form of a Fredholm integral equation, given by [23]

$$\alpha(\omega) = \int_{R_{0,\min}}^{R_{0,\max}} \Omega_{\mathrm{e}}(\omega, R_0)\Psi(R_0)\mathrm{d}R_0, \tag{3.38}$$

where the known quantities are α, which is the measured attenuation as a function of frequency, and Ω_{e}, which is the extinction cross section of a bubble of radius R_0 being insonified at frequency ω. The unknown quantity is Ψ, which represents the bubble size distribution.

The extinction cross section arises from the fact that a bubble causes energy to be lost from an acoustic wave. As the wave hits the bubble in the long-wavelength limit, it causes the bubble to pulsate and these pulsations are damped by viscous and thermal mechanisms. The pulsations also reradiate sound, scattering the acoustic energy. This loss of energy from the acoustic wave caused by the presence of a bubble is the extinction cross section and is defined as the ratio of time averaged power loss per bubble, $\langle \dot{W} \rangle$, to the intensity of the incident acoustic beam, I_{b}.

$$\Omega_{\mathrm{e}} = \frac{\langle \dot{W} \rangle}{I_{\mathrm{b}}}. \tag{3.39}$$

For the inversion, the extinction cross section can be computed using an equation given by Leighton [65] as

$$\Omega_{\mathrm{e}} = \frac{\beta_{\mathrm{tot}}}{\beta_{\mathrm{rad}}} \frac{4\pi R_0^2}{((\omega_0/\omega)^2 - 1)^2 + \beta_{\mathrm{tot}}}, \tag{3.40}$$

where β_{tot} is the total damping constant consisting of the thermal, viscous and radiation damping constants. The radiation damping constant, β_{rad}, is corrected following the method of Ainslie and Leighton [77] to use the radiation damping constant of Andreeva and Weston [78, 79], where

$$\beta_{\mathrm{rad}} = \frac{\omega_0^2 R_0}{c_{\mathrm{w}}\, \omega}. \tag{3.41}$$

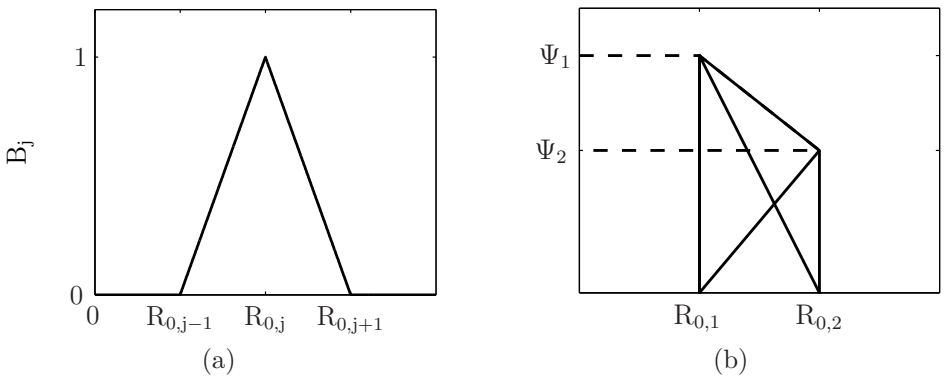

Figure 3.1: Examples of (a) a linear B-spline, and (b) B-spline integration.

With the attenuation and extinction cross sections known, the bubble size distribution can now be calculated. The range of radii (between $R_{0,\min}$ and $R_{0,\max}$) is divided into N+1 intervals. A set of N linear B-spline functions are then defined by

$$B_j(R_0) = \begin{cases} \frac{R_0 - R_{0,j-1}}{R_{0,j} - R_{0,j-1}} & \text{if } R_{0,j-1} < R_0 < R_{0,j} \\ \frac{R_{0,j+1} - R_0}{R_{0,j+1} - R_{0,j}} & \text{if } R_{0,j} < R_0 < R_{0,j+1} \\ 0 & \text{otherwise} \end{cases} . \tag{3.42}$$

These B-splines take the form shown in figure 3.1(a).

These B-splines are used because they essentially give a linear interpolation when integrated, as shown in figure 3.1(b). The area between points $R_{0,1}$ and $R_{0,2}$ is given by

$$\begin{aligned} R_{0,\text{area}} &= \Psi_2 \Delta x + \frac{1}{2}(\Psi_1 - \Psi_2)\Delta x \\ &= \frac{1}{2}(\Psi_1 + \Psi_2)\Delta x. \end{aligned} \tag{3.43}$$

The bubble size distribution can then be approximated by

$$\Psi(R_0) = \sum_{j=1}^{N} \Psi_j B_j(R_0), \tag{3.44}$$

where

$$\Psi_{\mathrm{j}} = \Psi(R_{0,\mathrm{j}}). \tag{3.45}$$

Substitution of equation (3.44) into equation (3.38) gives

$$\begin{aligned} \alpha(\omega) &= \int_{R_{0,\min}}^{R_{0,\max}} \Omega_{\mathrm{e}}(\omega, R_0) \sum_{\mathrm{j}=1}^{N} \Psi_{\mathrm{j}} B_{\mathrm{j}}(R_0) \mathrm{d}R_0 \\ &= \sum_{\mathrm{j}=1}^{N} \Psi_{\mathrm{j}} \int_{R_{0,\min}}^{R_{0,\max}} \Omega_{\mathrm{e}}(\omega, R_0) B_{\mathrm{j}}(R_0) \mathrm{d}R_0. \end{aligned} \tag{3.46}$$

The attenuation, $\alpha(\omega)$, has been measured at N frequencies corresponding to the resonances of bubbles at radii $R_1, R_2, R_3, \ldots, R_N$. For $\mathrm{i} = 1 : N$,

$$\alpha(\omega_{\mathrm{i}}) = \sum_{\mathrm{j}=1}^{N} \Psi_{\mathrm{j}} \int_{R_{0,\min}}^{R_{0,\max}} \Omega_{\mathrm{e}}(\omega_{\mathrm{i}}, R_0) B_{\mathrm{j}}(R_0) \mathrm{d}R_0. \tag{3.47}$$

Equation (3.47) can be simplified by using

$$K_{\mathrm{ij}} = \int_{R_{0,\min}}^{R_{0,\max}} \Omega_{\mathrm{e}}(\omega_{\mathrm{i}}, R_0) B_{\mathrm{j}}(R_0) \mathrm{d}R_0 \tag{3.48}$$

which gives an expression for $\alpha(\omega_{\mathrm{i}})$ as

$$\alpha(\omega_{\mathrm{i}}) = \sum_{\mathrm{j}=1}^{N} \Psi_{\mathrm{j}} K_{\mathrm{ij}}. \tag{3.49}$$

This can be expressed in matrix form as

$$\begin{pmatrix} \alpha_1 \\ \alpha_2 \\ \alpha_3 \\ \vdots \\ \alpha_N \end{pmatrix} = \begin{pmatrix} K_{11} & K_{12} & K_{13} & \ldots & K_{1N} \\ K_{21} & K_{22} & K_{23} & \ldots & K_{2N} \\ K_{31} & K_{32} & K_{33} & \ldots & K_{3N} \\ \vdots & \vdots & \vdots & & \vdots \\ K_{N1} & K_{N2} & K_{N3} & \ldots & K_{NN} \end{pmatrix} \begin{pmatrix} \Psi_1 \\ \Psi_2 \\ \Psi_3 \\ \vdots \\ \Psi_N \end{pmatrix}. \tag{3.50}$$

which can be written in vector matrix form as

$$\boldsymbol{\alpha} = \mathbf{K}\boldsymbol{\Psi}. \tag{3.51}$$

A solution for the bubble size distribution is given by

$$\boldsymbol{\Psi} = \mathbf{K}^{-1}\boldsymbol{\alpha}, \tag{3.52}$$

where $\mathbf{K}^{-1}$ is the inverse matrix. The $\mathbf{K}$ matrix is ill-conditioned owing to the highly peaked nature of the kernel, $\Omega_{\mathrm{e}}(\omega, R_0)$. Figure 3.2 shows the extinction cross section over a range of frequencies for a number of insonifying frequencies. It shows that although resonant bubbles contribute most significantly to the loss of energy from the acoustic wave, large bubbles also have a significant contribution due to geometrical scattering caused by their sheer physical size.

This ill-conditioning results in small changes in the attenuation vector produce large changes in the B-spline coefficient vector and therefore the bubble size distribution, $\boldsymbol{\Psi}$. This can be improved by centering the B-splines on the resonant radii corresponding to the frequencies at which the attenuation was measured. The matrix, however, is still ill-conditioned because off-diagonal values are often large compared to diagonal values due to the tails on the extinction cross sections shown in figure 3.2. This is especially the case when the frequency range is broad and there are bubbles with large radii present when the cloud is being insonified with a high frequency.

One method of solving this ill-conditioned matrix is to use singular value decomposition where the $\mathbf{K}$ matrix becomes

$$\mathbf{K} = \mathbf{U}\mathbf{W}\mathbf{V}^T, \tag{3.53}$$

where $\mathbf{U}$ and $\mathbf{V}^T$ are orthonormal matrices and $\mathbf{W}$ is a diagonal matrix consisting of the singular values w_{j} of $\mathbf{K}$.

The problem is worsened when noise is present in the signal. This can be

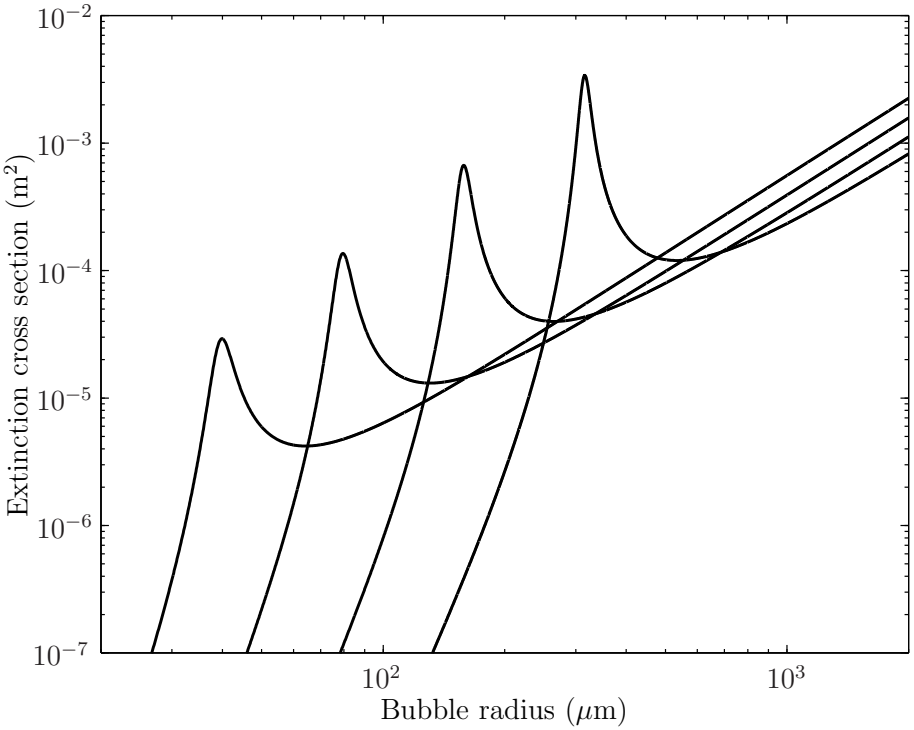

Figure 3.2: The extinction cross sections for a range of bubble radii calculated using equation (3.40) with insonification frequencies of 25, 50, 100 and 200 kHz (from left to right).

represented in the equation

$$\alpha = \alpha_{\mathrm{E}} + \delta_{\mathrm{n}}, \tag{3.54}$$

where α is the measured attenuation, α_{E} is the exact attenuation and δ_{n} is the noise. A solution to equation (3.38) can now be written as

$$\Psi = \sum_{\mathrm{j}=1}^{N} v_{\mathrm{j}} \left(\frac{u_{\mathrm{j}} \cdot \alpha_{\mathrm{E}}}{w_{\mathrm{j}}} + \frac{u_{\mathrm{j}} \cdot \delta_{\mathrm{n}}}{w_{\mathrm{j}}} \right), \tag{3.55}$$

where u_{j} are the column vectors of the matrix $\mathbf{U}$ and v_{j} are the column vectors of the matrix $\mathbf{V}$. Errors can arise here when the second fractional term is large compared to the first fractional term. When w_{j} is small, the problem becomes worse.

So to find a stable and accurate solution, Tikhonov regularisation [80] is one option that can be used. The error associated with the solution is given by

$$\mathbf{e}_{\mathrm{I}} = \boldsymbol{\alpha} - \mathbf{K}\boldsymbol{\Psi}. \tag{3.56}$$

Since measurements of attenuation alone and not phase speed as well have been made, only real numbers are used and therefore the regularised solution can be obtained by minimisation of the composite cost function ζ_{ccf}, given by

$$\zeta_{\mathrm{ccf}} = \mathbf{e}_{\mathrm{I}}^{T}\mathbf{e}_{\mathrm{I}} + \beta\boldsymbol{\Psi}^{T}\boldsymbol{\Psi}, \tag{3.57}$$

where β is a scalar value and determines the amount of regularisation. Substitution of equation (3.56) into (3.57) gives

$$\begin{aligned}
\zeta_{\mathrm{ccf}} &= (\boldsymbol{\alpha}^{T} - \boldsymbol{\Psi}^{T}\mathbf{K}^{T})(\boldsymbol{\alpha} - \mathbf{K}\boldsymbol{\Psi}) + \beta\boldsymbol{\Psi}^{T}\boldsymbol{\Psi} \\
&= \boldsymbol{\alpha}^{T}\boldsymbol{\alpha} - \boldsymbol{\Psi}^{T}\mathbf{K}^{T}\boldsymbol{\alpha} - \boldsymbol{\alpha}^{T}\mathbf{K}\boldsymbol{\Psi} + \boldsymbol{\Psi}^{T}\mathbf{K}^{T}\mathbf{K}\boldsymbol{\Psi} + \beta\boldsymbol{\Psi}^{T}\boldsymbol{\Psi} \\
&= \boldsymbol{\Psi}^{T}(\mathbf{K}^{T}\mathbf{K})\boldsymbol{\Psi} + \boldsymbol{\alpha}^{T}\boldsymbol{\alpha} - \boldsymbol{\alpha}^{T}\mathbf{K}\boldsymbol{\Psi} - \boldsymbol{\Psi}^{T}\mathbf{K}^{T}\boldsymbol{\alpha} + \beta\boldsymbol{\Psi}^{T}\boldsymbol{\Psi} \\
&= \boldsymbol{\Psi}^{T}(\mathbf{K}^{T}\mathbf{K} + \beta\mathrm{I}_0)\boldsymbol{\Psi} - 2\boldsymbol{\alpha}^{T}\mathbf{K}\boldsymbol{\Psi} + \boldsymbol{\alpha}^{T}\boldsymbol{\alpha},
\end{aligned} \tag{3.58}$$

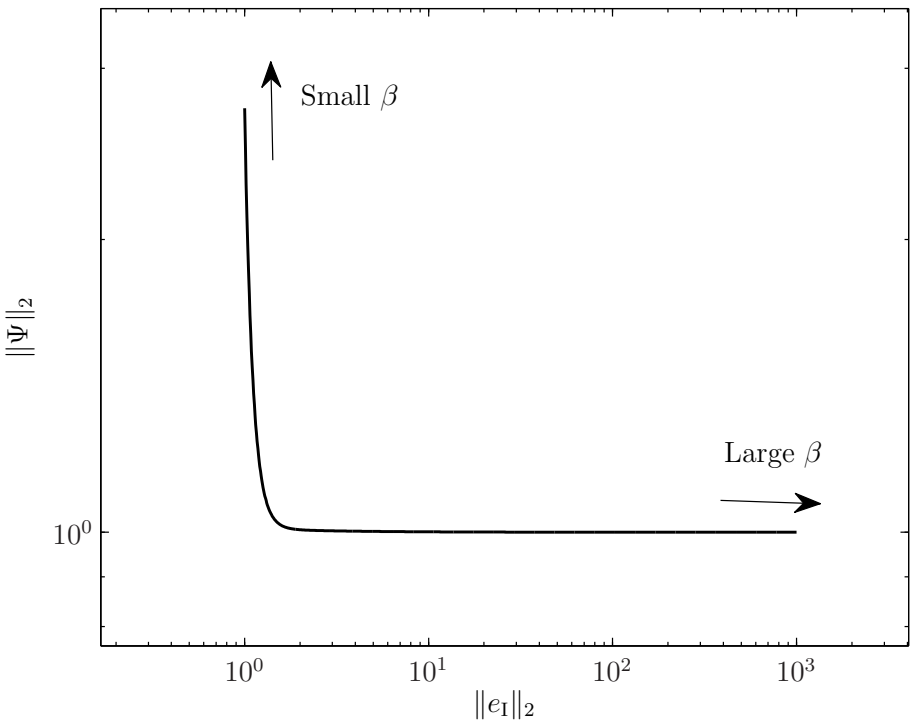

Figure 3.3: The 'L' curve produced by plotting the euclidean norm of the regularised solution, $\|\mathbf{\Psi}\|_2$ against the corresponding residual norm, $\|e_I\|_2$. This technique was not actually used to process the data from this PhD. See chapter 5 for more details on the inversion technique.

where $\mathbf{I}_0$ is the identity matrix. An optimum solution for the bubble size distribution can now be found by minimising equation (3.58) with respect to $\mathbf{\Psi}$, giving

$$\mathbf{\Psi}_{\text{opt}} = (\mathbf{K}^T\mathbf{K} + \beta\mathbf{I}_0)^{-1}(\mathbf{K}^T\boldsymbol{\alpha}). \tag{3.59}$$

One method of finding the optimum beta value is to use an 'L-curve' [25]. This method was successfully used by Leighton *et al.* [8] and involves plotting the euclidean norm of the regularised solution, $\|\mathbf{\Psi}\|_2$, against the corresponding residual norm, $\|\mathbf{e}_I\|_2$. This graph often produces a well-formed 'L-curve', shown in figure 3.3, with the optimum value for beta being the value at the corner of the 'L'. As is described in more detail in section 5.1.4,

the 'L-curve' technique has some disadvantages and, in this thesis, a different approach is taken.

3.3 Inverted echo sounder theory

An equation for volumetric backscatter strength, S_v, is presented by Trevorrow [42] as

$$S_v(r) = 20\log_{10}[A_{\mathrm{IES}}(r)] + K_{\mathrm{cal}} + 40\log_{10}[r] + 2\cdot\alpha_{\mathrm{ab}}\cdot r - 10\log_{10}[U(r)], \quad (3.60)$$

where $A_{\mathrm{IES}}(r)$ is the raw IES amplitude, K_{cal} is a calibration factor, r is the range from the source (given by $r = \frac{1}{2}\cdot c_{\mathrm{w}}\cdot t$, where c_{w} is the local sound speed and t is the time after transmission), α_{ab} is acoustic absorption and $U(r)$ is the insonified volume, given by

$$U(r) = \frac{1}{3}\varphi\left[\left(r + \frac{1}{4}c_{\mathrm{w}}\tau\right)^3 - \left(r - \frac{1}{4}c_{\mathrm{w}}\tau\right)^3\right], \quad (3.61)$$

where φ is the equivalent solid angle of the transmit transducer and τ is the pulse duration.

Equation (3.60) is derived from standard echo sounder relations [81]. The transmission loss term, $40\log_{10}[r]$, provides a time and range varying gain.

It should be noted that S_{v} is the decibel equivalent of the volumetric backscatter strength s_{v} and they are related by the equation

$$S_{\mathrm{v}} = 10\log_{10}\left(\frac{s_{\mathrm{v}}}{s_{\mathrm{v,ref}}}\right)\mathrm{dB}, \quad (3.62)$$

where $s_{\mathrm{v,ref}} = 1\,\mathrm{m}^2/\mathrm{m}^3$ is the reference value.

3.4 Relating the volumetric backscatter strength to the bubble size distribution

In order to relate the two datasets that are presented in this report, it is necessary to create a relationship between the volumetric backscatter strength and the bubble size distribution. This will enable bubble size distribution measurements to be used as a reference to calibrate volumetric backscatter strength measurements.

Leighton [65] has described a method to relate these variables by considering the extinction cross section introduced in section 3.2. Equation (3.40) stated that the extinction cross section is given by the ratio of the time averaged power loss to the intensity of the incident acoustic beam, $\Omega_\mathrm{e} = \langle \dot{W} \rangle / I_\mathrm{b}$, which is found as follows. If a plane wave travels a distance Δr through a bubble population of n_b bubbles per unit volume, the intensity is reduced by

$$\Delta I_\mathrm{b} = -n_\mathrm{b} \Omega_\mathrm{e} \Delta r. \tag{3.63}$$

Integration of equation (3.63) gives

$$I_\mathrm{b} = I_{\mathrm{b},0} e^{-n_\mathrm{b} \Omega_\mathrm{e} r}, \tag{3.64}$$

where $I_{\mathrm{b},0}$ is the intensity at $r = 0$. Now consider a cloud of bubbles, with a density described by $n(R_0)$ for increment $\mathrm{d}R_0$ so that $n(R_0)\mathrm{d}R_0$ is the number of bubbles per unit volume with radius between R_0 and $R_0 + \mathrm{d}R_0$. The extinction cross section for the cloud is given by

$$\Omega_\mathrm{e}^\mathrm{c} = \int_{R_0=0}^{\infty} \Omega_\mathrm{e} n(R_0) \mathrm{d}R_0. \tag{3.65}$$

The scattering cross section is the proportion of this power loss through scattering alone and is derived by Foldy [82] (see appendix A). By taking the definition of backscattering cross section from Clay and Medwin [83] and assuming the backscatter is omnidirectional, it is shown that these two

quantities are related by

$$\Omega_{\mathrm{b-s}} = \frac{\Omega_{\mathrm{scat}}}{4\pi}, \tag{3.66}$$

where $\Omega_{\mathrm{b-s}}$ is the backscattering cross section for an individual bubble and Ω_{scat} is the scattering cross section. Therefore, the backscattering cross section per unit volume becomes

$$s_{\mathrm{v}} = \frac{1}{4\pi} \int_{R_0=0}^{\infty} \Omega_{\mathrm{scat}} n(R_0) \mathrm{d}R_0. \tag{3.67}$$

Equation (3.67) relates the volumetric backscatter strength, s_{v}, discussed in section 3.3 to the bubble size distribution, $n(R_0)\mathrm{d}R_0$, discussed in sections 3.1 and 3.2.

3.5 Summary

This chapter has detailed the theory behind the acoustic methods used throughout this thesis. A forward model has been presented predicting frequency dependent attenuation using a bubble size distribution as an input. This was carried out using a binomial expansion of the complex ratio of sound speeds in a bubbly medium.

An inversion of this theory was then discussed along with the problems of an ill-conditioned $\mathbf{K}$ matrix and the need for regularisation in the presence of noise. A method of Tikhonov regularisation was used to find the optimum bubble size distribution.

The theory involved in the inverted echo sounder experiment is then presented with the key equations required to convert raw waveforms to volumetric backscatter strength, S_{v}.

A method of relating the volumetric backscatter strength, S_{v}, and the bubble size distribution, $n(R_0)\mathrm{d}R_0$, was then described. This allows data taken with the IES system to be calibrated by the data from the acoustic attenuation system.

The following chapter details the design and construction of a spar buoy

built to measure bubble populations using the theory described in this chapter. The experiments carried out with the spar buoy are also detailed.

Chapter 4

Sea Trials

This chapter details the method and experiments undertaken as part of this study, and the equipment used to do this. Difficulties encountered in the design of the experimental system are also discussed, as well as the changes made to equipment between the two sea trials.

4.1 Method

This section discusses the application of the theory in chapter 3 and relevant literature to the design of the acoustic experiments.

In order to measure the attenuation over a range of frequencies, a train of pulses is used, where each consecutive pulse is of a higher frequency than the previous. The construction of this train of pulses is discussed in the next section.

4.1.1 Pulse construction

The duration, shape and duty-cycle of the acoustic pulses were important factors to consider in the design of the experiment. One of the assumptions made in the formulation of the complex wavenumber is that the bubbles move with monochromatic oscillations. For this to be the case, they must have reached steady-state oscillation, a period after the initial transient response.

Ideally, pulses should be at least 20 cycles in length [28, 84]. This is because the use of pulse lengths not long enough to bring bubbles to steady-state oscillations has been known to result in a reduction in scattering [28, 85, 86] though this is not always experienced [87, 88]. The hydrophones in the experiment reported here would be mounted within a metre of the surface and therefore surface reflections begin to interfere with the direct acoustic signal. Therefore a compromise must be made as to the pulse duration, and this was decided to be 1 ms. This means that bubbles with a resonant frequency below 20 kHz would be excited for less than 20 cycles, though this was unavoidable.

It is also necessary to allow the bubbles to ring-down after excitation [8]. This allows the experimental conditions to match the starting conditions of the theory in chapter 3 (i.e., $R = R_0$ and $\mathrm{d}R/\mathrm{d}t = 0$). Therefore a pause of 20 ms was left between each pulse in the pulse train.

The recorded waveform was likely to have noise contaminating the signal and therefore hinder the identification and analysis of each pulse. In order to help identification, a Gaussian window was applied to each pulse. The resulting pulse took the form shown in figure 4.1.

4.1.2 Frequencies for attenuation measurements

One of the goals of this experiment was to have bubble size distribution measurements over a large range of bubble radii. In order to achieve this, a broad range of frequencies needed to be used in the attenuation experiment. A target range of 2-200 kHz was set as this covers the majority of the range measured by previous experimentalists, yet is broader than the measurements taken in any other single experiment. Also, in order to obtain the best possible input to gas flux models, as much detail as possible was needed about the sub-surface bubble populations.

Ideally, there should be stationarity within the bubble cloud, i.e., the population within the cloud should not change during the measurements. In reality, this is not possible with multiple pulse measurements, though it

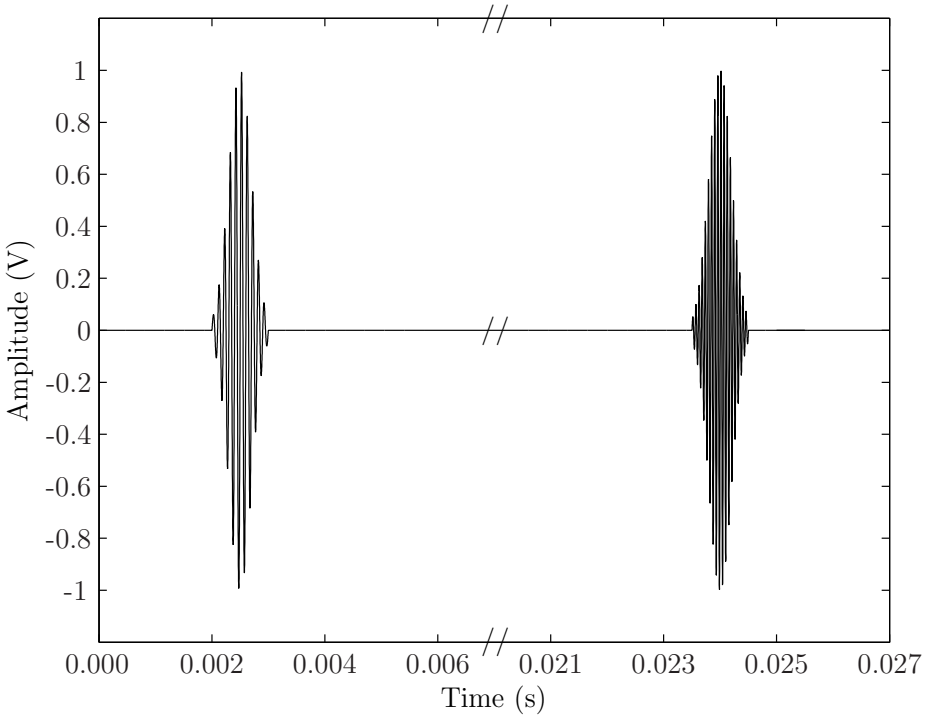

Figure 4.1: Two of the concatenated pulses in the pulse train (as generated on the computer) with frequencies 10 kHz and 18 kHz. The pulse length and off-time are 1 ms and 20 ms respectively. The x-axis is broken to remove the space between the pulses.

is possible to take measurements over a short enough time period that it is plausible to assume the bubble cloud does not change significantly over the measurement. Therefore, to keep the total measurement duration short, it is preferable to use few pulses. However, fewer pulses results in a loss of resolution in the bubble size distribution and so a compromise must be made.

A total of fourteen frequencies were used, with a single pulse at each frequency. This number of frequencies was chosen as it allowed a good resolution within the range whilst not being so many that the pulse train duration was too long to assume that the bubble cloud is stationary. With a pulse length of 1 ms, and an off-time of 20 ms, the total measurement takes 274 ms. Therefore, for a hydrophone separation of 0.2 m, the average velocity

Frequency, kHz	Bubble Radius, μm
3	1141
7	486
10	339
18	187
25	134
29	115
38	88
46	72
66	50
85	39
118	27
135	24
160	20
197	16

Table 4.1: The frequencies used in the experiments, and the corresponding resonant radii calculated using equation (4.1) at a depth of 1.2 metres, assuming air bubbles in water and κ varying between $\kappa = 1.15$ for a radius of 16 μm and $\kappa = 1.37$ for a radius of 1141 μm as described in [65].

of the bubble cloud should not exceed 0.73 m s^{-1} for stationarity to hold. Whilst this may be exceeded directly beneath a breaking wave, it is valid to assume this velocity will not be reached at the measurement depths. Table 4.1.2 shows the frequencies used along with the corresponding resonant radii, calculated using an equation [65] modified from the form given by Minnaert [89] to include surface tension forces, given as

$$\omega_0 = \frac{1}{R_0}\sqrt{\frac{3\kappa p_{\mathrm{bub}}}{\rho_w} - \frac{2\sigma}{\rho_{\mathrm{w}} R_0}}, \tag{4.1}$$

where κ is the polytropic index, p_{bub} is the pressure inside the bubble, ρ_w is the density of the liquid and σ is the surface tension. The frequencies were chosen to give as even a spacing as possible whilst operating within the most sensitive ranges of each of the transmit transducers.

4.2 Experiment

The acoustic experiments were undertaken as part of a collaborative project with scientists and technicians at the National Oceanography Centre (NOC), Southampton, who designed and built a spar buoy capable of having all necessary equipment mounted on it. The spar buoy is 11 metres long with approximately 2.5 metres protruding above the sea surface (see figure 4.2(b)). The spar buoy had a damping plate on the bottom of it which, as well as holding the batteries, allowed the buoy to ride up and down with the long period waves (i.e., swell) and yet not with the shorter period waves (i.e., breaking waves). This allowed capacitive wave wires (developed at NOC) mounted on the top section of the buoy to measure wave height and, from this, detect breaking waves.

4.3 Equipment

The theory described in chapter 3 is the basis for the two different types of acoustic measurements that were taken on the sea trials. Section 3.2 describes how measurements of attenuation can be inverted to produce a bubble size distribution. Section 3.3 describes how the measurement of pulses reflected off the sea surface and sub surface bubble clouds can be used to calculate volumetric backscatter strength. Each of these experiments has equipment specific to those measurements. The majority of the equipment, however, is shared by both experiments. The following subsections detail the equipment used.

4.3.1 Power management and distribution

A total of three Deep Sea Batteries are mounted on the very bottom section of the buoy, two of which are used for the acoustic systems, the other is used for the wave wires, cameras and positioning equipment. The two voltages from the batteries were 12 V and 24 V. Table 4.3.1 shows the different voltages

(a)

(b)

Figure 4.2: Panel (a) shows the spar buoy (in a horizontal position) as it is deployed into the Atlantic Ocean. The skewed perspective makes the yellow (top) section appear longer than the bottom section. The bottom section is, however, longer than the top section. Panel (b) shows the spar buoy as it sits in the water, with the top section protruding above the surface.

required by each piece of equipment in the acoustic system. In order to

Equipment	Voltage Required
Computer	+5 V, +12 V
Hydrophone Pre-amplifiers	± 12 V
Optical Amplifier	+ 12 V
DAQ Multiplexing Board	± 12 V
Power Amplifier Drivers	± 12 V
Power Amplifiers	± 48 V

Table 4.2: Required voltages for each piece of equipment in the acoustic system.

produce these voltages, Vicor DC-DC Converter Modules were used. The outputs from the modules were connected to a distribution board from which the necessary voltages were supplied to each piece of equipment.

4.3.2 Controlling the equipment

The buoy was to be free floating and autonomous so a suitable control system had to be developed. At the heart of the system was a MagnumX 1000 Single Board Computer running Windows XP. This computer has an average power consumption of approximately 12 W as opposed to a typical desktop computer, which would use upwards of 100 W. It was important to keep the power consumption as low as possible since power would potentially be the limiting factor in how long the acoustic system could acquire data for. A low power unit will also produce far less heat, which aids the prevention of potentially damaging condensation forming inside the housing. Script files were written in Mathworks MATLAB® and were then compiled to run as executable files upon Windows startup. These scripts controlled the timings of each of the measurements as well as generating the acoustic waveforms that were sent out into the water. The received waveforms were recorded straight onto a Seagate Momentus hard drive. These hard drives are of the 2.5" form factor as opposed to the standard 3.5" form factor. Standard hard drives would have a high probability of failing under the shock and motion

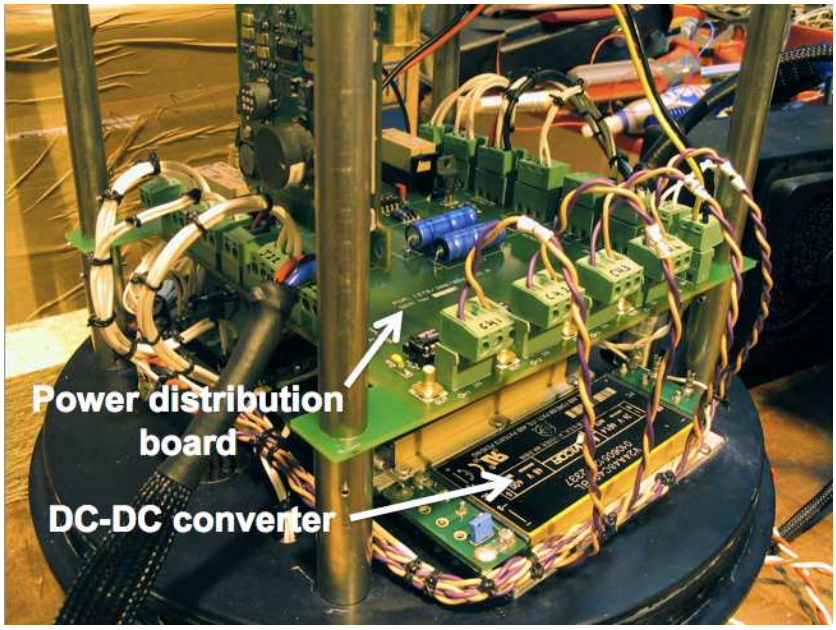

Figure 4.3: The power distribution board with all the connections in and out of it. One of the DC-DC converters is also visible. For perspective, the diameter of the end cap (the black disk upon which everything is mounted) is 304 mm in diameter.

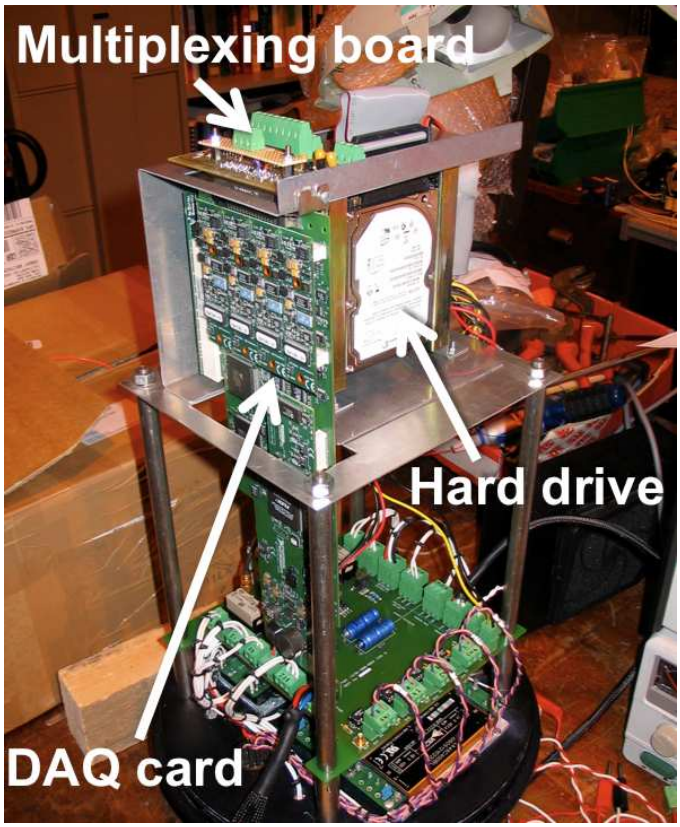

Figure 4.4: The computer mounting assembly with hard drive, MagnumX (under the hard drive, hidden from view), DAQ card and multiplexing board.

they would experience on the buoy whereas the 2.5" form factor drives are far more resilient to the violent motion at the sea surface. The 2.5" solid state hard drives were considered as these have no moving parts and are therefore exceptionally robust but these were decided against because of their extremely high price at the time.

The data bandwidth required of the hard drive was large and therefore it was important to ensure the 2.5" hard drive (which, by nature, is slower than a 3.5" hard drive) would be able to handle the volume of data coming in from the acquisition card. At any one time, the acquisition card could be acquiring data on 4 channels at a maximum sampling rate of 1 MHz. This gives a maximum bandwidth of

$$4\,\text{channels} \times 1\,\text{MSamples/s} \times 2\,\text{bytes/sample} = 8\,\text{MB/s}.$$

The manufacturers specification for the hard drive states a maximum sustained transfer rate of 44 MB/s, though independent tests (www.tomshardware.com) suggested that after sustained periods of data transfer the rate may drop to approximately 22 MB/s. Even with this drop in transfer rate, the hard drive can comfortably maintain the required bandwidth.

4.3.3 Data acquisition

As previously mentioned, all acoustic waveforms were generated on the computer and therefore had to be converted from digital signals to analogue signals. The received waveforms would also need to be converted from analogue signals to digitals signals. These procedures were carried out by a National Instruments PCI-6110 DAQ card plugged into the computer. This is a multifunction data acquisition card allowing simultaneous sampling over multiple channels for both input and output data at high sampling rates (a sample rate of 1 MHz per channel was used throughout the experiments). The card's two available analogue outputs were both used, one sending signals to the low frequency side of the amplifier, the other sending signals to

the high frequency side of the amplifier.

For the second sea trial, optical fibre sensors (developed by Ping-Chang Hsueh of the University of Southampton, under the supervision of Professor T. G. Leighton) were added to the system to provide an additional measurement of the bubble size distributions. This meant the data acquisition cards maximum number of input channels (4) was exceeded. A multiplexing board was custom designed and built (by technicians at the ISVR) to fit onto the data acquisition card. Sending a digital signal from the acquisition card to the board would switch between two banks of 4 input channels, increasing the number of available channels to 8 (though only 4 could be used simultaneously).

4.3.4 Power amplification

The design requirements for the power amplifiers were such that an off-the-shelf amplifier could not be used since no existing battery-powered amplifier can operate over such a broad range of frequencies (2-200 kHz) at the required power levels. Therefore the amplifiers had to be custom designed. In bubbly environments, attenuation is high and therefore the transmit level from the transducers must be as large as possible. A target level of approximately 190 decibels at 1 metre was set.

The realisation of these amplifiers was made possible by Paul Doust, at the time working for Blacknor Technology, who is an expert in the field of amplifier design and construction as well as transducer matching. He designed an amplifier with two halves - one to amplify the high frequencies and one to amplify the low frequencies.

As part of the amplifier, matching circuits were built-in for each of the transducers in order to flatten the frequency response of each transducer and extend the usable range [90]. This is necessary because of the resonance inherent in any transducer causing the transducer to radiate far more energy at its resonant frequency than at the frequencies above and below resonance.

As with the other electronics, the power amplifiers were contained in an

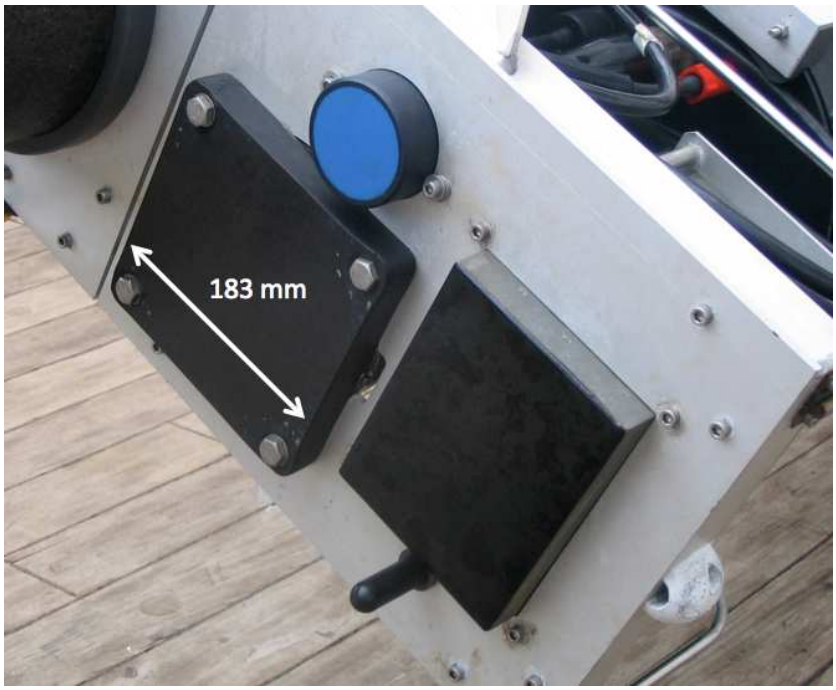

Figure 4.5: The three transducers mounted on the buoy. The square faced one is the low frequency transducer, the round one is the mid frequency transducer, and the rectangular one is the high frequency transducer. The hydrophone used for the inverted echo sounder system is also visible.

underwater housing, mounted on the buoy (see section 4.3.7). Being in an enclosed space can cause overheating issues but this was overcome by sinking the amplifier chips into one of the end caps of the housing, thus dissipating the heat into the water rather than into the air in the housing.

4.3.5 Transmit transducers

In order to cover the required frequency range (2-200 kHz), a total of three transducers were used. A Massa 137D transducer was used for the low frequencies. This transducer has a usable frequency range of approximately 2-11 kHz.

A custom made piston transducer, supplied by Neptune Sonar, was used for the mid frequencies. Piston transducers are naturally directional and very

efficient, which is ideal for this application. The transducer is resonant at 24 kHz and with the matching circuits mentioned in the previous section has a usable frequency range of approximately 15-30 kHz.

The third transducer, used for high frequencies, is another custom designed and built transducer. The transducer has previously been used to measure bubble populations in the field [8, 28, 84] and has also been used in laboratory experiments [91]. This transducer was also designed and developed with Paul Doust, who at that time was working with Thorn Marine Systems. The transducer actually has three elements inside, each one covering a different frequency range. In this experiment however, only two of these elements were used giving a total frequency range of 30-200 kHz.

4.3.6 Hydrophones

The design criterion for the hydrophone system was challenging. The hydrophones were to be mounted close to the sea surface, whereas the data acquisition equipment was to be mounted in the housing at the bottom of the buoy. This poses a problem of signal-to-noise ratio as the signals need to travel long distances along the cables before they are recorded, increasing the possibility of interference and noise polluting the signal. One solution to this problem would be to use hydrophones with built in pre-amplifiers which could boost the signals before they are transmitted along the cables, thus greatly increasing the signal-to-noise ratio. There is however a very limiting disadvantage to this solution. The near surface ocean can be a very turbulent and chaotic environment and therefore the hydrophones could be damaged by debris. The hydrophones were also to be mounted on arms protruding from the buoy and could easily be knocked and damaged during deployment and recovery of the buoy from the ship. Therefore it would be very costly to replace a hydrophone and a pre-amplifier as opposed to just a hydrophone, especially with an already tight budget.

The solution that was decided upon was to use hydrophones with short cables connected to a pressure housing containing pre-amplifiers mounted

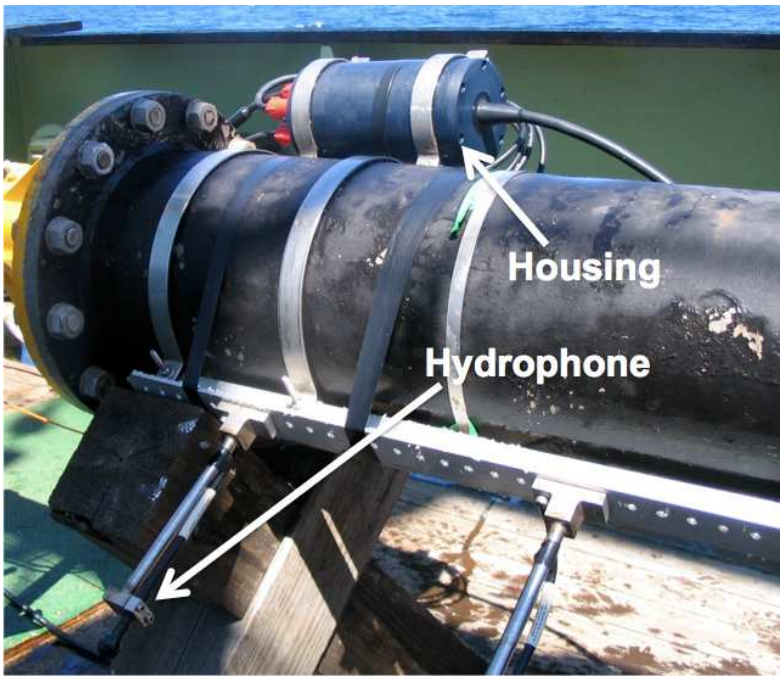

Figure 4.6: The pre-amplifier housing mounted just behind the hydrophones. One of the hydrophones, mounted on the protruding arm, can be seen in the bottom left of the photo.

close to the hydrophones. A long cable ran from this housing to the main housing, carrying the already amplified signals. This provided a good signal-to-noise ratio whilst only having the hydrophones, and not the pre-amplifiers, in a vulnerable position. The hydrophones used were D140 hydrophones, with a usable frequency range of 1 - 200 kHz, supplied by Neptune Sonar who also supplied the pre-amplifiers. The pre-amplifiers were designed with a 1 kHz high pass filter to filter out any low frequency noise, such as ship noise. There is a link that can be made on the printed circuit board of the pre-amplifiers to increase the gain from 20 decibels to 40 decibels.

A single B200 hydrophone, also supplied by Neptune Sonar, was mounted on the same plate as the transmit transducers (see figure 4.5). This hydrophone was used as part of the inverted echo sounder system and measured surface reflections. It has a specified frequency range of 10 Hz - 180 kHz.

Figure 4.7: The pressure housing as mounted on the buoy.

4.3.7 Other equipment

All of the electronics needed to be mounted on the buoy, and therefore had to be contained in a waterproof housing. There is a large amount of equipment and electronics associated with the acoustic system and most conventional housings are too small to fit everything in. A custom designed housing was manufactured by Neptune Sonar large enough to fit everything in. The housing is cylindrical in shape with an internal diameter of 286 mm and a length of 644 mm. There is sensitive electronic equipment on the buoy and during a deployment the buoy can be knocked against the side of the ship. In order to avoid this kind of shock occurring whilst the equipment is running, a water switch is used in conjunction with relays so that the electronics only switch on when the buoy is in the water.

All the necessary clamps to mount equipment on the buoy were designed and manufactured by the Engineering Design and Manufacturing Centre at the University of Southampton.

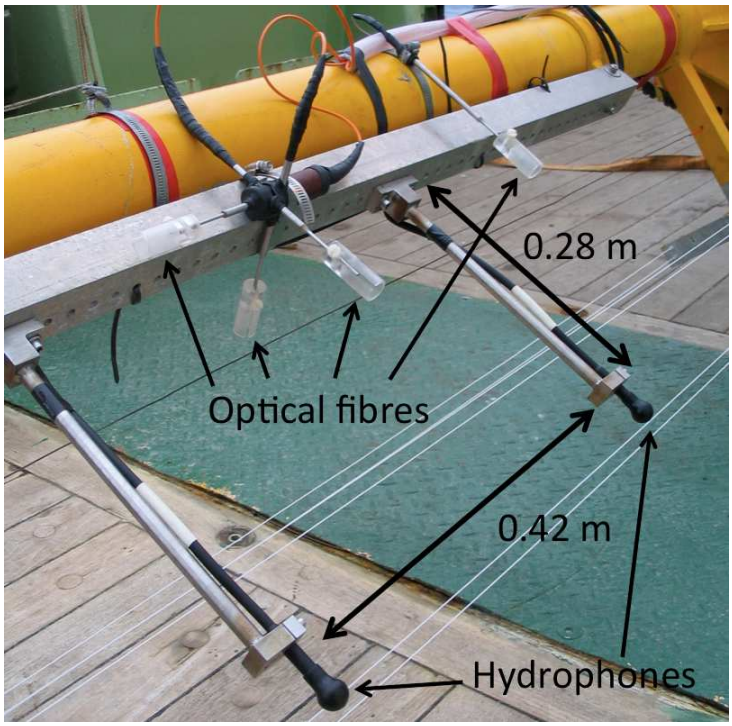

Figure 4.8: The four optical fibre sensors mounted close to the hydrophones. Three are mounted in a tri-axial array and another is mounted on its own. The fibres protrude approximately 10 mm out of the metal shaft and are protected by a cylindrical plastic housing, visible in the photograph.

4.3.8 Optical fibre system

A method of measuring bubble populations using optical fibres was implemented by Ping-Chang Hsueh, a PhD student of Professor T. G. Leighton at the ISVR. Light is shone down a fibre and the reflection coefficient at the tip is measured. This reflection coefficient varies dramatically depending on whether the tip is in air (i.e., a bubble, or water) and bubble populations can be inferred from a recorded time-series [92, 93]. Optical fibres were mounted close to the hydrophones in order to provide a secondary measurement of the sub-surface bubble populations. Power for the optical amplifier is taken from DC-DC converters inside the main electronics housing. The measured data is recorded on the hard drive inside the main electronics housing.

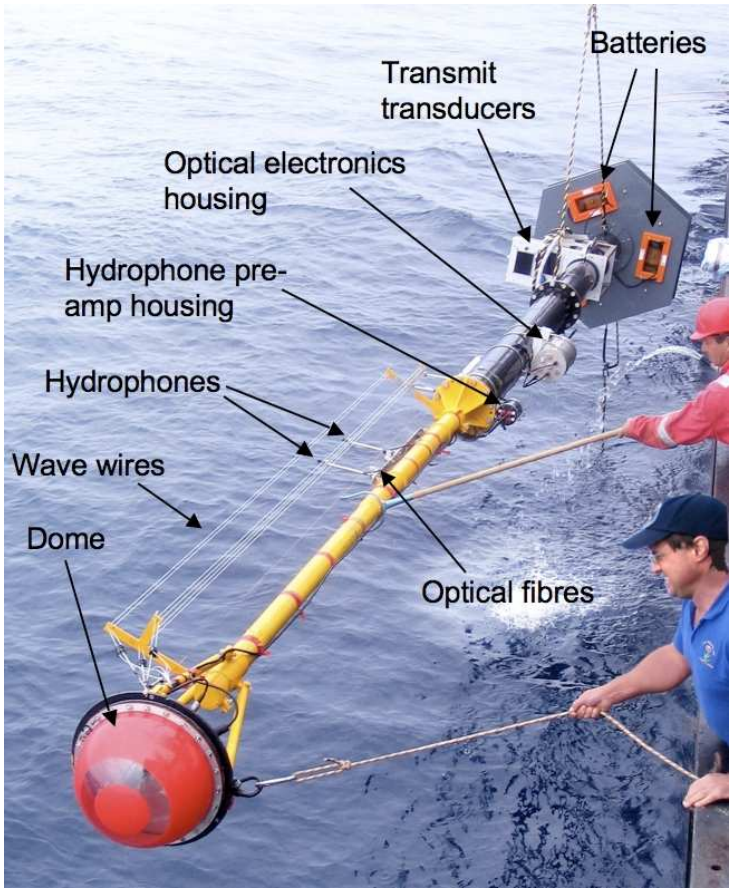

Figure 4.9: The buoy being deployed on D320.

4.3.9 Equipment summary

The system as a whole performed very satisfactorily and the recorded waveforms followed those that had been transmitted with high fidelity.

4.4 D313 Cruise

The first sea-trial was on the *RRS Discovery* on Cruise D313. The sea trial was scheduled from 6th November to 14th December 2006, with the ship leaving from and returning to Govan, Glasgow. The intended area of operation was north-west of the Scottish Outer Hebrides in the North Atlantic, though

the exact route was dictated by weather conditions.

For almost the entire duration of the cruise, there were severe storms in the North Atlantic. This made carrying out scientific experiments very difficult. Almost all of the experiments on the cruise suffered as a result as the ship spent much of its time sheltering from the storms amongst the Scottish Islands. This had very obvious implications for the acoustic experiments as bubble clouds are only formed under breaking waves, produced by rough weather. In sheltered water, there are very few breaking waves and therefore few sub-surface bubble clouds. As is described in section 4.4.2 there were actually some breaking waves during the time periods in which the buoy was deployed, though it was difficult to measure these.

The timing of the beginning of D313 had left little time for system preparation and testing. Therefore one of the main objectives of the first cruise was to test all of the systems, discover what they were capable of, and optimise the experiment to produce the best results. With this in mind, each deployment was planned to last a few hours in duration. It was also planned to keep the buoy within sight of the ship so as not to rely on the positioning systems at such an early stage.

4.4.1 Hydrophone spacing and signal levels

On D313, only attenuation measurements were made. These measurements were the most important to make and therefore time was spent getting that system working as it should. This, however, meant that the inverted echo sounder system was not used at all on the first cruise.

The array of hydrophones was mounted on the buoy so that the distance from the first hydrophone to the transmit transducers was 3.86 metres. The spacing between each hydrophone was 0.20 metres. When the buoy was in the water, the average depth of the hydrophones was approximately 3 metres. This was the shallowest the hydrophones could be mounted at that stage since there were only clamps available to fit them onto the wide section of the buoy and not the top section. Three of the four hydrophones were used

Figure 4.10: The three hydrophones used on D313. The photograph looks down the buoy towards the base, and the transmit transducers are visible in the background. Hydrophone separation is 0.2 m and the distance from the hydrophone furthest from view to the transmit transducers is 3.86 m.

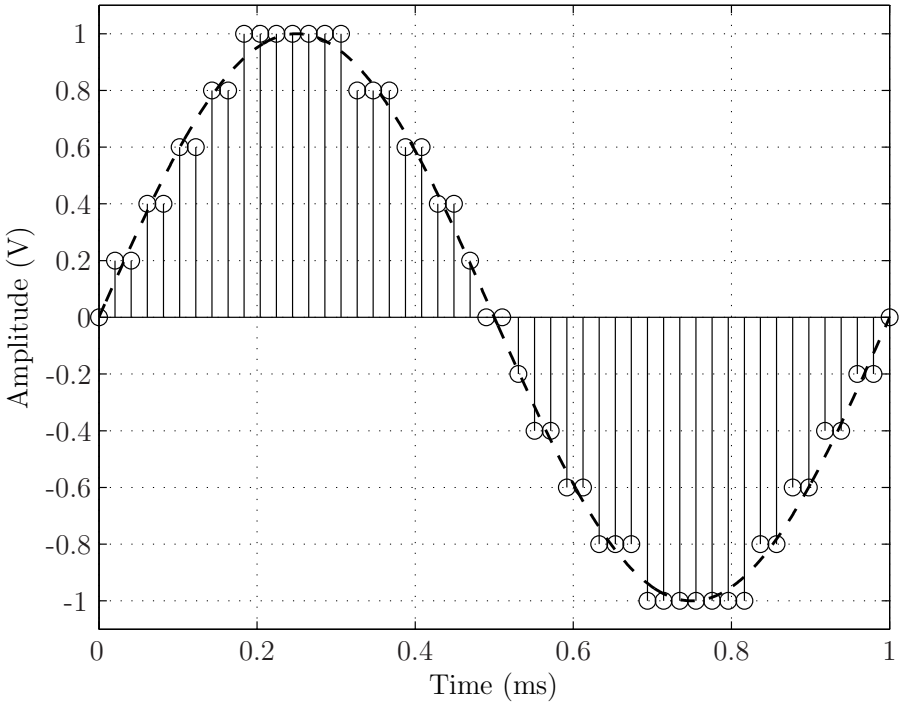

Figure 4.11: An example of quantisation noise created using artificial data.

since this would give bubble size distributions at more than one depth and yet leave one hydrophone to keep as a backup in case one of the hydrophones was damaged.

As was mentioned earlier, time for pre-cruise testing was very limited and therefore various gain levels had not been optimised before the cruise. The input voltage range for the data acquisition also had to be chosen carefully. If the range is too small, there is the risk of clipping signals at a higher level. If the range is too large, there is the possibility of quantisation noise. Quantisation noise occurs as the analog signals coming into the DAQ card are digitised. Figure 4.11 shows how sampled points are moved to the nearest quantisation level and therefore they do not exactly represent the original signal. The DAQ card used in the experiments is a 12 bit card, providing 4096 (2^{12}) levels of quantisation. This means that if the input voltage range is set to $\pm$ 10 V, the card can achieve a resolution of 4.8 mV. For a signal

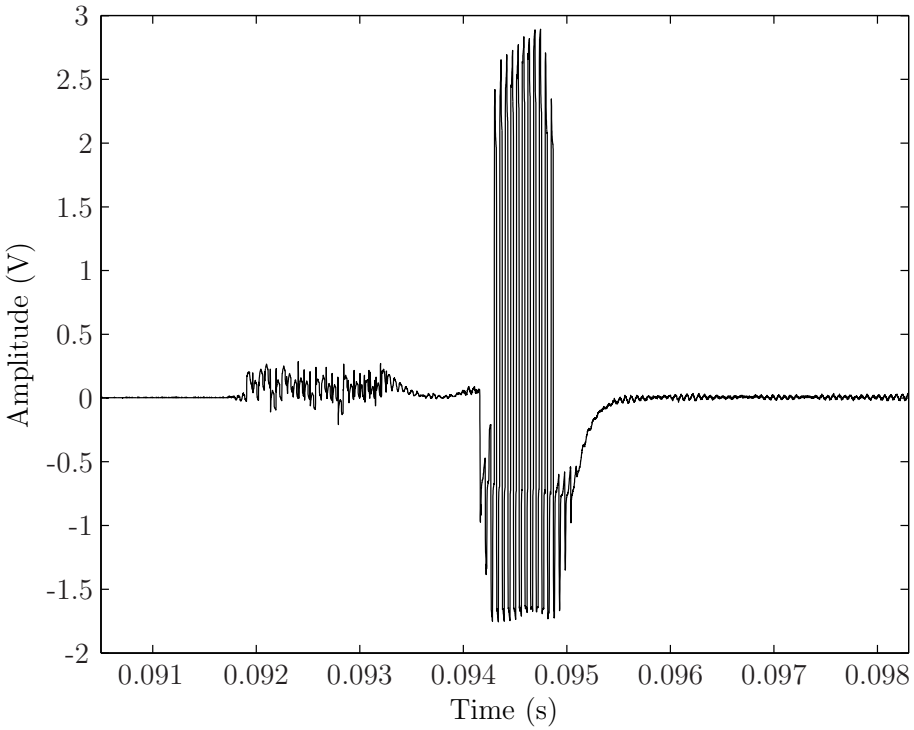

Figure 4.12: A recorded waveform from the hydrophone tests. This type of signal is very suggestive of saturation of the pre-amplifier.

at 185 dB, this would introduce a potential error of 0.035 dB which can be assumed negligible.

It was also important to ensure the optimum sound pressure level in the water. The brief tests that were carried out prior to the cruise showed that it was possible to drive the hydrophone pre-amplifiers into saturation if the sound pressure level is too high (see figure 4.12). The script files were therefore set up to run through differing values of both the peak to peak voltage sent to the power amplifier and the input voltage range of the data acquisition card.

4.4.2 Deployments

A total of four deployments were made on the first sea trial. With this being the first real test of the equipment, each deployment highlighted faults and areas of the system that could be improved. This section details each deployment and what was learnt from each one.

Deployment 1

The first deployment was made on 8th November 2006 in calm water (sea state 2) soon after leaving port (in the Mull of Kintyre) and was very much a test deployment. The purpose of this test was threefold. The buoy is 11 metres long and weighs almost half a tonne and therefore handling the buoy and deploying and recovering it from the water is not trivial. The calm water test gave the ship crew a chance to practice handling the buoy. All the systems on the buoy had not yet been tested together so the first deployment was also a chance to do that. Thirdly, a bubble free attenuation measurement is required in order to calculate the additional attenuation induced by bubbles to use in the inversion. This would have to be carried out in calm, bubble free water.

For the deployment, the ship was positioned in a way to shield the buoy from wind as it was deployed. The consequence of this was that when the buoy was in the water, the wind started to blow the ship over the buoy and the buoy began to be dragged under the ship. Fortunately this was realised before any major damage occurred and the buoy was winched back out of the water. The ship was then repositioned in a way that it would be blown away from the buoy as it was deployed. This was the positioning for all subsequent deployments.

Unfortunately, upon recovery of the buoy and connection to the onboard computer, it was discovered that no acoustic data had been taken. It appeared as if the computer had never even turned on. After extensive testing, it was discovered that the fault was caused by the Windows screensaver turning on, interrupting the executable script file and aborting the program. This

Figure 4.13: Conditions during the second deployment.

was easily fixed by disabling the screensaver. All other power saving features of Windows were also disabled in order to prevent further interference.

Deployment 2

The second deployment was on 19th November 2006. There was moderate wind throughout but not very much white capping (sea state was a developing 3). The physical deployment of the buoy went without complication. The buoy was in the water for just over 2 hours. The buoy was recovered and it was found that data had been successfully acquired. However, even with the lowest output voltage to the power amplifiers, the hydrophone pre-amplifiers were overloaded by the sound pressure level in the water (see figure 4.14). As was mentioned in section 4.3.6, the hydrophone pre-amplifiers were designed with the ability to adjust the gain for this very purpose. A link on each printed circuit board could be desoldered and this reduced the gain by 20 dB, from 40 dB to 20 dB. There was no way to test the system onboard

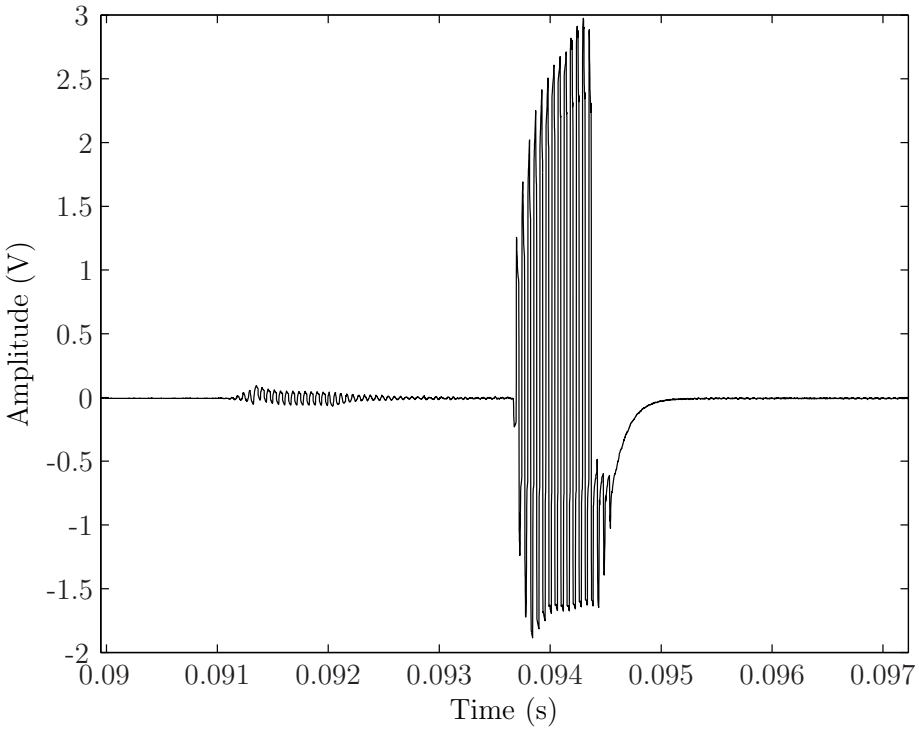

Figure 4.14: A signal received by the computer from one of the hydrophone pre-amplifiers during the second deployment. The signal shows the same characteristics as the signals from the pre-cruise tests (see figure 4.12) and is typical of a saturated pre-amplifier.

Figure 4.15: Conditions on the third deployment of Cruise D313.

the ship so the results of this adjustment would be discovered on the third deployment.

Deployment 3

The third deployment was made on 20th November 2006. Although positioned in sheltered water, there were occasional breaking waves (sea state was a developing 3). The buoy systems performed well and for the first time, good quality acoustic signals were recorded. There was, however, another problem. Of the 14 pulses sent out from the computer, only the first 6 could be seen on the received waveforms. The cut-off point coincided with the split between the low frequency and high frequency sides of the power amplifier. This was a major problem, with many potential causes. Each cable in the signal path was checked and found to be working. The output from the data acquisition card (which has a separate channel for both the high and low frequencies) was checked and found working. The transducer was unlikely

to be the cause of the problem since it was working before the cruise and was packed very well in transit from Southampton to the ship. This left the power amplifier as the cause of the problem which is one of the most complicated pieces of equipment and very difficult to fix. Despite this, upon a thorough visual inspection of the power amplifier, an internal spade connector was found to be connected incorrectly, forming a weak link between the amplifier and the matching circuits. This would have presented a far higher impedance to the amplifier than normal and was very likely be the to cause of the problem. Having reseated the connector as it should have been, the buoy was hung over the side of the ship for a short period of time in order to test it. The data recorded on the test showed pulses at all 14 frequencies[1].

Deployment 4

The fourth deployment was in sheltered water near the Isle of Eigg (sea state 4) on the 29th November 2006 and was the first deployment with a fully operational acoustic system. The intended duration of the deployment was five or six hours, but owing to a rapidly descending mist the decision was made to recover the buoy after approximately two hours as it was becoming very difficult to maintain visual contact with the buoy. Data was recorded, but no discernible attenuation was evident in the data.

4.4.3 D313 summary

The first sea-trial was a very good opportunity to test the buoy as a complete working unit. Faults in the system were discovered and corrected and areas of improvement were highlighted (see section 4.4.4). The main success was to establish a fully working, fully autonomous acoustic system capable of measuring bubble populations in deep ocean.

The acoustic data that was taken showed little attenuation. This was due to the deployments only being possible in sheltered water as opposed

[1]Much to the author's relief.

to in open ocean, and also because the hydrophone array was mounted too deep for the bubble clouds to have a noticeable effect on the acoustic pulses. This meant that for the second sea trial, new brackets were manufactured, allowing the hydrophones to be mounted on the top section of the buoy.

No damage was incurred upon the buoy except for partial damage to the water switch causing some of the protective plastic casing to break off. Because of this, a raindrop passing across the sensor can engage the switch so care must be taken on deck to ensure this does not happen. Other than that, the switch is still fully functional.

4.4.4 System refinements

A number of possible refinements were highlighted during the first cruise. Deploying the buoy in anything other than calm water was discovered to be very difficult. Yet if data is to be taken during rough weather, a workaround needs to be developed. Ideally, the buoy would be deployed in calm water a couple of days ahead of a storm. Data would be taken throughout the storm and then, when the weather had calmed, the buoy would be recovered. This would result in deployments of days rather than hours as it had been in the first sea trial. With a maximum battery life of approximately 12 hours, it was clear the acoustic system would need a form of timing device to delay system startup until the storm was overhead. As a solution, a Finder 86 series timer module was installed between the water switch and the startup relays inside the main pressure housing. The timer module could delay the system startup for up to 100 hours (approximately 4 days) which was more than sufficient. Another discovery was that with the pressure housing containing the computer and power amplifiers being so heavy, lifting it to and from, and mounting it on the buoy was not trivial. It was seen as the most involved process in preparing the buoy for each deployment. Downloading the data whilst the housing was still on the buoy would make things very much easier. So an extra bulkhead connector was fitted in one of the end caps. Inside the housing, the 8 pins on the connector were attached to an

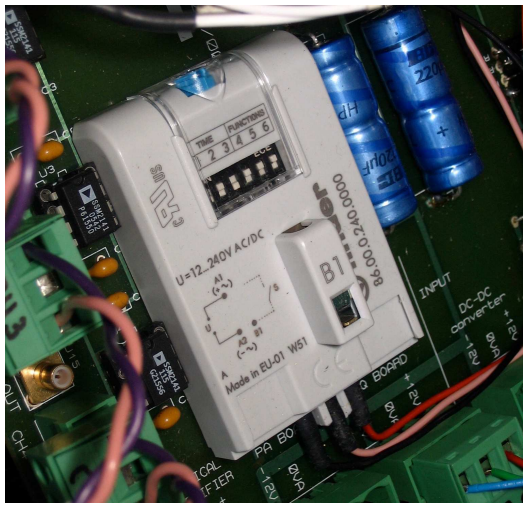

Figure 4.16: The Finder 86 series timer module.

ethernet cable running to the onboard computer. Outside of the housing, an ethernet cable was spliced onto a cable designed to mate with the bulkhead connector. This allowed remote access to the onboard computer from a laptop, which simplified the data downloading process dramatically. Powering the computer on deck was not trivial however. Previously, power to the housing would be initiated by the water switch and it was easy to short the contacts on the switch to override this. However, with the timer module now in place, power would not be supplied to the housing (and therefore the onboard computer) until the timer had finished which was typically 50 hours. This would negate any time savings brought about by being able to access the data on the computer remotely. To solve this problem, a reed switch was installed on the inside of the end cap. When a magnet was held against the correct place on the end cap, the reed switch would be activated and bypass the timer module, thus supplying power instantly to the computer.

Time synchronisation of the acoustic system and wave wire system was an important issue to resolve. It is something that had not been properly addressed for the first cruise. This made it difficult to synchronise breaking wave events occurring on the wave wire data and video data with the acoustic

data. This problem was solved by synchronising both systems with the ships clocks (set to Greenwich Mean Time) before each deployment. This would allow synchronisation accuracy within one or two seconds. The ambiguity arises because of an inherent drift within the clock on the computer causing a small error over the duration of the deployment.

4.5 D320 Cruise

The second and final sea trial took place from 16th June to 18th July 2007 on the *RRS Discovery*. The ship sailed from Falmouth and returned to Govan, Glasgow. The area of operation was in the North Atlantic, approximately 400 miles west of Portugal.

This sea trial had the potential to be very successful. Much had been learnt from the first sea trial, system refinements had been made, and the potential for quality data had increased greatly.

As well as the acoustic system for measuring attenuation, there was to be an upward looking echo sounder to measure the reflections of an acoustic pulse from the sea surface and sub-surface bubble clouds. Passive recordings were also to be made in an attempt to record a breaking wave as it happens and therefore infer an initial bubble population [94].

The weather conditions for the second cruise were completely different from the first cruise. The sea state was fairly calm throughout and the air temperature was generally far higher. This made deploying and recovering the buoy much easier, though posed its own problem in that without wind and breaking waves there would be no sub-surface bubble clouds to measure.

The following subsections describe the details of each of the deployments and table 4.7 gives a summary of the geographic locations and general details of all the deployments.

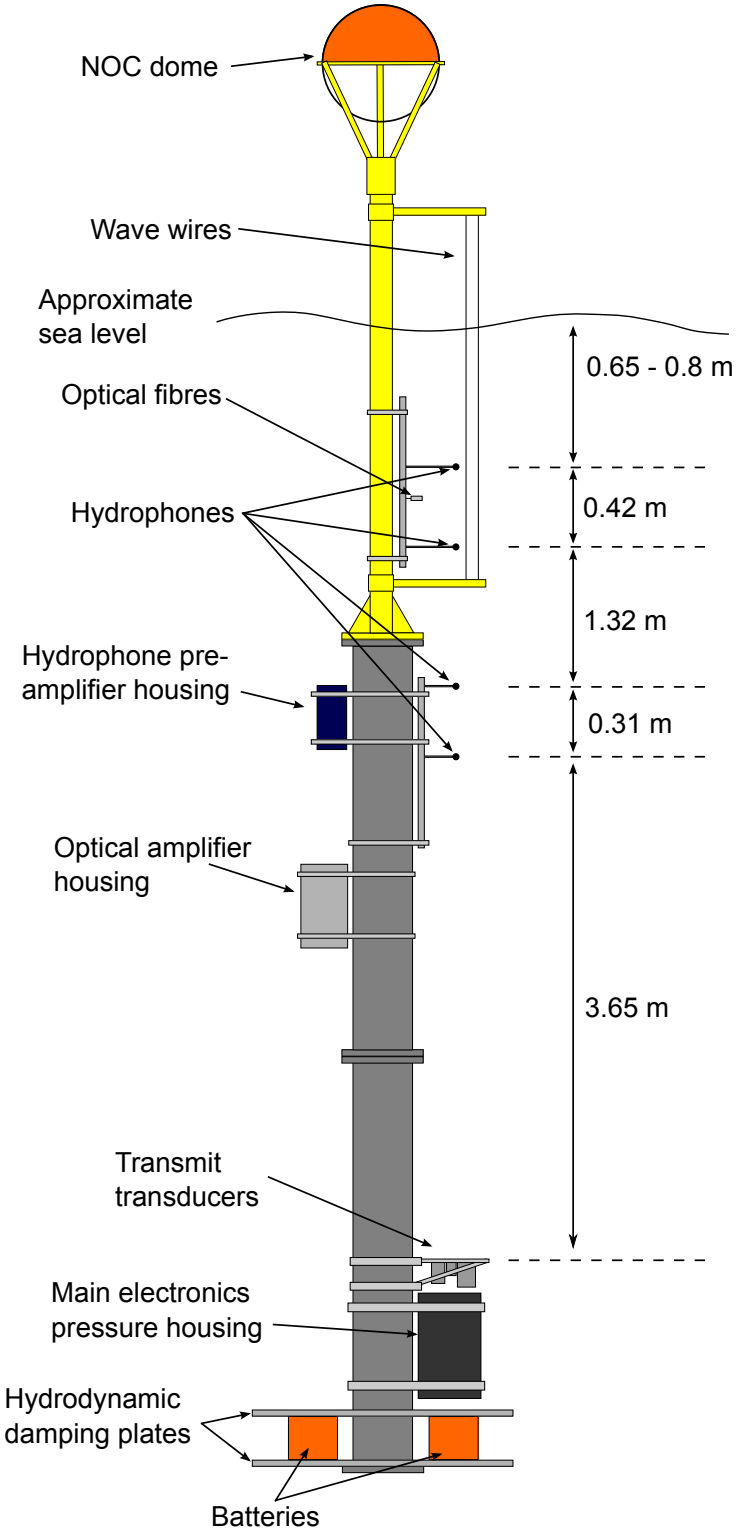

Figure 4.17: Schematic (not to scale) showing the arrangement of the buoy for the D320 cruise.

Hydrophone Position	Distance from transmit transducers	Distance from sea surface	Serial number	Pre-amplifier Gain
1	3.65 m	2.85 m	18878	20 dB
2	3.96 m	2.54 m	18879	20 dB
3	5.28 m	1.22 m	18880	20 dB
4	5.70 m	0.80 m	18881	20 dB

Table 4.3: Hydrophone arrangement details for deployment 1.

4.5.1 Deployment 1

The onboard computer had some problems before the first deployment. It was running slower than usual and would occasionally crash when running the script files on the workbench. This lack of reliability could not be depended upon for the deployment so the code was heavily reduced to include only the attenuation measurements. With this reduction, the computer seemed to run more stably and so the decision was made to use the shortened version of the code. It was later discovered (before the second deployment) that the problem with the computer was caused by a corruption of the PCI and IDE buses on the motherboard. This was resolved by a system reinstall.

With the new clamps, hydrophones could be mounted on the top section of the buoy, much closer to the surface than on the first sea trial. Four hydrophones were used for the first deployment in an attempt to work out the optimum spacing and depth of the hydrophones. This deployment was made on 22nd June 2007 and was longer than any of the previous deployments at just over two days. It was also the first deployment that the ship left the area of ocean that the buoy was deployed in. This meant that the positioning equipment had to be relied upon to find the buoy again before recovery. This equipment operated as expected and finding the buoy was not difficult.

The weather conditions throughout the deployment were calm (see figure 4.19). There were no visible white-caps (sea state 3). These conditions were good for taking a bubble free baseline measurement.

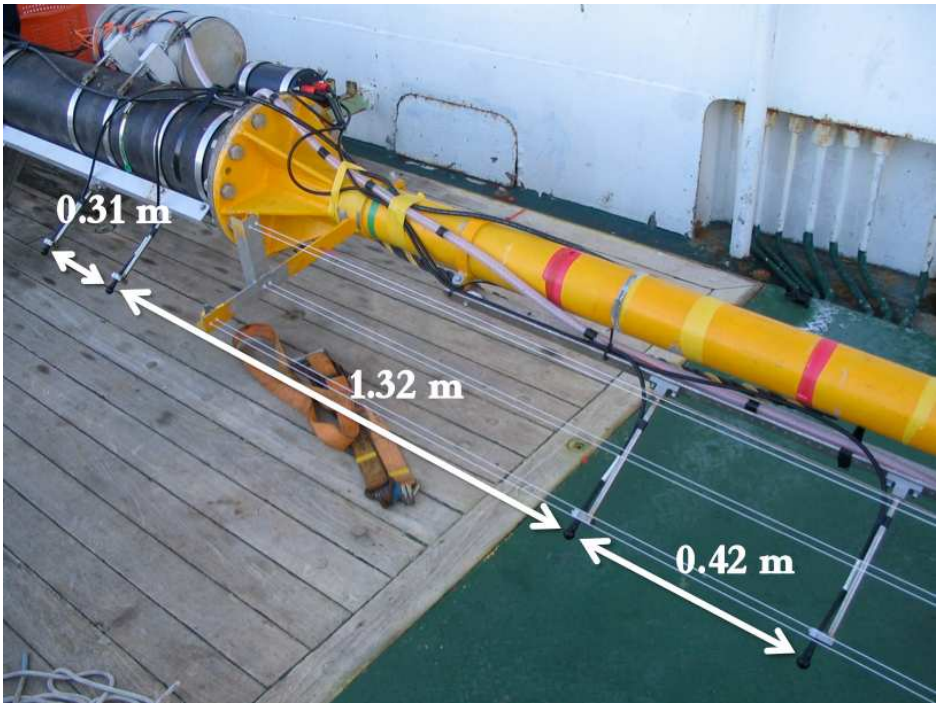

Figure 4.18: Hydrophone spacing for deployment 1 of D320. Approximate distance from the top hydrophone to the sea surface was 0.8 m. The distance from the source transducers to the first hydrophone was 3.65 m.

Figure 4.19: Conditions for the first deployment on D320. The sea state was very calm and there were no breaking waves.

4.5.2 Deployment 2

The second deployment on Cruise D320 was the most successful deployment of the two cruises. The results obtained from this deployment are discussed in detail in Chapter 5.

After almost two weeks of calm weather, hope of a large quantity of breaking waves was diminishing. However, each day, the weather forecasts were studied. A strong weather front was discovered heading towards the area of operation. The front was tracked and a prediction was made as to when it would reach the ship's position.

The buoy was deployed at 17:31 GMT on 28th June 2007, one day before the weather front was predicted to arrive. The start delay timer was set to approximately 18 hours (the timer uses an analog dial with only zero and 100 on the scale). This actually turned out to be nearer 19 hours so the equipment turned on at approximately midday on the 29th June 2007.

Figure 4.20: Weather conditions in the time period that acoustic data was recorded on the second deployment of Cruise D320.

The acoustic system took data for about 12 hours until the charge in the batteries was depleted. The weather conditions during the deployment were excellent. The number of breaking waves was the highest it had been for the sea trial (sea state 4-5). Figure 4.20 shows one such breaking wave as it passes the ship. It was difficult to capture the frequency of breaking waves in a still image but many white-caps can be seen in the photo. The buoy was recovered at 18:52 GMT on 1st July 2007. Upon recovery, the buoy was sitting noticeably lower in the water. This was later discovered to be caused by a leak in the optical fibre pre-amplifier housing. This housing was half full of water which significantly reduced the buoyancy of the buoy, causing it to sit lower in the water. The difference was approximately 0.15 metres. With the computer problems fixed, it was possible to run the inverted echo sounder and passive acoustic systems as well as the attenuation system for

Hydrophone Position	Distance from transmit transducers	Distance from sea surface	Serial number	Pre-amplifier Gain
1	3.65 m	2.85 m	-	-
2	3.96 m	2.54 m	18878	20 dB
3	5.28 m	1.22 m	18879	20 dB
4	5.70 m	0.80 m	18880	20 dB

Table 4.4: Hydrophone arrangement details for deployment 2. No hydrophone was used in position 1.

(a) (b)

Figure 4.21: Panel (a) shows the buoy just after deployment, sitting at the correct depth and panel (b) shows the buoy just before recovery sitting lower in the water. The timing of passing waves slightly exaggerates the depth difference.

Hydrophone Position	Distance from transmit transducers	Distance from sea surface	Serial number	Pre-amplifier Gain
1	3.65 m	2.85 m	18881	40 dB
2	3.96 m	2.54 m	18878	20 dB
3	5.28 m	1.22 m	18879	20 dB
4	5.70 m	0.80 m	18880	20 dB

Table 4.5: Hydrophone arrangement details for deployment 3.

this deployment. This meant only three hydrophones could be used in the attenuation array, with the fourth channel of the DAQ card being used by the hydrophone for the inverted echo sounder. The three hydrophones used in the attenuation array were also used for the passive recordings. The positions of the hydrophones were the same as for the previous deployment, only the deepest position was not used. The hydrophone for the inverted echo sounder was mounted in the same plate as the transmit transducers and can be seen in figure 4.5.

4.5.3 Deployment 3

The third deployment was made on the 4th July 2007 at 10:47 GMT. The leak in the optical fibre housing had damaged one of the optical amplifier channels so only three channels were used for that system. This allowed an extra hydrophone to be used in the acoustic system.

Attenuation data from the second deployment was good so adjustments to the gains of the hydrophone pre-amplifiers were made in an attempt to improve the quality of the passive recordings. As was mentioned in section 4.3.6, the gain of the hydrophone pre-amplifiers can be increased by 20 dB by soldering a link in at the correct point in the circuit. This extra gain was added to the hydrophone with serial number 18881. Weather conditions were far from ideal for breaking waves (sea state 3-4). The sun shone and the sea state was calm (see figure 4.22). The main benefit of this deploy-

Figure 4.22: Conditions on 6th July, the day the acoustic system was recording data on the third deployment.

ment would be to the NOC systems on the buoy. The capacitive wave wire data acquisition system had been having problems and frequently stopped acquiring data for no obvious reason. So after attempts were made to resolve the problem, the scientists were keen to test the system again with another deployment.

4.5.4 Deployment 4

At 19:57 GMT on 9th July 2007, the buoy was deployed for the fourth and final time. For this deployment, another hydrophone pre-amplifier (for the hydrophone with serial number 18878) had the gain increased to 40 dB.

Hydrophone Position	Distance from transmit transducers	Distance from sea surface	Serial number	Pre-amplifier Gain
1	3.65 m	2.85 m	18881	40 dB
2	3.96 m	2.54 m	18878	40 dB
3	5.28 m	1.22 m	18879	20 dB
4	5.70 m	0.80 m	18880	20 dB

Table 4.6: Hydrophone arrangement details for deployment 4.

Weather conditions were similar to the third deployment (sea state 3-4) and not very conducive to sub-surface bubble clouds. Though this did not seem to matter since upon recovery of the buoy and downloading of the data, it was discovered that the acoustic system had only been powered for approximately 25 minutes as opposed to the usual 10 or 12 hours. It was unclear what had caused this as the batteries were charged before the deployment in the same way as for the previous deployments. One reason could have been due to the batteries being run down too much in previous deployments. For example, the 24 volt battery generally read about 11 or 12 volts after a deployment. This kind of deep discharge could have partially damaged the batteries and prevented them from being charged properly before the final deployment.

Unfortunately, as the buoy was being recovered for the last time, some of the equipment was damaged. The ship rolled as the buoy was lifted from the water causing it to swing into the side of the ship. It was then dragged along the side of the ship. This caused damage to one of the transducers and destroyed one of the hydrophones.

4.6 Summary

This chapter has detailed experiments undertaken on two sea trials as part of this project. Chapter 5 gives extensive examples of recorded data and gives an in depth description of the processing involved in turning the raw waveforms into useful acoustic data.

No.	Deployment				Recovery				Comments
	Day	Time	Latitude	Longitude	Day	Time	Latitude	Longitude	
1	22nd June	13:18	43° 42.7 N	18° 06.2 W	24th June	14:15	43° 36.3 N	18° 59.3 W	Buoy positioned near ASIS-1 buoy.
2	28th June	17:32	43° 13.3 N	17° 44.3 W	1st July	18:52	42° 44.2 N	17° 20.4 W	Deployment with most breaking waves. Leak in optical housing causing buoy to sit lower in water. Positioned near ASIS-2 buoy.
3	4th July	10:47	42° 34.6 N	16° 33.7 W	7th July	19:15	42° 41.2 N	16° 22.6 W	Leak in optical electronics housing no longer an issue. Positioned near ASIS-1 buoy.
4	9th July	19:57	43° 32.3 N	16° 06.6 W	13th July	11:24	42° 32.5 N	15° 49.4 W	Damage to hydrophone and transducer upon recovery. Positioned near 3rd SF_6 patch.

Table 4.7: Summary of the deployments of the D320 sea trail. The ASIS (Air-Sea Interaction Spar) buoys make high resolution measurements of the air-sea interface, including fluxes, turbulence, waves, and water mass properties. The SF_6 patch refers to a dual tracer method used for estimating the gas transfer velocity, K_T, based on the time dependent change in the concentration ratio of the inert gaseous tracers sulphur hexafluoride, SF_6, and helium-3, ^3He. Both the ASIS buoys and tracer patch experiments were part of the Deep Ocean Gas Exchange Experiment mentioned in chapter 1.

Chapter 5

Results and Analysis

This chapter examines the data recorded on the sea trials and describes how these data were processed to produce meaningful results. These results are then presented and discussed.

The first sea trial, D313, did not produce any useful data. The weather was generally too calm, the hydrophone array was mounted too deep, and the equipment only worked as it should have on one of the four deployments. As was mentioned in chapter 4, the main use of the first sea trial was to test the equipment and to make any necessary improvements.

The second sea trial, D320, was a great deal more successful. With the lessons learnt from the first cruise, a far more refined acoustic system could be used. Despite these improvements, only one of the four deployments returned data of a suitable quality. The first deployment was in calm waters so, as would be expected, there were no sub-surface bubble clouds. It was a very similar case for the third deployment with warm weather and flat seas. Chapter 4 described how a battery failure prevented any useful data being taken on the fourth deployment. The system did actually run for 25 minutes but generally the last two hours of data on each of the deployments were unusable. This is because as the batteries lose their charge, the voltage decreases and since the hydrophone pre-amplifiers were run straight from the batteries (rather than through a DC-DC converter), the recorded waveforms

become clipped when the voltage supplied to the pre-amplifiers is too low. This means the 25 minutes of data from the final deployment was all during this period of insufficient voltage.

The second deployment of D320 was the only deployment out of a total of eight (over two sea trials) to return usable data.[1] Fortunately this deployment produced some excellent data and it is the analysis of this data that is discussed throughout this chapter.

Two different datasets are discussed in the chapter. The first is the attenuation data which can be processed to calculate bubble populations; and the second is the inverted echo sounder data which can be processed to show a profile of the sub-surface bubble clouds. Passive acoustic data is mentioned in chapter 4 but there were no successful recordings made in this way. This is because the gains on the hydrophone pre-amplifiers were too low for passive recordings, and could not be increased because of the low gains required for the active acoustic data and budget constraints severely limited the number of hydrophones. On the third and fourth deployments the gains of some of the pre-amplifiers were increased but the weather conditions for these deployments were too calm to produce breaking waves.

This chapter presents results from two different datasets, and after that it discusses how these datasets can be used together to gain still more information about the sub-surface bubble populations.

5.1 Acoustic attenuation data

The acoustic attenuation system used a series of 14 pulses, each increasing in frequency. Figure 5.1 shows an example of the recorded waveform. Each pulses is 1 ms long with a 20 ms pause between pulses. Chapter 4 discusses

[1] Until one experiences the difficulties of conducting experiments at sea, one will not realise that even one successful deployment is considered fortunate. Many of the scientists on the first sea trial left with no data at all. It is not possible simply to repeat the experiments another day - these sea trials are planned years in advance. To run a ship like the *RRS Discovery* costs approximately £10,000 per day so it is very important to take useful data within the limits of the cruise dates.

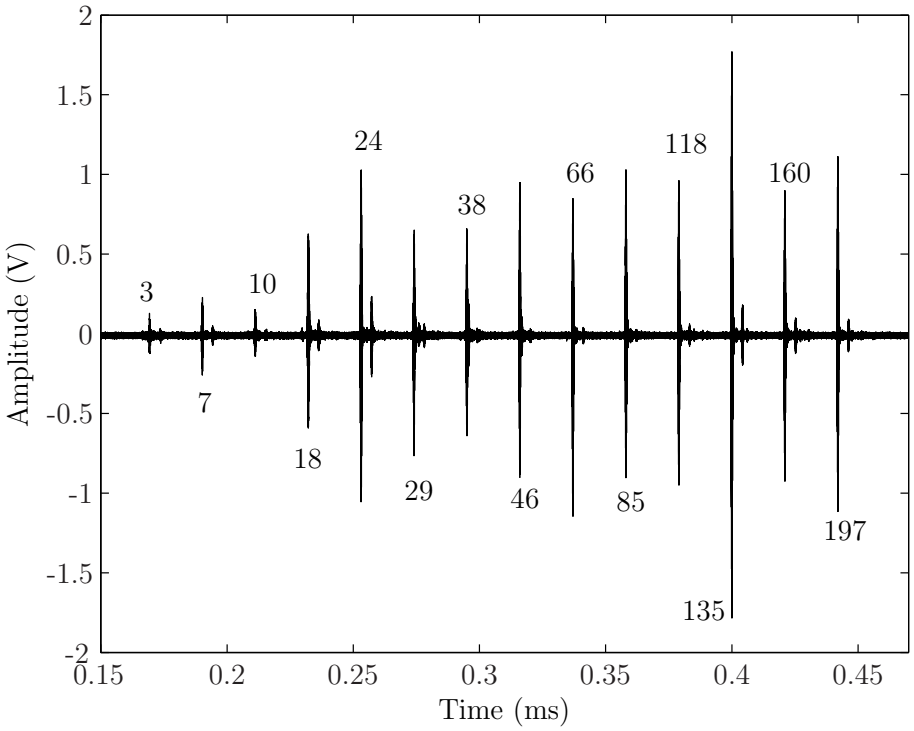

Figure 5.1: The 14 acoustic pulses as measured by the hydrophones on the sea trials, with frequencies labelled in kHz. The amplitude of each pulse respectively (in dB *re* 1 μPa) is 170, 175, 171, 184, 190, 186, 187, 189, 195, 193, 191, 198, 185 and 196.

the reasons for choosing those values and should be consulted for a more in depth description of the theory.

The train of pulses was transmitted once a second for nine seconds. There would then be a pause whilst the inverted echo sounder and the optical fibre systems ran. This sequence was continuously repeated until the battery charge was depleted. The time period between each file was approximately 2.5 minutes. For the second deployment on D320, a total of 246 files were created, each containing nine datasets (separated by a second) giving a total of 2214 pulse trains. Since each pulse train contained 14 pulses, and data was recorded on three channels, a total of over 90,000 pulses would need to be processed. This was an extremely large amount of data and would require automated processing.

5.1.1 Raw waveforms to voltage amplitudes

The first difficulty in processing was aligning the pulses. For each recording, the data acquisition system was automatically triggered by the computer. The computer was not fast enough to begin recording the incoming waveforms at exactly the same time for each data set, so the offset between the start of each data file and the first pulse changed with each dataset. To overcome this, an autocorrelation was performed using one of the original outgoing pulses. Once the position of that pulse had been found, preset windows (figure 5.2) could be placed over each of the pulses in the signal making it possible to process each individual pulse. A band-pass filter was applied and a Hilbert transform [95] taken to obtain the envelope of the pulse. The amplitude of the pulse was then measured by taking the maximum value of the envelope. This technique of finding the maximum was effective for the majority of the pulses. In some instances (less than 1% of the time) the reflected pulse was actually of a larger amplitude than the direct pulse (see figure 5.4). This could have been caused by the curvature of the surface as a wave passes producing a focussing effect. In order to solve this problem, a peak detection algorithm was written to find the two peaks with the highest amplitude. The

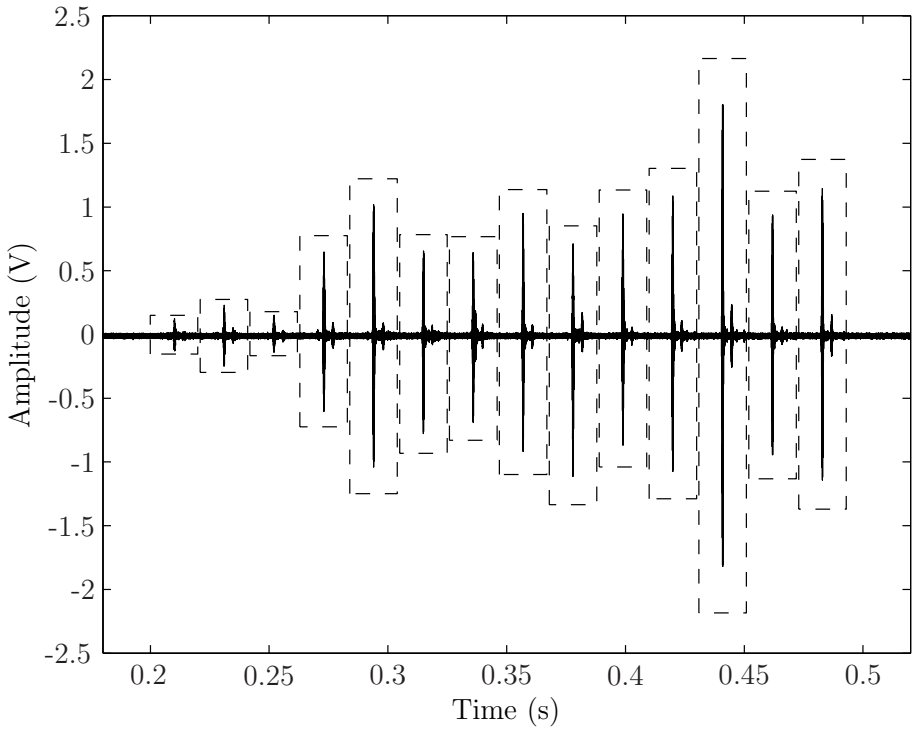

Figure 5.2: The results of the algorithm to detect automatically where the pulses were in the received signal.

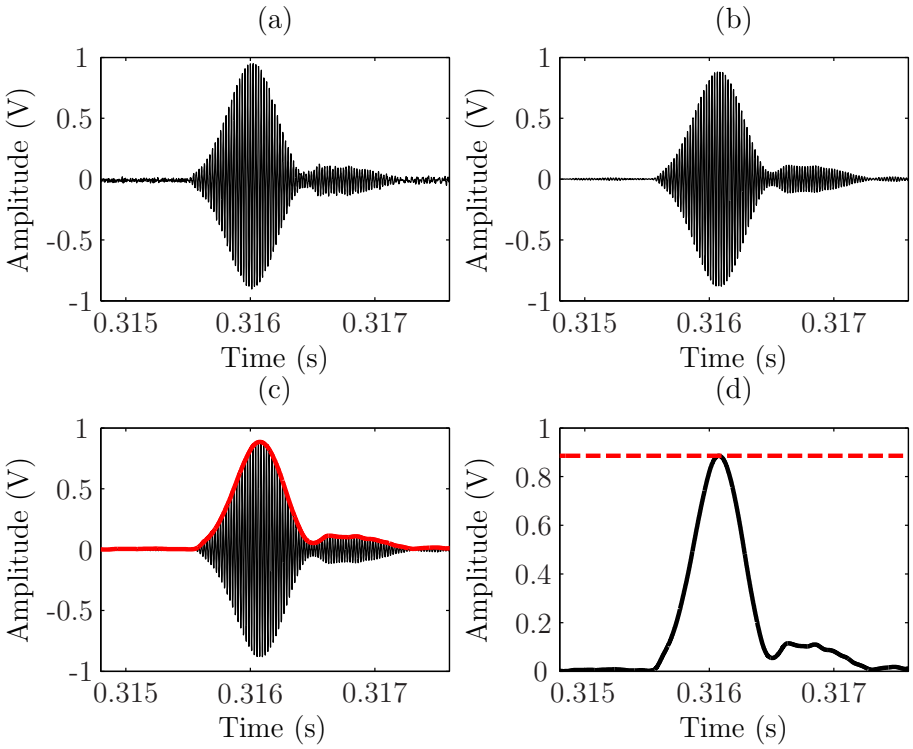

Figure 5.3: Part of the processing procedure where amplitude corresponds to that received from the hydrophone pre-amplifiers and recorded on the computer. (a) The noisy unfiltered pulse. (b) The filtered pulse. (c) The envelope of the pulse, calculated using a Hilbert transform. (d) The maximum value of the pulse marked by the algorithm as the dashed line.

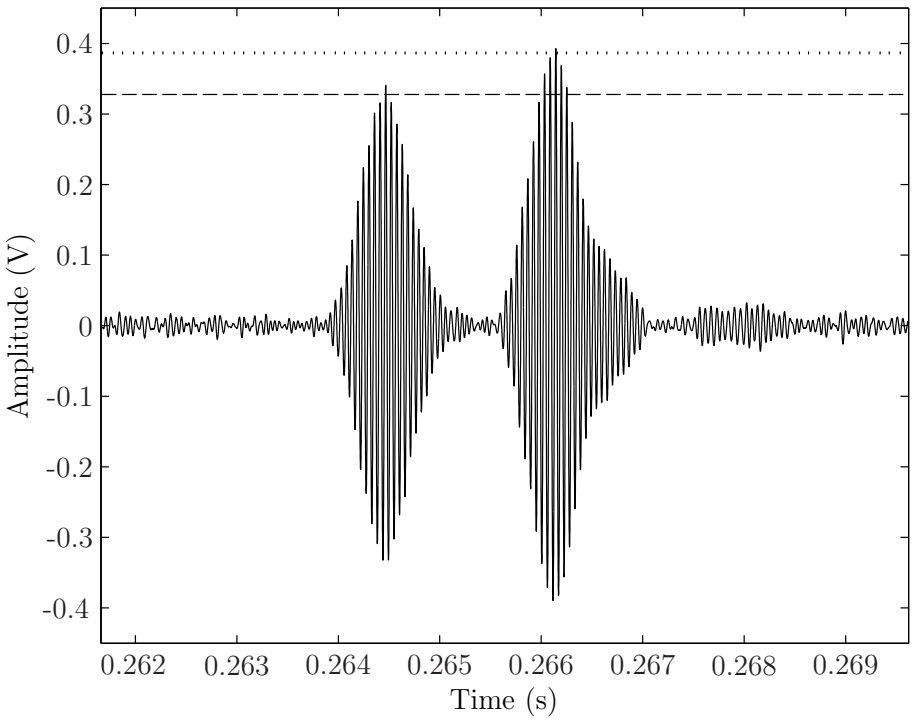

Figure 5.4: A direct and reflected 18 kHz pulse. The two horizontal lines mark the peaks that have been automatically detected by the processing algorithm. The dashed line marks the peak correctly chosen as the direct pulse and the dotted line marks the peak chosen as the reflected pulse.

program could then work out whether the highest peak was from the direct or reflected pulse and ensure the direct pulse was used.

There were also some occurrences of attenuation so high that the pulse could not be measured above the electronic noise level. In these instances, the program assigned a default value similar to the noise level.

5.1.2 Voltage amplitudes to pressure levels and attenuation

Pascal values for each of the pulses were then calculated using the calibration sheets for each of the hydrophones. The sensitivity of each hydrophone at a

given frequency is defined as

$$\mathrm{SENS} = 20\log_{10}\left[\frac{x_{\mathrm{V}}\frac{\mu V}{Pa}}{1\frac{V}{\mu Pa}}\right] \tag{5.1}$$

where x_{V} is the voltage per unit pressure. This can be rearranged to give

$$x_{\mathrm{V}} = 10^{\frac{-\mathrm{SENS}}{20}} \times 10^{6}. \tag{5.2}$$

This could then be used to convert the amplitude of each pulse, given in volts, to a pressure, given in pascals. It was then necessary to calculate the excess attenuation induced by bubbles and this was done using

$$A_{\mathrm{excess}} = 20\log_{10}\frac{P_{\mathrm{meas}}}{P_{\mathrm{base}}}. \tag{5.3}$$

The attenuation in dB per metre can then be calculated using

$$A = \frac{A_{\mathrm{i}} - A_{\mathrm{i+1}}}{\mathrm{distance}}, \tag{5.4}$$

where A_{i} is the attenuation measured in the i^{th} position. The baseline measurement is the measurement taken at sea with no bubbles present. It is necessary since the inversion uses the additional attenuation caused by the presence of bubbles. The most reliable baseline (termed here the "D2" baseline) is extracted from the sea trial data from the second deployment, in the following manner. The sound pressure levels at each frequency and for each hydrophone were plotted against time (see figure 5.5) for the duration of the deployment. Figure 5.5 shows how a clear baseline value emerges from the data when plotted in this way. It is also easy to identify which points are outliers - they appear on the plot above the average sound pressure level. These outliers are caused by errors in the automatic processing program and are likely to be instances when the program cannot work out whether the largest pulse is the direct or reflected pulse. The figure also shows areas of bubble activity where the presence of bubbles has attenuated the pulse and

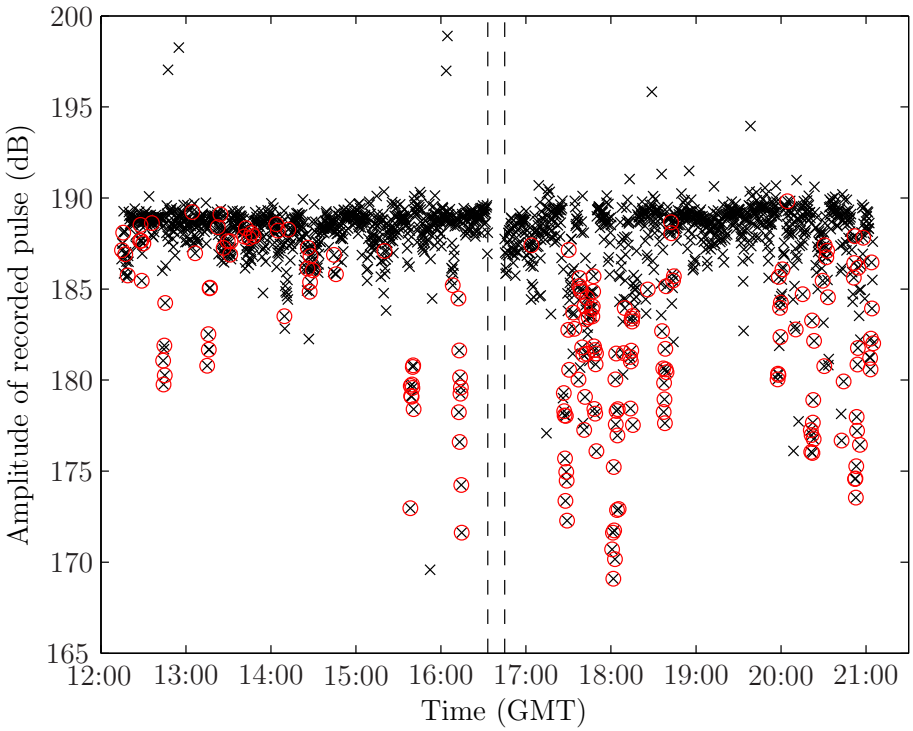

Figure 5.5: The sound pressure levels of the recorded 66 kHz pulses throughout the second deployment of D320. When bubbles are present, the amplitudes of the pulses drop, sometimes by up to 20 dB. The red circles highlight the 198 attenuation events discussed in section 5.1.5. The gap in the data set is where the inverted echo sounder system was running.

Hydrophone Position	Hydrophone serial number for deployment 1	Hydrophone serial number for deployment 2
1	18878	Not used
2	18879	18878
3	18880	18879
4	18881	18880

Table 5.1: A table showing which hydrophone occupied each measurement position.

therefore the measured sound pressure level is reduced. Finding a baseline measurement this way has significant advantages over direct measurement and use of hydrophone calibrations (as described below), in that it removes any calibration errors (though introduces its own uncertainties, expanded upon in section 5.1.3). It also removes any inaccuracies introduced by a change in conditions between the baseline measurement and the data measurement such as water temperature, salinity and turbulence. To provide ancillary baselines for comparisons with the "D2" method described above, several direct measurements in bubble-free conditions were undertaken (see figure 5.6).

Although bubble-free data were taken during the first deployment, and would have provided a suitable comparison with the "D2" baseline discussed above, owing to the requirement that the spar buoy hosts a range of sensors from several investigations, the positioning of the hydrophones was not consistent between the first and the second deployments. Table 5.1 clarifies the variation in the positioning of the hydrophones. This change in hydrophone position meant that calibration errors would be introduced if a baseline was taken from deployment 1 and used for data from deployment 2. The calibrations supplied with the hydrophones had a precision of ± 1 decibel. This introduces the potential of a 2 dB error between hydrophones and makes calculating an accurate baseline measurement very difficult since many of the attenuation values were of a similar magnitude to the 2 dB error.

The hydrophone positions were not changed for the third and fourth de-

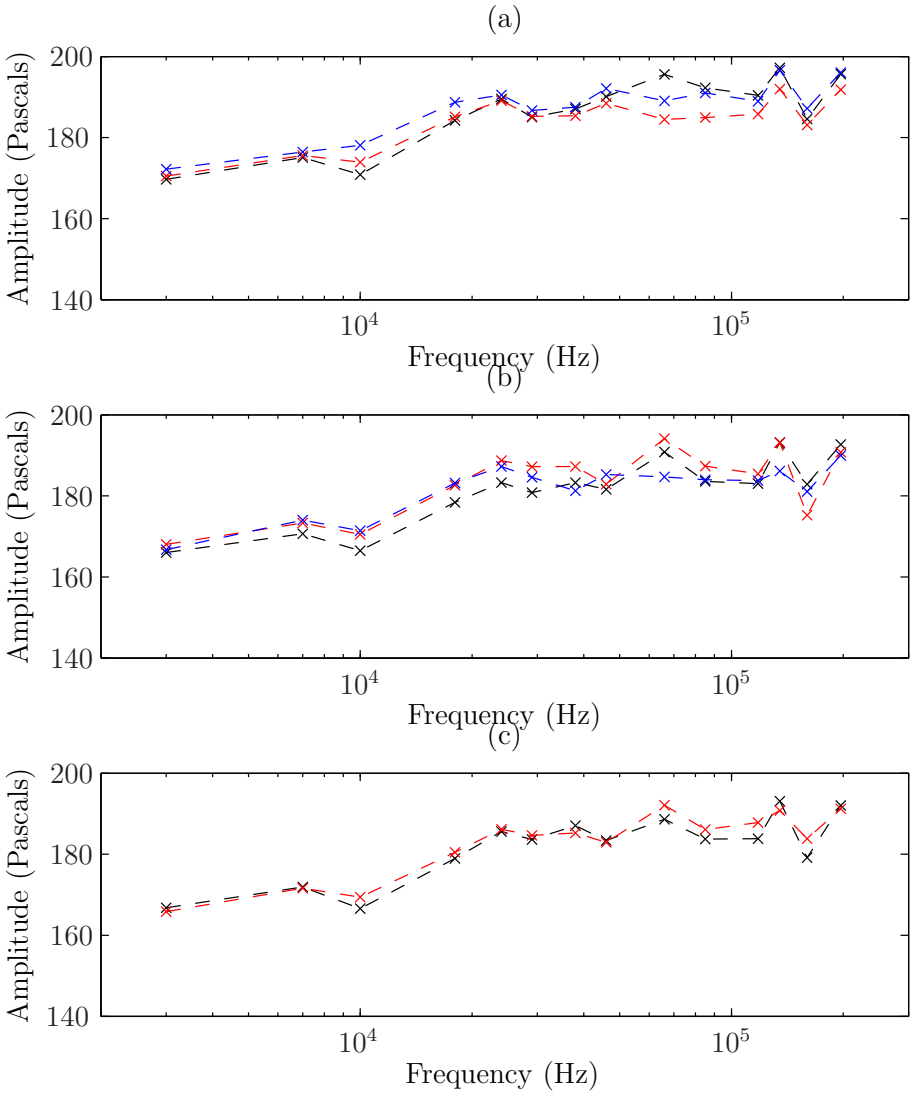

Figure 5.6: A comparison of the three baseline measurements. The black dashed line shows the "D2" baseline, the red dashed line shows the deployment 1 baseline and the blue dashed line shows the dock baseline. Panels (a), (b) and (c) show data for hydrophones at 2.54 m, 1.22 m and 0.80 m depths respectively. Panel (c) is missing data from the dock measurement owing to damage to the hydrophone sustained during the fourth recovery on D320.

Figure 5.7: The buoy in the docks at the National Oceanography Centre, Southampton, as part of a calibration test.

ployments but equipment failure prevented a baseline measurement being taken using those datasets. As an ancillary measurement to the calibrations, a dock test was carried out at the National Oceanography Centre upon return to Southampton. The validity of this measurement was uncertain, since the buoy had been dismantled for transit from the ship back to Southampton. However, in the interests of determining for future researchers to what extent such a disturbance invalidates (or otherwise) the baseline, the buoy was reconstructed using the geometrical and dimensional measurements of equipment on the buoy that had been taken on the ship to try and rebuild it as it was on the ship. As was shown in the previous chapter, one of the hydrophones had been destroyed so only two of the three hydrophones used on the second deployment could be used in the dock test. The comparison shown in figure 5.6 shows the efficacy of finding the baseline using the "D2"

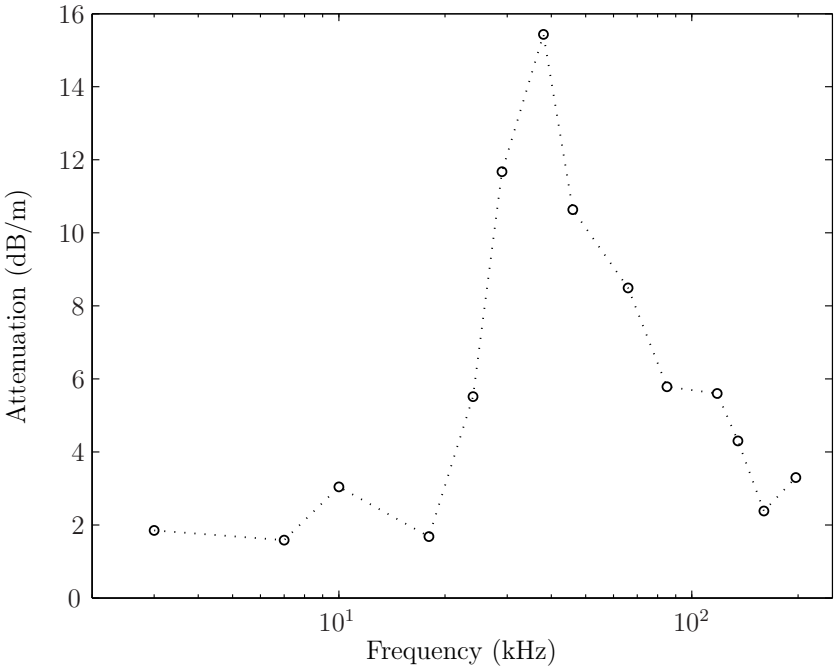

Figure 5.8: Attenuation against frequency measured at 20:24 on 29$^{\text{th}}$ June 2007 during the second deployment of D320. The measurement represents a spatial average of the attenuation between hydrophones at depths of 0.8 and 1.22 m (though these hydrophones were approximately 15 cm deeper for the second deployment of D320, as mentioned in section 4.5.2).

method, and it was this baseline which was extracted from the data to use for the processing of the dataset.

Once an appropriate baseline measurement was established, it was possible to calculate attenuations using equations (5.3) and (5.4). Figure 5.8 shows a typical attenuation measured during the deployment. With three hydrophones, attenuation could be measured between three points, i.e., at two discrete depths along paths a to b, and b to c, where a, b and c are the hydrophone positions. Therefore nominal attenuation can be path averaged for the midpoints of the two paths. The deepest depth was between the first and second hydrophones and the mid-point between these was on average 2 metres deep. The shallowest mid-point depth was on average 1.15 metres deep and was midway between the second and third hydrophones.

5.1.3 Uncertainty in "D2" baseline technique

Although the "D2" baseline method offers many advantages over the alternatives (discussed in section 5.1.2), it introduces uncertainties specific to the technique. Figure 5.5 shows a typical plot from which the baseline pressure level for one frequency at one hydrophone position was extracted. The baseline value is taken from the thick band of the data points that runs from left to right. Uncertainty arises from the thickness of this band and the exact point at which the baseline value is taken. The method used, therefore, was to measure the thickness of the band and take the midpoint as the baseline value. A maximum and minimum value could then also be extracted from the thickness of the band. The method for calculating attenuation from pressure levels is given in equations (5.3) and (5.4). Rearranging these equations gives the uncertainty around an attenuation value between two hydrophones as

$$A_{\text{uncert}} = \frac{20}{\text{distance}} \left[\log_{10} \left(P_{\text{m-rat}} \frac{P_{\text{alt\_base,i+1}}}{P_{\text{alt\_base,i}}} \right) \right], \tag{5.5}$$

where $P_{\text{alt\_base,i}}$ and $P_{\text{alt\_base,i+1}}$ are the alternative baselines (taken from the maximum and minimum of the thickness of the bands) and $P_{\text{m-rat}}$ is the ratio of measured pressures, given by

$$\begin{aligned} P_{\text{m-rat}} &= P_{\text{meas,i}} \times P_{\text{meas,i+1}} \\ &= (P_{\text{base}_\text{i}} \times P_{\text{base,i+1}}) \times 10^{\frac{A \times \text{distance}}{20}}. \end{aligned} \tag{5.6}$$

This uncertainty can be applied to the whole dataset and the results are shown in section 5.1.5.

5.1.4 Attenuation data to bubble size distributions

Once the voltage levels received from the hydrophones have been converted to attenuations, the attenuation data can be inverted to produce bubble size distributions using the theory described in chapter 3. This is not, however, a trivial process, as the matrix used in the inversion typically has large off-

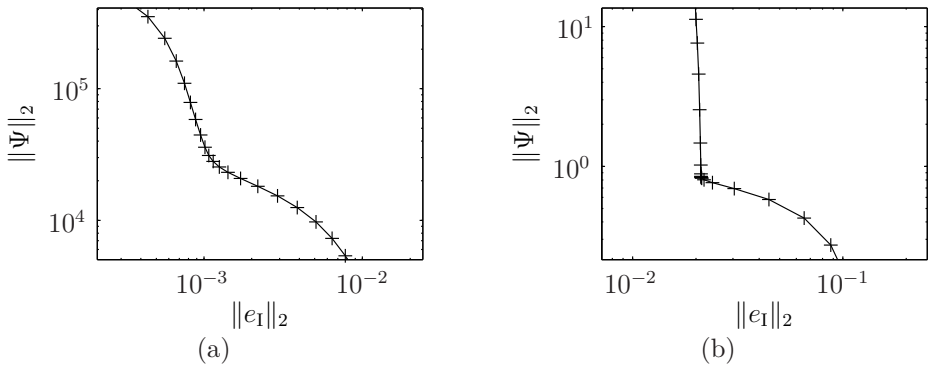

Figure 5.9: Two examples of an L-curve using data from the second deployment of D320.

diagonal values resulting in instabilities that require an optimisation process. The code that was first used to perform the inversion was written by Dr Gary Robb, who at the time held a post-doctoral position under the supervision of Professor Timothy Leighton and Professor Paul White at the University of Southampton. The code is based on existing theory [16, 19, 23] and uses a regularisation technique based on the L-curve (figure 5.1.4) described in Leighton *et al.* [8]. With this technique, the user has to select the optimum value from the corner of the "L". A number of drawbacks are inherent with this method. Firstly, each inversion required user input to select the optimum beta value. Secondly, there was sometimes more than one "L" with no real indication as to which would produce the best result. Through experimentation with artificial data, it was found that sometimes an accurate solution could be found, and yet sometimes the result produced was inaccurate. In the light of these drawbacks, an automated inversion with some feedback concerning the accuracy of the result would be superior and greatly reduce processing time.

Modifications to the code were carried out by the author with the help of Professor Paul White and Professor Timothy Leighton of the University of Southampton. For each inversion, a large range of beta values are swept through. For each beta value, a bubble size distribution is calculated. This distribution is then re-inverted and compared to the original attenuation

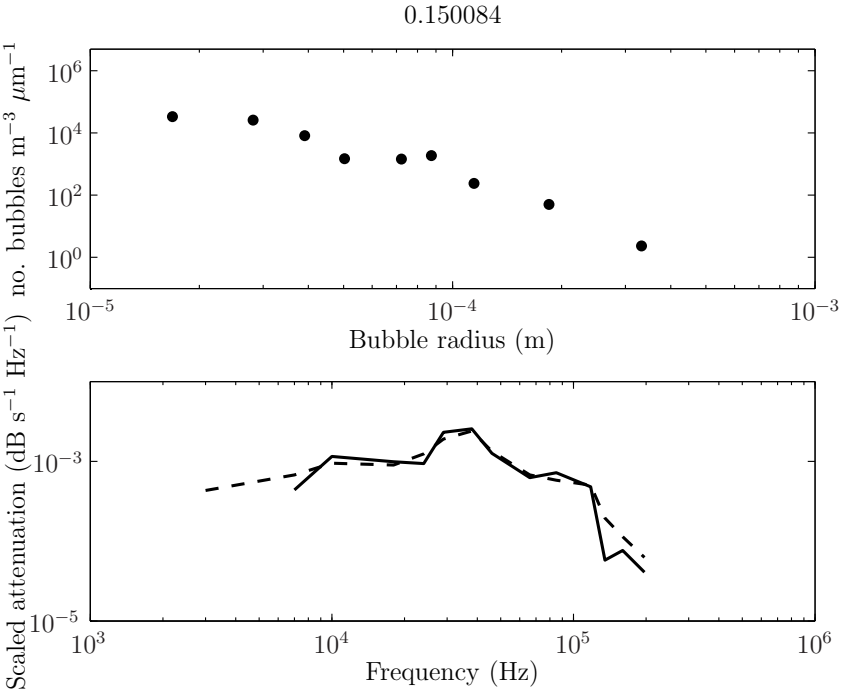

Figure 5.10: The still frame taken from the graphical animation of the inversion. The current beta value is shown at the very top, the bubble size distribution is shown on the top plot and the comparison of the original (bold line) and re-inverted (dashed line) attenuation is shown on the bottom plot.

data. This was initially a graphical function (see figure 5.10), with an animation of the changing bubble size distribution and the comparison between the original and re-inverted attenuation as the beta values are being swept through being displayed on a computer screen. It should be noted that the attenuation data referred to here are scaled with frequency as in equation (3.37) in chapter 3. The resulting quantity, v, is given by

$$v = \frac{c_{\mathrm{w}} A}{20 \log_{10}(\mathrm{e})\, \omega}, \tag{5.7}$$

This graphical function was an immediate improvement since it provided feedback on the accuracy of the inversion. The process could be automated

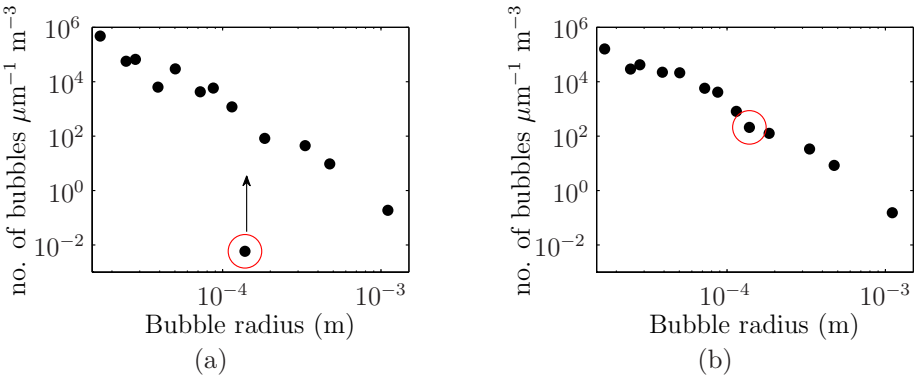

Figure 5.11: The bubble population as the range of beta values are swept through. Panel (a) shows a new point (circled) which is sliding up to the position shown in panel (b).

by recording the difference between original and re-inverted attenuation for each beta value and then finding the beta value that produces the minimum difference. Although this appeared to be a good technique, it was not always accurate for the following reason. The instabilities in the inversion mentioned earlier cause some of the values in the bubble size distribution to be negative. As the regularisation value is increased, each negative value is "reined in" and eventually becomes positive. As each previously negative point becomes positive, it increases as the beta value is further increased until it reaches its final value in the bubble size distribution (see figure 5.11). This means that if the beta value is not increased enough, the resulting bubble size distribution will have a sharp dip that should not be there. However, if the beta value is increased too much, the error between the original and the re-inverted attenuation becomes too great. Therefore it is important to apply the appropriate amount of regularisation.

A subtle modification was also made to the way in which the regularisation is applied. The standard method of applying the regularisation is given in equation (3.59). This adds a regularisation value to the diagonal elements of the ill-conditioned $\mathbf{K}$ matrix (see section 3.2). This results in the small diagonal elements being affected proportionately far more than the large diagonal elements. An alternative solution is to inflate the diagonal elements

by a proportional amount, which is achieved by applying the regularisation parameter using

$$\Psi_{\text{opt}} = [(\mathbf{K}^T\mathbf{K})(1 + \beta\mathbf{I}_0)]^{-1}(\mathbf{K}^T\boldsymbol{\alpha}). \tag{5.8}$$

Through experimentation with both methods, it was found that the new method allowed stable and accurate solutions to be found more easily than through use of the old method.

Automating the selection of the beta value is not a trivial process. It was very difficult to write code that could automatically select the optimum beta value. The most reliable method was to select a beta value manually from the graphical function. Whilst this was time consuming, the resulting bubble size distributions were as accurate as possible.

5.1.5 Processing the entire dataset

With a technique for inverting attenuation data to produce bubble size distributions now in place, the entire dataset could be processed. As the attenuation data were studied in more detail, it was found that many of the files did not show significant attenuation. Therefore, each file was passed through an algorithm that examined the sum and the mean of the frequency dependent attenuation and selected only those files that showed attenuation across a range of frequencies. Of the 1800 measurements made, only 198 showed significant attenuation and it is these measurements that are inverted to bubble size distributions. The lengthy procedure of processing these data produced some excellent results, shown in figure 5.12.

Figure 5.14 shows the means of the measurements at each depth compared to historical measurements. The figure shows very good agreement between the measured bubble size distributions and the historical data from the open ocean. There is a clear increase in the number of bubbles between the two depths. The range of bubble radii measured as part of this PhD is the broadest range ever to be measured in this way (active acoustics) in the open ocean [9, 20, 29, 30, 33, 34, 96–102] which is an achievement in itself.

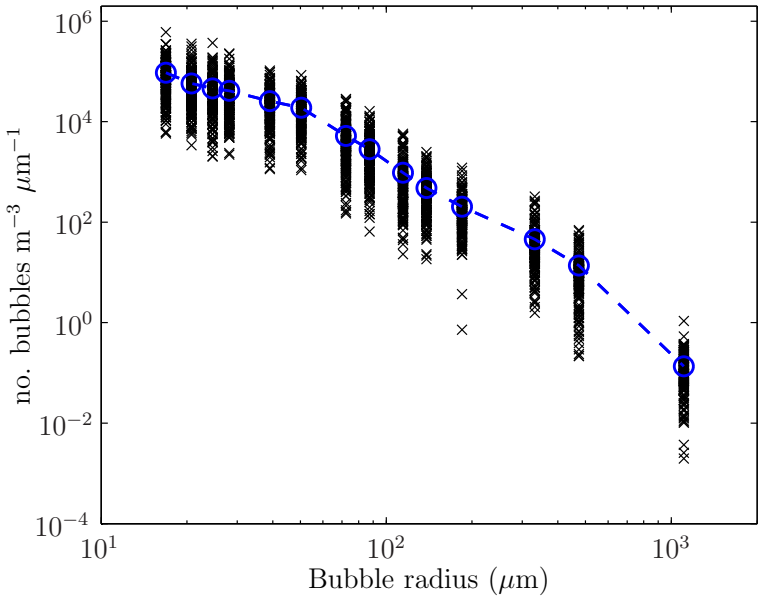

(a)

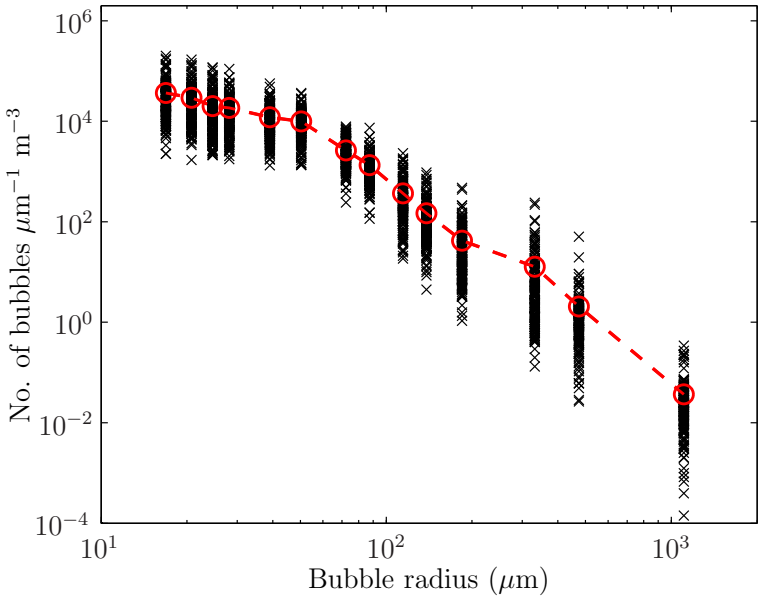

(b)

Figure 5.12: Bubble size distributions for the second deployment of D320 at depths of (a) 1.15 m, and (b) 2 m. The blue and red lines show the mean bubble size distribution at each depth.

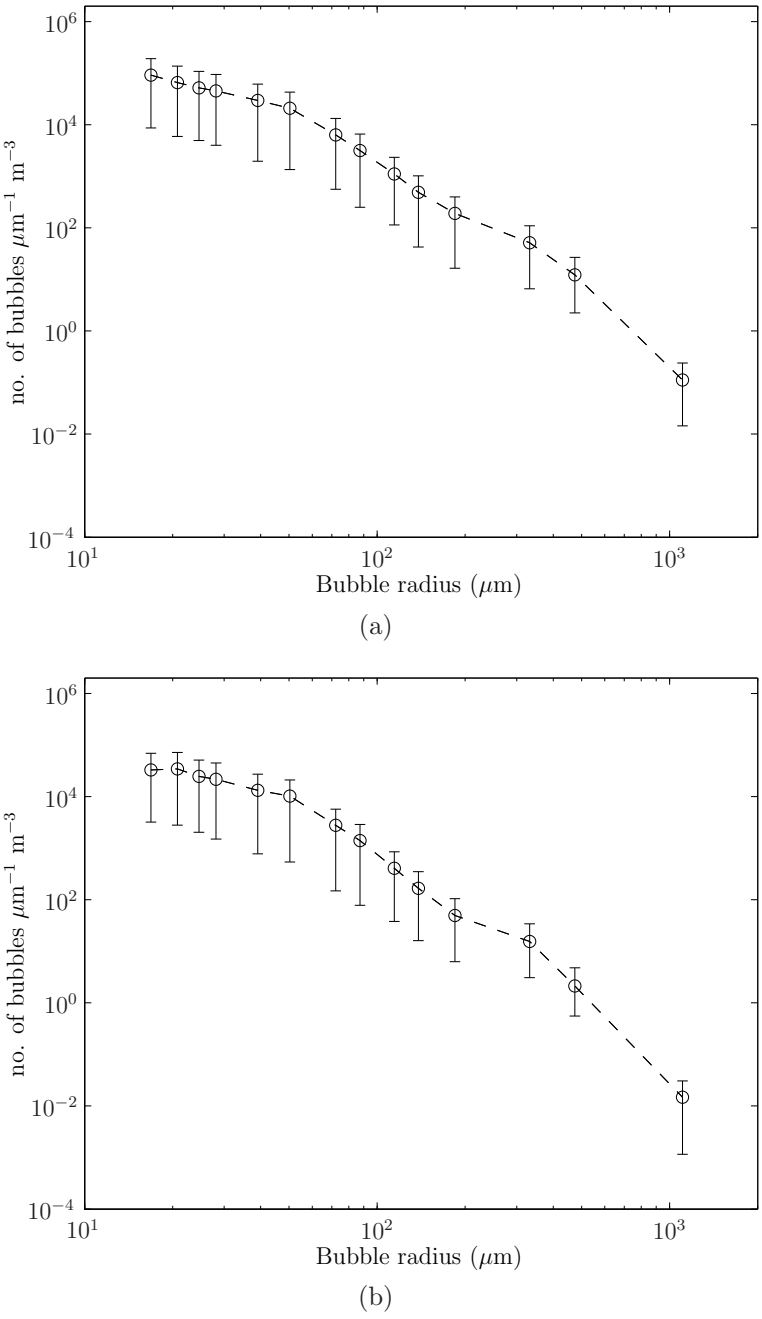

Figure 5.13: Standard errors for the mean bubble size distributions at (a) 1.15 m and (b) 2 m.

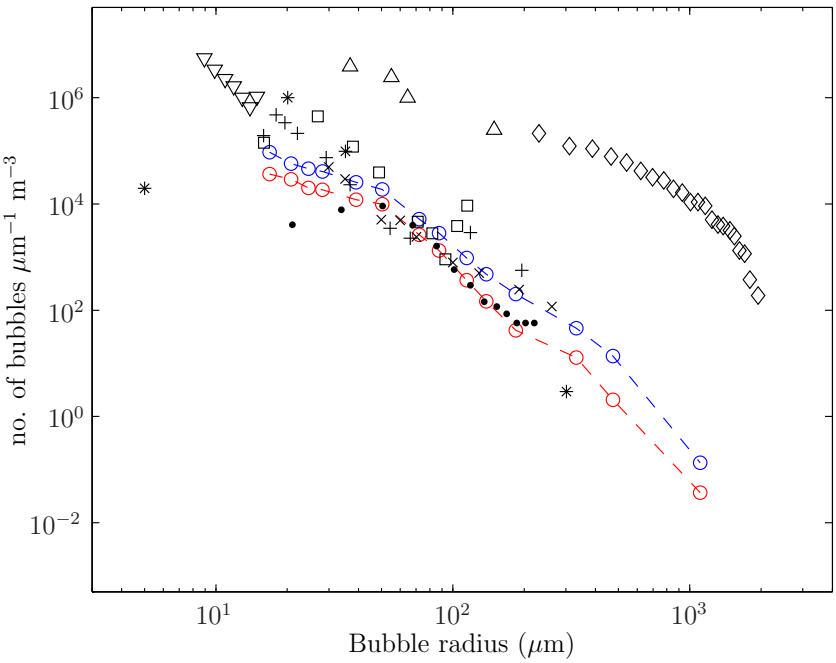

Figure 5.14: The bubble size distributions measured on the sea trial compared with historical measurements. The historical data include the open ocean data of Breitz and Medwin [9] (crosses), Phelps and Leighton [30] (plus signs), Farmer and Vagle [29] (stars) and Johnson and Cooke [10] (dots), and the surf zone data of Deane and Stokes [26] (diamonds), Phelps *et al.* [27] (triangles), Meers *et al.* [28] (downward pointing triangles) and Leighton *et al.* [8] (squares).

Uncertainty arising from the baseline measurements (see section 5.1.3) can be applied to the means of the bubble size distributions shown in figure 5.12. The means are transformed into attenuation using the techniques discussed in chapter 3. Once mean attenuations have been calculated for both measurement depths, equations (5.5) and (5.6) can be used to calculate the minimum and maximum attenuation. The results of this are shown in figure 5.15. The minimum and maximum attenuations can then be inverted to yield minimum and maximum bubble size distributions, shown in figure 5.16. As can be seen from the figures, the impact of the uncertainty is greater at 1.15 metres than at 2 metres depth.

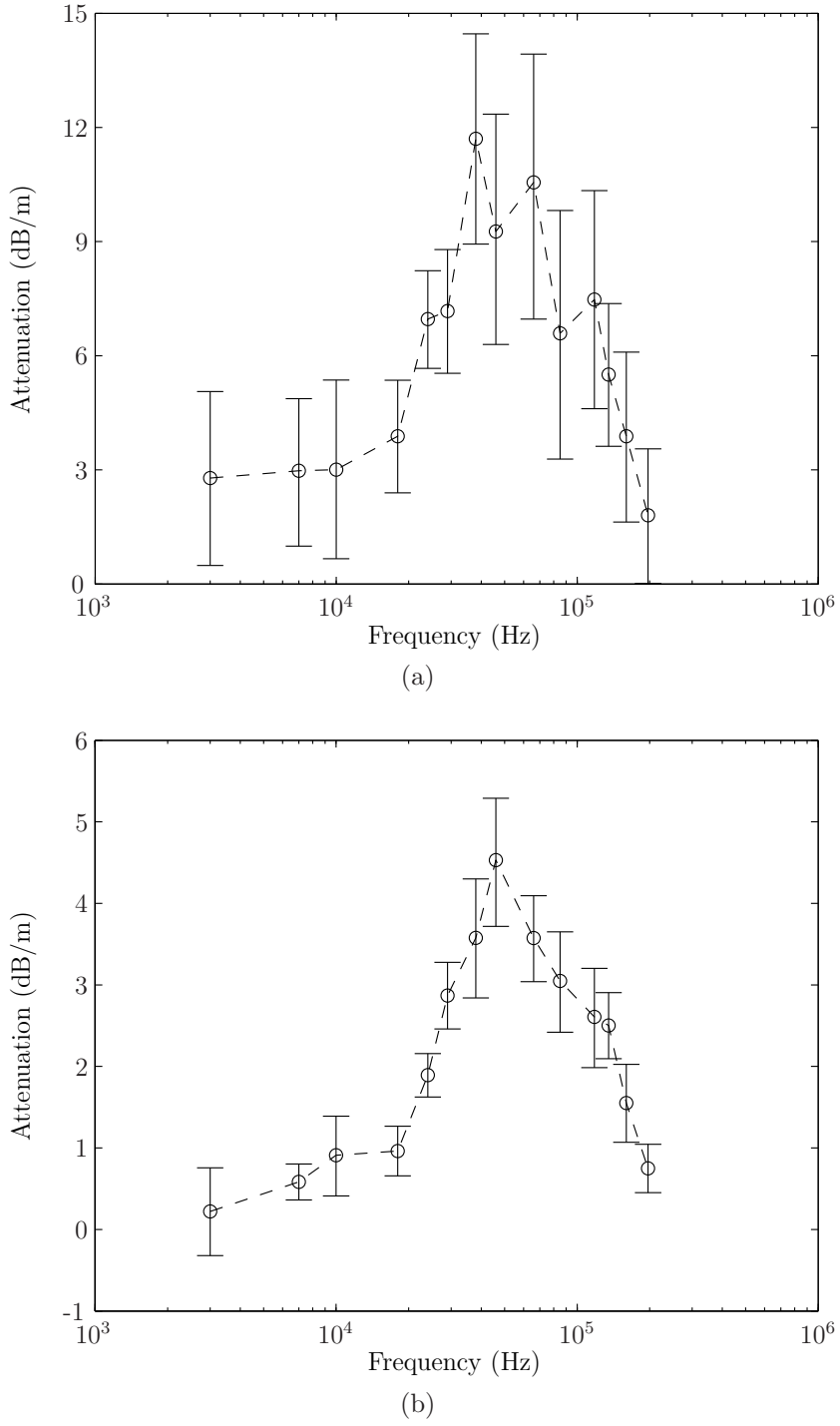

Figure 5.15: Mean attenuation at (a) 1.15 metres and (b) 2 metres depth. The uncertainty bars show the uncertainty arising from the baseline measurement, as described in section 5.1.3.

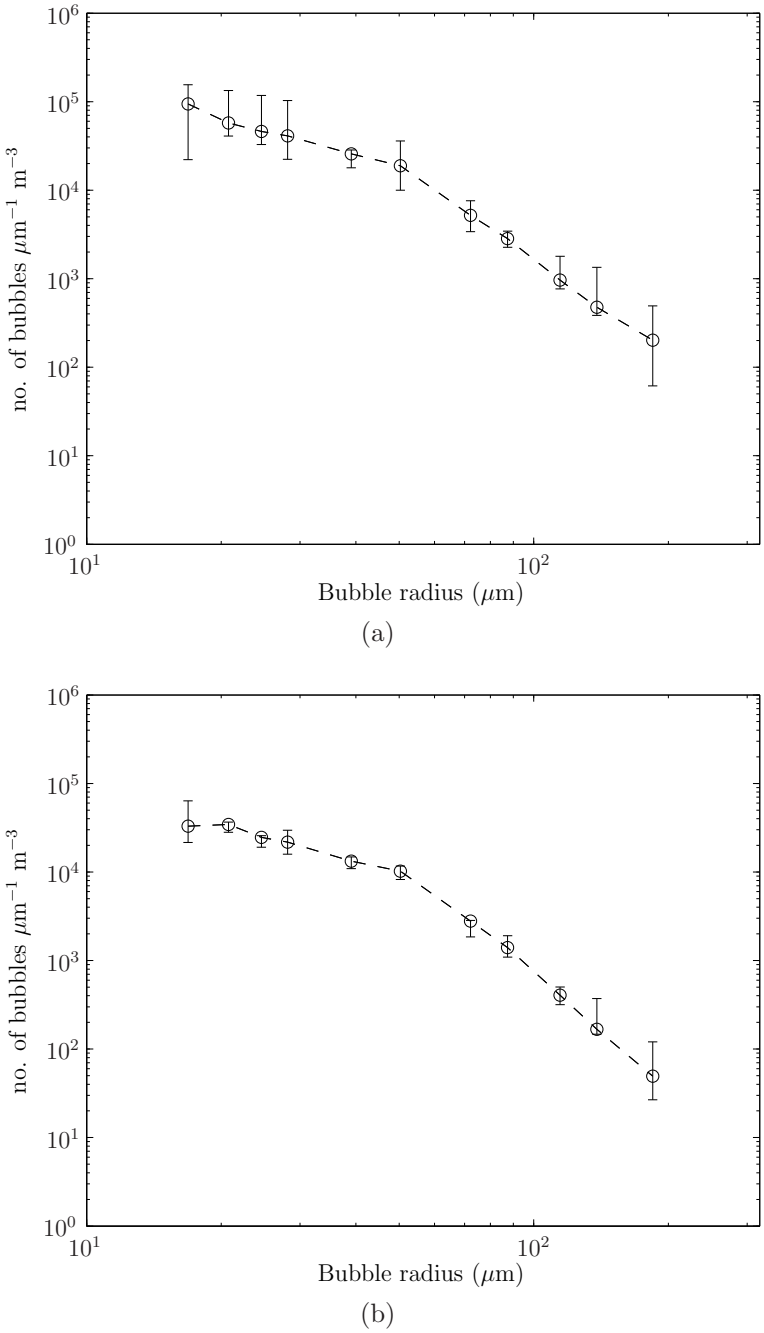

Figure 5.16: Mean bubble size distributions at (a) 1.15 metres and (b) 2 metres depth. The uncertainty bars show the uncertainty arising from the baseline measurement, as described in section 5.1.3. Only radii in the range 16-187 μm are shown as these are the most important radii for comparison with results in chapter 6.

Authors	Year	Bubble size range (μm)	Wind speed (ms^{-1})	Measurement depth (m)	Water depth (m)	Technique
Johnson and Cooke [10]	1979	17 - 300	11-13	0.7	20-30	Photographic
Breitz and Medwin [9]	1989	30 - 270	12-15	0.25	120	Acoustic resonator
Farmer and Vagle [29]	1989	17 - 119	12-14	14/24	140/4000	Acoustic bubble scatter
Phelps *et al.* [27]	1997	38 - 119	11	1.5	3	Combination frequency
Phelps and Leighton [30]	1998	16 - 192	10-12	0.5	17-22	Combination frequency
Deane and Stokes [26]	1999	250 - 2000	-	0.05	0.3	Photographic
Meers *et al.* [28]	2001	9 - 15	6.5	1	1.5	Acoustic attenuation
Leighton *et al.* [8]	2004	16 - 115	4	~ 1	2	Acoustic attenuation

Table 5.2: Historical bubble size distribution measurements.

5.2 Supporting data

For a thorough comparison of the measured data with the historical data, meteorological and other supporting data must be considered. The top section of the spar buoy has wave wires capable of measuring wave height and period. However, because of unexplainable equipment failure, no data was measured by these wires. Therefore it is necessary to look to other sources for meteorological measurements, namely the closely located ASIS-2 buoy and instruments on the ship. The *RRS Discovery* has a ship borne wave recorder (SBWR) onboard as well as numerous sensors and equipment for measuring meteorological conditions. The most notable is AutoFlux [103], which measures air-sea fluxes as well as logging data from many sensors mounted on the ship.

It is important to assess whether data measured on the ship will be similar to that which would have been measured by the buoy. Figure 5.17 shows the positions of the buoy, the ship and the ASIS-2 buoy on the day of measurement during the second deployment. During the period in which data was taken, the ship was on the southern half of its track. At the start of this period, the ship was approximately 48 km away from the buoy and by the end of the period the ship was approximately 15 km from the buoy. It is therefore a reasonable approximation to assume that the meteorological conditions at the position of the buoy were similar to those measured at the ship's location. This approximation is further substantiated by comparing the wind speeds (shown in figure 5.19) measured by the ship sensors and by the ASIS-2 buoy, which was on average less than 9 km from the spar buoy.

The wave period, T_{z}, measured by the SBWR is shown in figure 5.18. Owing to the nature of the SBWR, the measurements it makes can be inaccurate when the ship is steaming. Therefore the ship's speed has been plotted alongside the wave data to highlight periods of uncertainty. The mean wave period is 6 seconds. The significant wave height, H_{s}, which is the average wave height of the one-third largest waves, was measured by the ASIS-2 buoy and the data was kindly supplied by Professor William Drennan of the

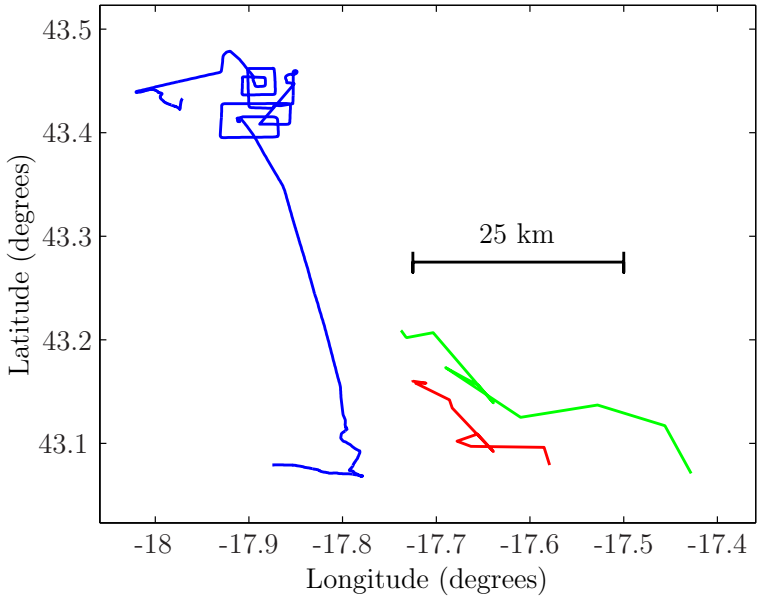

Figure 5.17: The positions of the buoy (red line), the ship (blue line) and the ASIS-2 buoy (green line) on 29th June 2007 during the second deployment of D320.

Rosenstiel School of Marine and Atmospheric Science, University of Miami. Figure 5.21 shows the significant wave height increasing steadily throughout the deployment. The wind speed is reasonably constant throughout the measurement period (1200 hrs to 2300 hrs) with a mean value of 14 m/s which is similar to many of the historical experiments. The significant wave height is shown in figure 5.21 and can be seen steadily rising throughout the measurement period from just under 2 metres to approximately 4 metres.

The air temperature (recorded on the ship by AutoFlux) for the 29th June is shown in figure 5.20. The temperature rises to approximately 18.3 °C during daylight hours and falls to approximately 17.5 °C during the night. The water temperature remains reasonably constant throughout the 24 hour period with a mean value of 17 °C.

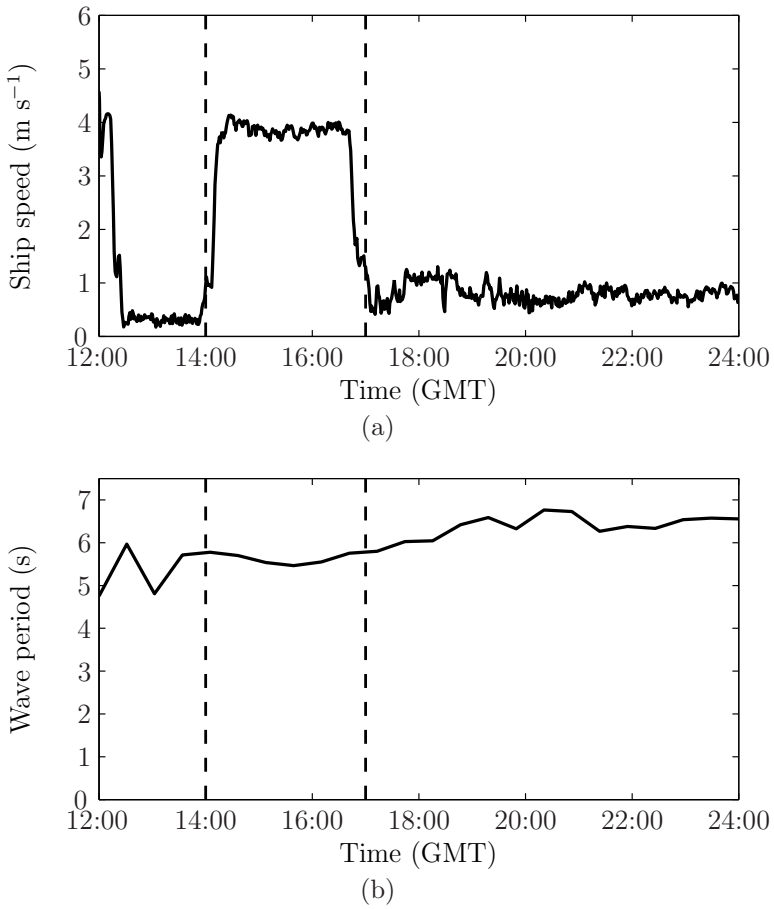

Figure 5.18: Wave data measured by the ship borne wave recorder on 29$^{\text{th}}$ June 2007. The ship speed is shown in (a) and the wave period, T_{z}, in (b). The dashed vertical lines on each graph show the start and end times of the period in which the ship is steaming, causing possible inaccuracies in the measured data.

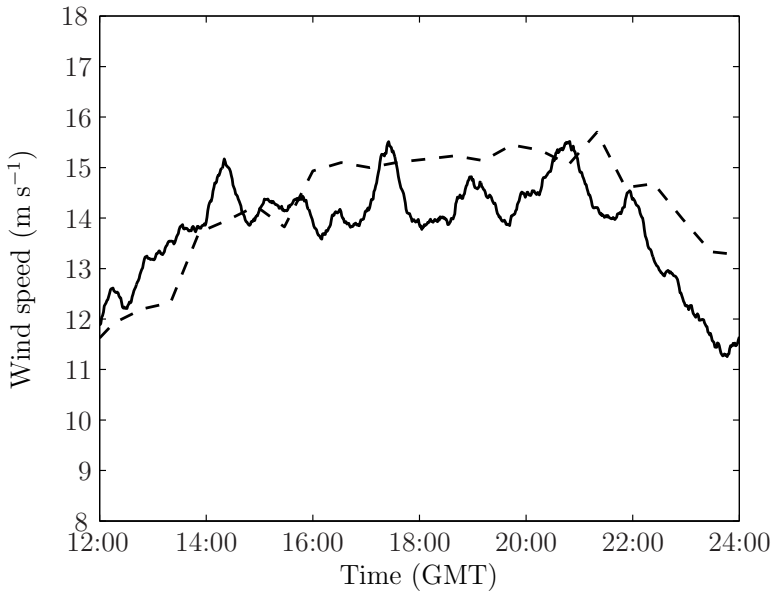

Figure 5.19: Wind speeds on the 29$^{\text{th}}$ June 2007 as measured by AutoFlux on the ship (the solid line) and the ASIS-2 buoy, located near the spar buoy (dashed line). Both datasets have been corrected to a height of 10 m using techniques outlined in [104].

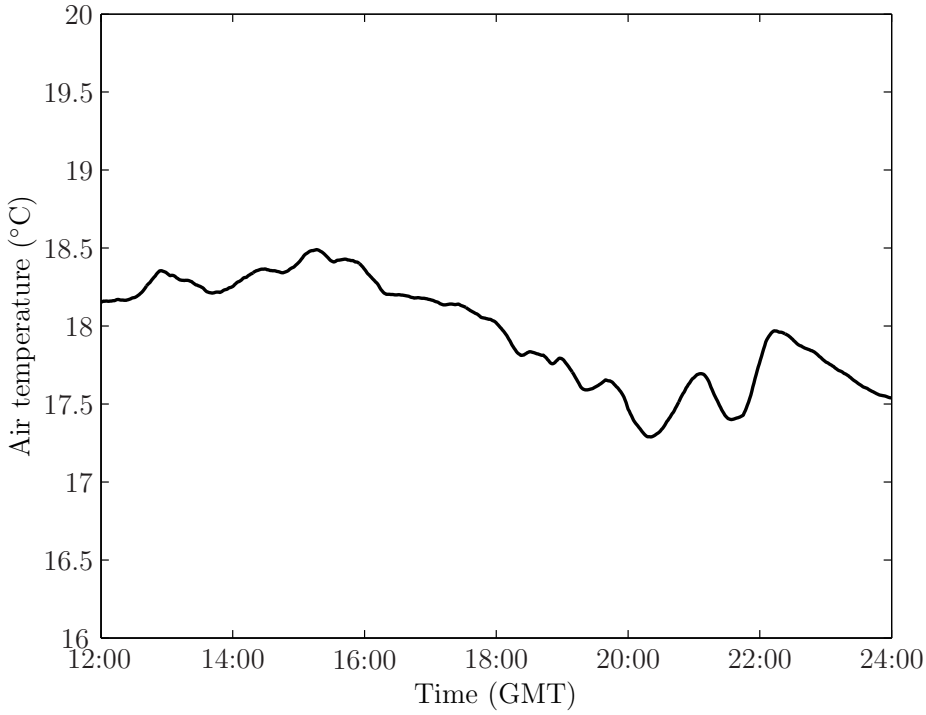

Figure 5.20: The air temperature for 29th June 2007 measured at the ship's location at a height of 17 m.

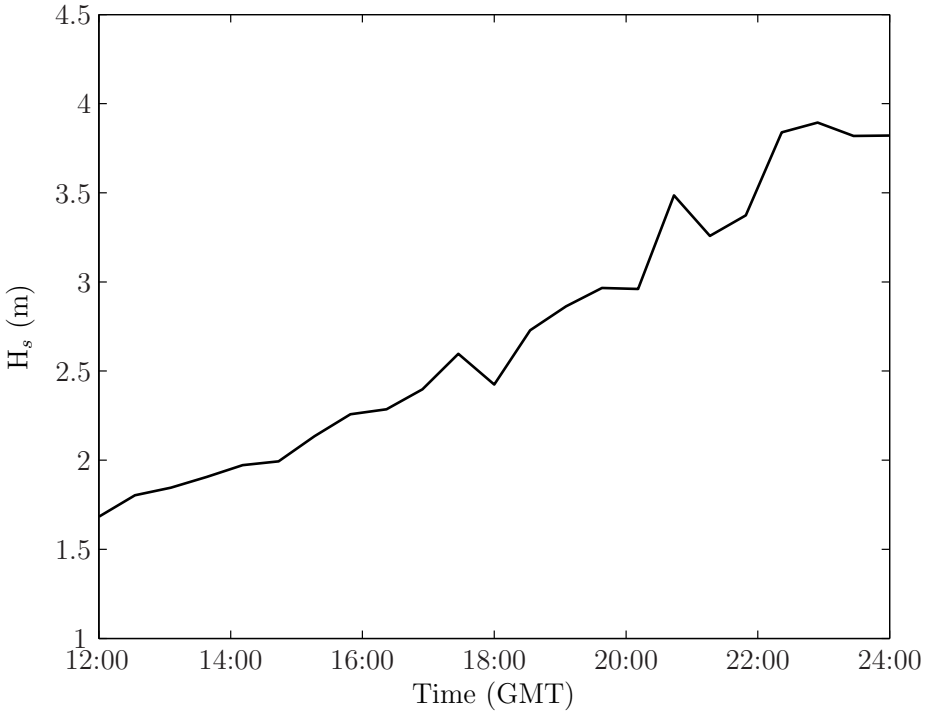

Figure 5.21: The significant wave height, H_{s}, throughout the second deployment. The measurements were taken by the closely located ASIS-2 buoy and the data is courtesy of Professor William Drennan of RSMAS, University of Miami.

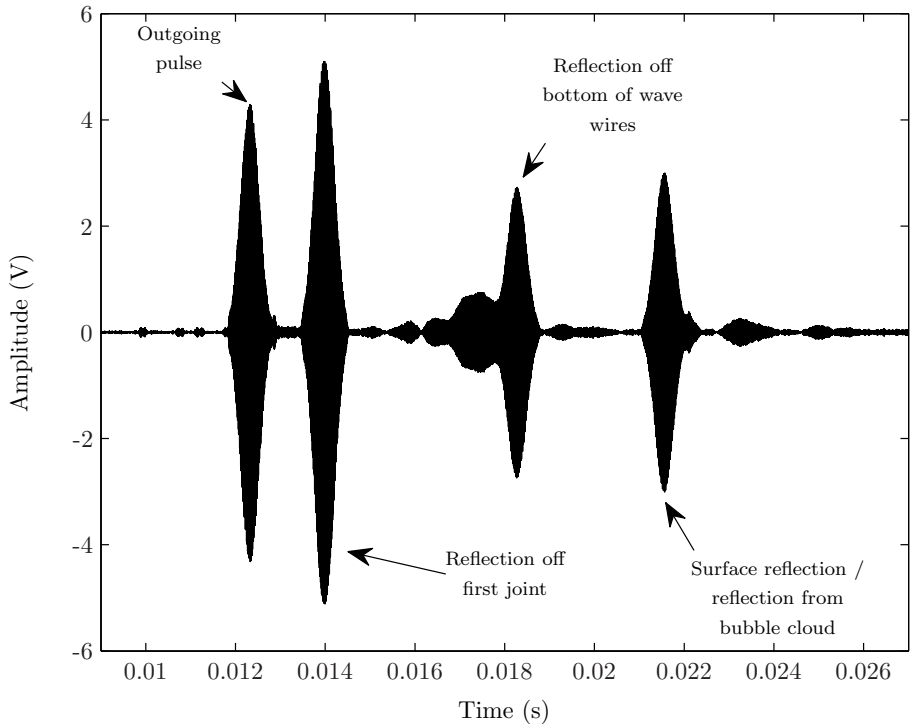

Figure 5.22: A typical signal measured by the hydrophone during the inverted echo sounder experiment. Significant reflections are labelled on the plot.

5.3 Inverted echo sounder data

The inverted echo sounder (IES) system employed a single hydrophone, located at the base of the buoy, measuring single 160 kHz pulses reflected from the sea surface and the bubble clouds. By measuring the strength of the backscatter due to bubbles, a profile of the bubble clouds can be obtained as the buoy passes through them.

The echo sounder emits one pulse every five seconds for five minutes, then saves the file and repeats this procedure for another five minutes. This is supposed to happen twice throughout the deployment. As with the attenuation data, the second deployment of the second sea trial was the only deployment to return useful data. Even so, a fault in the equipment meant that only one ten minute period of IES data was recorded instead of two.

Figure 5.22 shows the received signal and there are clearly a number of reflections between the source and the surface of the ocean. These were all caused by the physical structure of the buoy and could not be avoided because the buoy provided the platform for several measurement systems by a number of researchers, and was not primarily designed to host acoustical sensors. Ideally, there would be no structure between the hydrophone and the surface and indeed previous experiments [42] have achieved this. However, this was not possible on a buoy designed to be able to carry out so many different experiments, especially since acoustic experiments were not the primary objective of the buoy.

To overcome these prominent reflections, it was important to compare the measured signals with a baseline measurement to find the effect of the presence of bubbles. Section 5.1.2 described the method to obtain a baseline measurement for the attenuation data. A similar method was used for the IES data, and is described in more detail in section 5.3.1. As for the attenuation data, baseline measurements taken in the docks at the National Oceanography Centre were not compatible with the sea trial data for reasons described in section 5.1.2.

5.3.1 Processing the data

Unlike the acoustic attenuation system, which used frequencies between 3 and 197 kHz, the IES system used only a single frequency - 160 kHz. This is because the system looks at backscatter strength rather than attenuation at different frequencies. These single frequency measurements make filtering the signal very easy with a band-pass filter centred at 160 kHz. A Hilbert transform is taken in order to get the envelope of the signal as can be seen in figure 5.23. A cross correlation is then performed using the signal and the envelope of the original outgoing pulse. This smoothes the signal and gives a more accurate representation of where the reflected energy is in the signal.

As with the attenuation data, the slow speed of the onboard computer prevented the signals from being aligned. A peak detection algorithm was

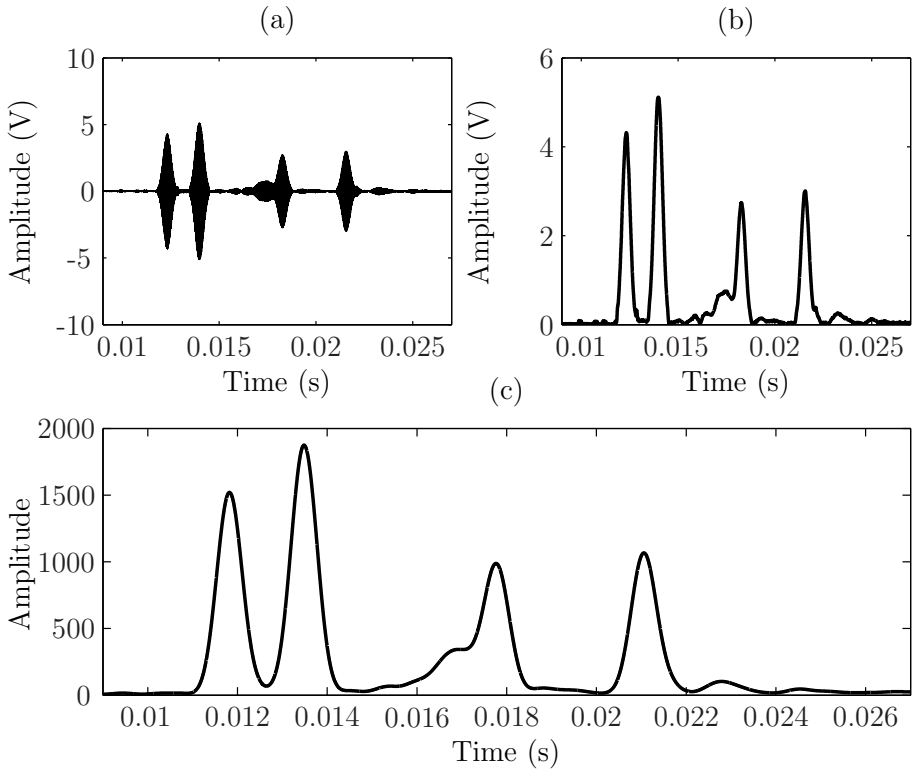

Figure 5.23: Panel (a) shows the filtered signal received from the hydrophone, panel (b) shows the resulting signal after the Hilbert transform and panel (c) shows the signal after the cross-correlation with the original pulse.

written to detect the first peak and this allowed the signals from all the files to be aligned.

The next step in the processing was to take all of the raw amplitude signals and turn them into volumetric backscatter strengths. The theory used for this step is detailed in chapter 3. The most important equation used is

$$S_{\mathrm{v}}(r) = 20\log\left[A_{\mathrm{IES}}(r)\right] + K_{\mathrm{cal}} + 40\log\left[r\right] + 2\cdot\alpha_{\mathrm{ab}}\cdot r - 10\log\left[U(r)\right], \quad (5.9)$$

where S_{v} is the volumetric backscatter strength with units of decibels *re*: 1 m^{-1}. The calibration coefficient, K_{cal}, is something that is missing from this dataset. Section 5.4 describes how the attenuation data can be used to calibrate the IES data. Until the value of the calibration coefficient, K_{cal}, is determined (see later), we will let $S_{\mathrm{v,K}}$ indicate the value of the volumetric backscatter strength calculated from the raw data with a fixed but unknown calibration factor, K_{cal}. There will be a constant fixed number of decibels which need to be added to values of $S_{\mathrm{v,K}}$ to give the absolute values S_{v} of the volumetric backscatter strength.

Once the volumetric backscatter strengths, $S_{\mathrm{v,K}}$, have been calculated for each pulse, the baseline is chosen by taking the minimum $S_{\mathrm{v,K}}$ at each range bin. The baseline can then be subtracted from each of the data files giving the extra volumetric backscatter strength resulting from bubbles. This information can then be plotted against time as shown in figure 5.24. As shown in figure 5.24(a), there is a great deal of noise introduced below what is shown as 5 metres. This is caused by interference from the structure of the buoy and cannot be avoided. Figure 5.24(b) shows the top few metres of the water column which is generally unpolluted acoustic data.

The next step is to work out where the surface is on these plots. This is done using the cross-correlated data. The surface can be found be measuring the position of the surface reflection.

The positions of the hydrophones can also be marked on the plot as can be seen in figure 5.25. The positions of the hydrophones become significant

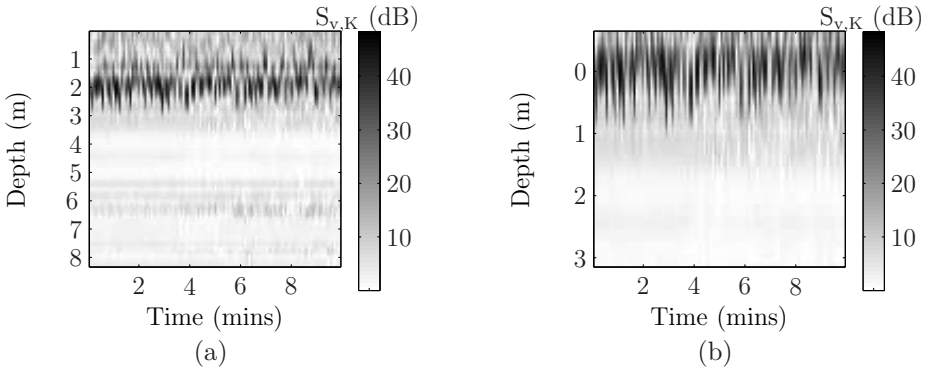

Figure 5.24: The uncalibrated volumetric backscatter strength, $S_{\mathrm{v,K}}$, for all depths (a) and for the top few metres (b). Depths are relative to the mean surface level. Although a portion above the sea surface is shown in (b), this is merely the signal recorded after the surface reflection and this is later removed (see figure 5.26).

when calibrating the IES data with the acoustic attenuation data. This is expanded upon in the next section.

With the position of the surface known, it becomes easy to plot $S_{\mathrm{v,K}}$ with the surface flattened to give a profile of the sub-surface bubbles clouds. Removing the surface displacements allows the calculation of time-averaged profiles, the data to be displayed in depth versus time coordinates, and comparison with previous experimental results [29, 42]. Figure 5.26 shows there is a moderate amount of variation in the top metre of the water column with bubble clouds extending down to approximately two metres. This is actually far shallower than has been experienced in previous experiments [29, 42]. There are two reasons for this. First, the experiments carried out by Trevorrow [42] and Farmer [29] were during periods of high (up to 20 m s^{-1}) wind speeds. Secondly, as shown in figure 5.27, there is no evidence that the IES measurements were taken in a period of high bubble activity and therefore bubble clouds would not be expected to penetrate to deeper depths.

The values shown so far (figures 5.24 to 5.29) for the volumetric backscatter strength have all been in terms of $S_{\mathrm{v,K}}$ (rather than the absolute value S_{v} since the calibration factor (K_{cal} in equation (5.9)) has yet to be determined.

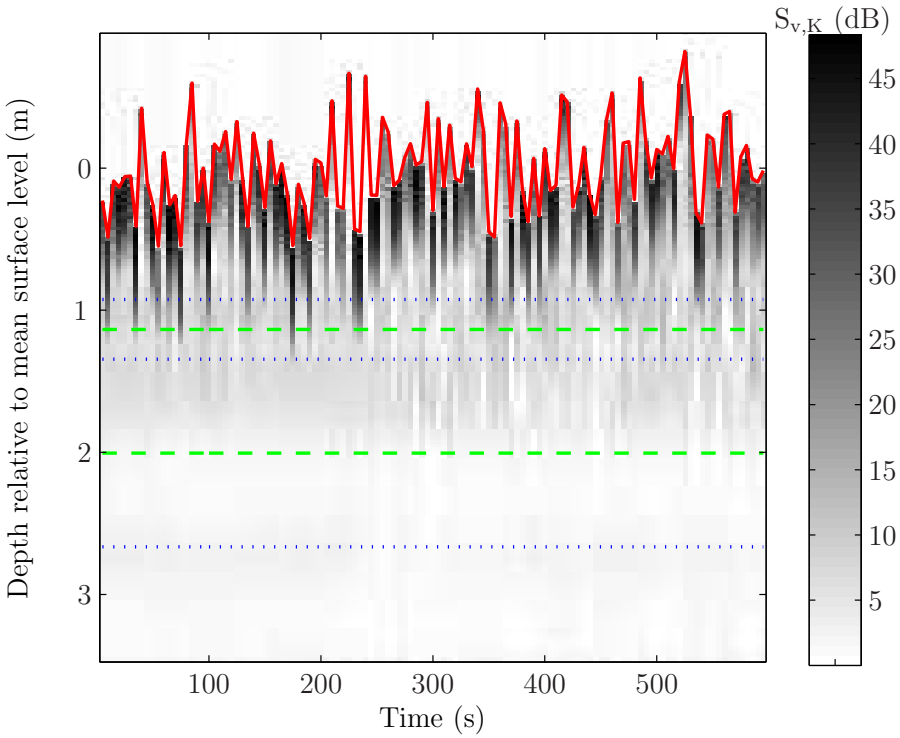

Figure 5.25: $S_{v,K}$ with surface mapped on as the bold red line, very clearly showing variation in the surface height. The positions of the hydrophones are shown as the blue dashed lines, and the measurement positions of the attenuation data are also shown (red dashed lines).

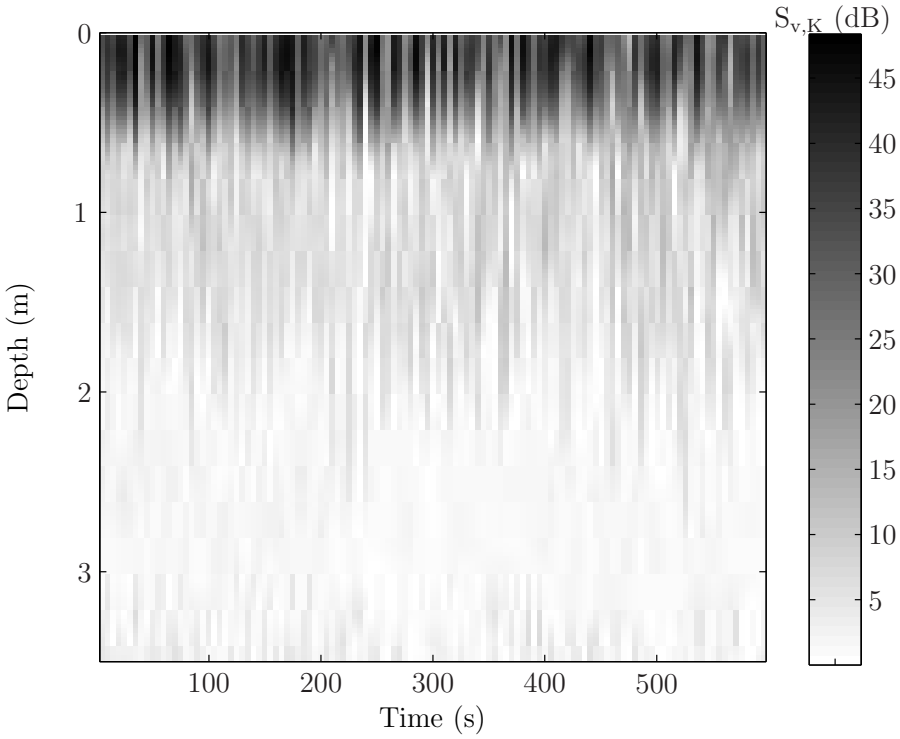

Figure 5.26: The volumetric backscatter strength before K_{cal} is applied, with surface variations removed.

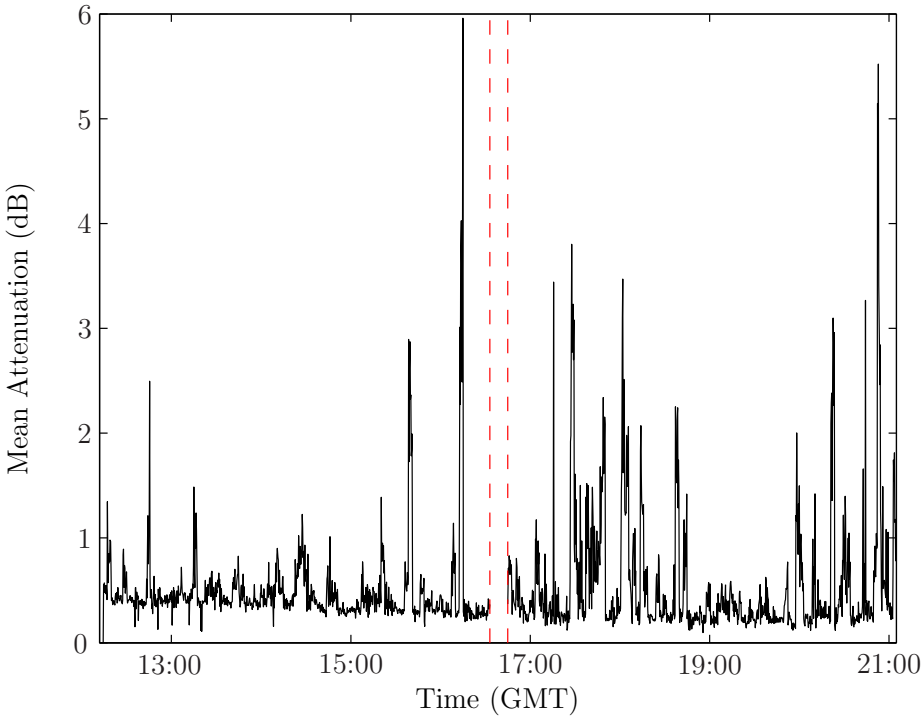

Figure 5.27: A representation of the mean attenuation throughout the deployment. Each point is made by averaging the pascal values of attenuation for each of the 14 frequencies in a single file. The IES system operated between the two red lines.

Calibration of the equipment during tests at NOC was not possible because of the sensitivity of the received waveform to the structure of the buoy. Even with careful attention to detail, it was very difficult to reassemble the buoy for calibration in a way that mimicked the setup during the cruise deployments. Therefore an alternative method must be used to calibrate the data. The next section describes how this was done.

5.4 Calibrating S_{v}

The values of $S_{\mathrm{v,K}}$ do not include the fixed calibration value, K_{cal}, at present but there is a technique, using the theory outlined in chapter 3, that can calibrate the $S_{\mathrm{v,K}}$ values using the bubble size distribution data. Figure 5.28 shows how we have the uncalibrated volumetric backscatter strength but also a known absolute value for the bubble size distribution at the measuring point shown on the figure. The next step is to take the mean of all the results throughout the period that the IES was operating. This is shown in figure 5.29. We now need to know the bubble size distribution at the time of the IES data. Figure 5.30 shows the mean of 45 bubble size distributions (approximately 10 minutes) taken before and after the IES data. Using the theory described in chapter 3, it is possible to calculate the volumetric backscatter strength from a known bubble size distribution. This is done using the following equation [105]:

$$s_{\mathrm{v}}(R_0) = \frac{1}{4\pi} \int \Omega_{\mathrm{scat}} n(R_0) \mathrm{d}R_0, \tag{5.10}$$

where Ω_{scat} is the scattering cross section defined as

$$\Omega_{\mathrm{scat}} = \frac{4\pi R_0^2}{((\frac{\omega_0}{\omega})^2 - 1)^2 + \beta_{\mathrm{tot}}}. \tag{5.11}$$

From figure 5.29, the value for $S_{\mathrm{v,K}}$ at 2 metres depth is 3.127 dB. The absolute value for S_{v}, calculated from the bubble size distributions using equations (5.10) and (5.11), is -75.785 dB at 2 metres depth. Therefore the

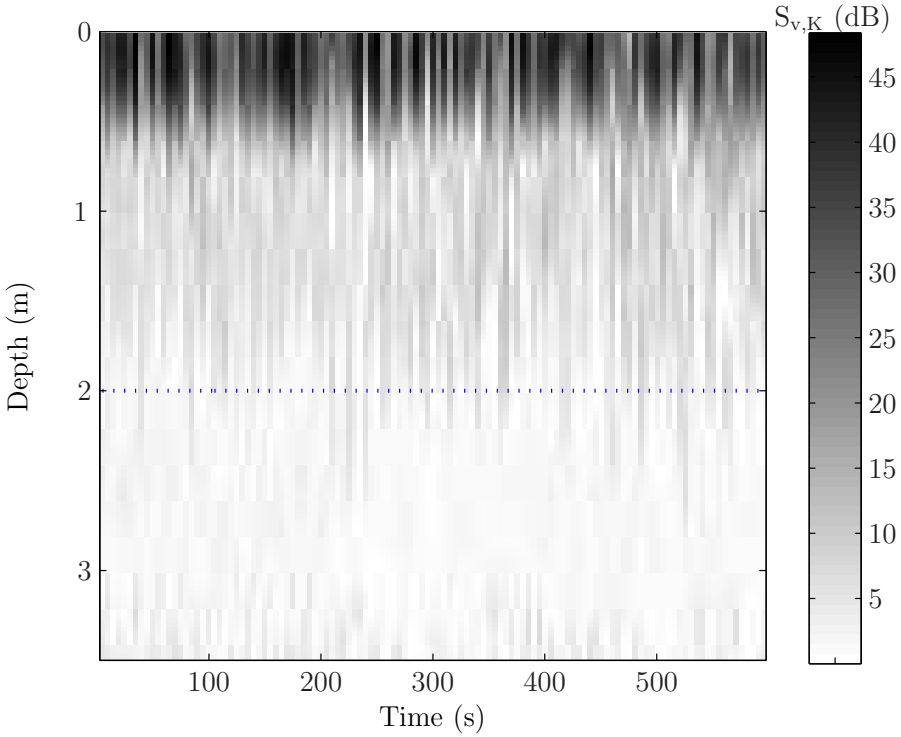

Figure 5.28: The volumetric backscatter strength (before K_{cal} is applied) with the position of the measured bubble size distribution between hydrophones 1 and 2 marked on as the dashed line.

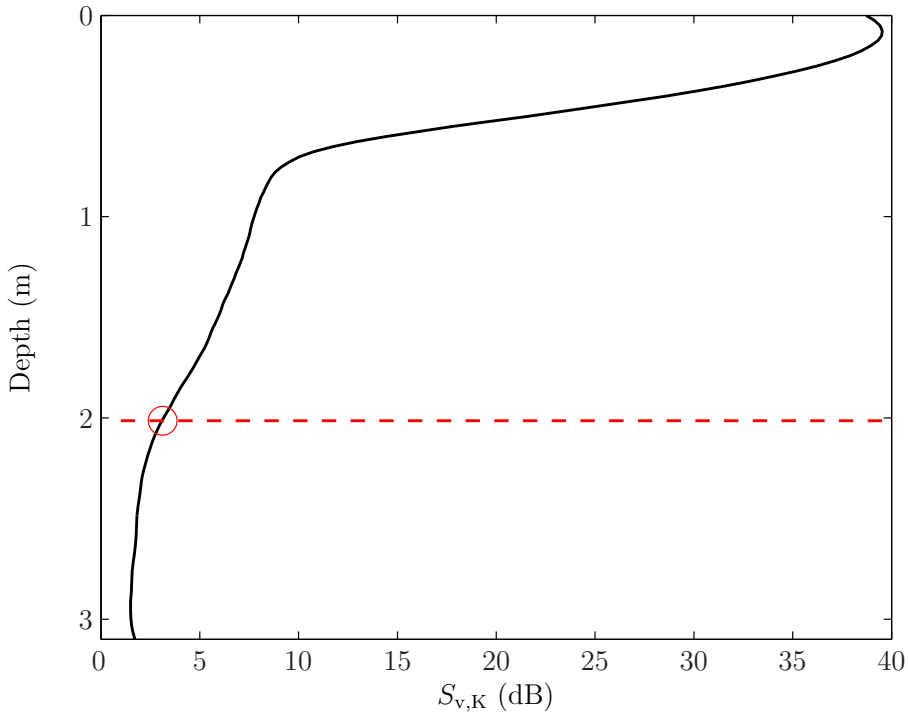

Figure 5.29: The mean $S_{v,K}$ for the ten minute period that the IES system was operating. The red dashed line shows the position of the known bubble size distribution.

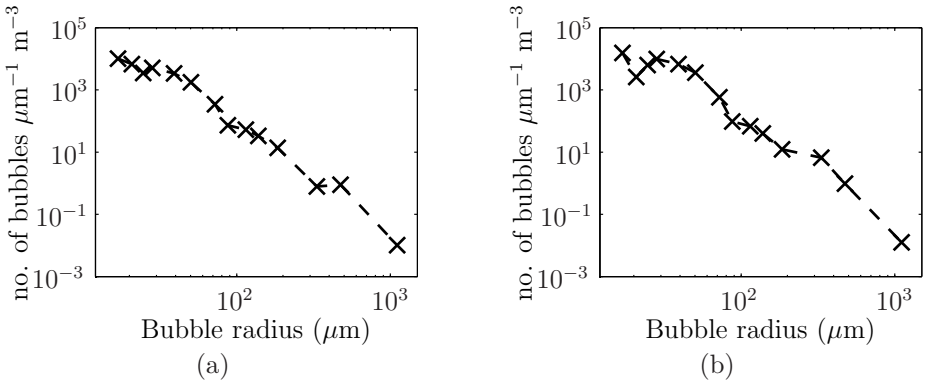

Figure 5.30: The mean of 45 bubble populations, spanning approximately 10 minutes, taken (a) before and (b) after the inverted echo sounder data.

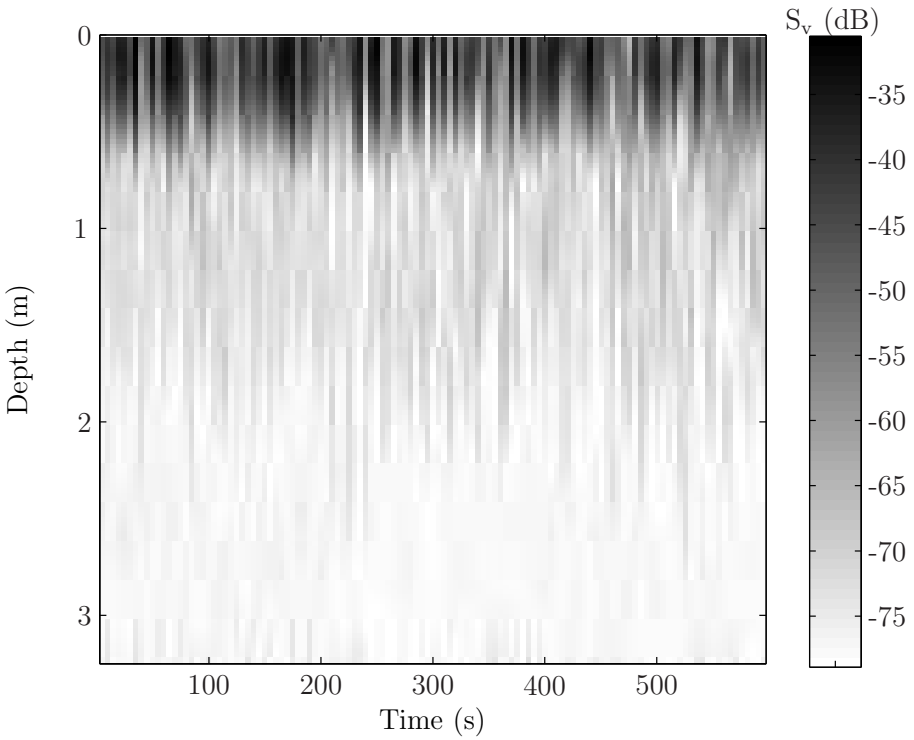

Figure 5.31: The final calibrated results from the IES data.

data of figures 5.24 to 5.29 can readily be expressed in absolute units using the simple calibration factor

$$S_{\mathrm{v}} = S_{\mathrm{v,K}} + 78.91 \text{ dB}, \tag{5.12}$$

giving a final calibrated result, shown in figure 5.31.

There is a slight increase in the bubble size distributions before and after the IES system was running. Therefore, an estimate of the uncertainty in the calibration can be calculated by looking at the difference between these populations. If the calibration is performed using only the populations from before the IES, S_{v} is given as -79.3 dB and with the populations from after the IES, $S_{\mathrm{v}} = -74.8$ dB.

Having now a calibrated dataset from the IES data, the bubble size distributions shown in figure 5.12 can now be scaled with depth using the mean

S_v values (as in figure 5.29), though naturally the calibrated values would be used. This can give invaluable information about the vertical profile of bubble density in the water column. Scaling the bubble size distributions in this way, however, is not so simple. Large bubbles naturally have more buoyancy than smaller bubbles and are therefore not so easily pulled down by turbulent forces. This means that after a bubble cloud has formed and evolved, larger diameter bubbles will generally be nearer the surface and smaller diameter bubbles will have been pulled down deeper. Therefore the shape of the bubble size distribution will change with depth. Theoretical models exist [62] which calculate the evolution of a sub-surface bubble cloud. The data presented in this chapter can be integrated into those models to produce simulations of sub-surface bubble clouds, allowing bubble size distributions to be calculated at any depth.

5.5 Summary

This chapter has presented results from the second deployment of the second sea trial which was the only deployment to return useful data. A large number of bubble size distributions along with their means have been calculated from attenuation data at two depths. Inverted echo sounder data has also been presented, showing the vertical and horizontal variation of the sub-surface bubble clouds. The IES data is calibrated using the attenuation data.

The mean values of the bubble size distributions can now be used as the basis for a gas flux model and this is discussed in more detail in the next chapter.

Chapter 6

Bubble Cloud and Gas Flux Modelling

The previous chapter presented results from the sea trials undertaken as part of this PhD. These results included inverted echo sounder data showing a profile of the sub-surface bubble clouds, and also attenuation data inverted to produce bubble size distributions. These measured data can be of enormous benefit when combined with models for bubble-mediated gas flux from sub-surface bubble clouds. This chapter describes the development of these models and how the measured data can be used with these models to produce meaningful results for gas exchange between the atmosphere and the ocean.

There are two contributors to gas flux between the atmosphere and the ocean: direct transfer and bubble-mediated transfer. As is mentioned in chapter 1, there is evidence that bubbles significantly increase the air-sea gas flux [7] during periods of increased sea-state. Bubbles start to have this effect when the wind speed is high enough to produce breaking waves, which entrain millions of bubbles as they break. One of the reasons for this increase is the ability of the bubbles to inject air into the sea even when the ocean is slightly supersaturated [106].

Liss and Merlivat [5] suggested gas transfer velocities, describing the total gas flux (direct and bubble-mediated), that were dependent on wind speed,

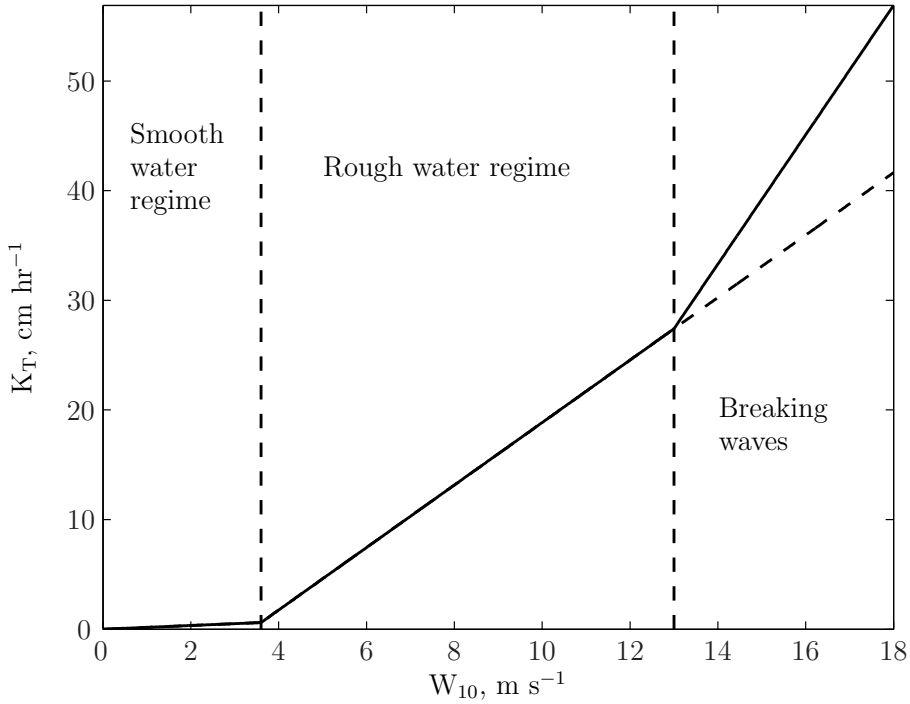

Figure 6.1: The three sea state regimes. The dashed line represents the rough water regime extended to high wind speeds.

given by

$$\begin{array}{lll} W_{10} < 3.6\text{ms}^{-1} & K_{\mathrm{T}} = 0.17W_{10} & \text{smooth water regime} \\ 3.6\text{ms}^{-1} < W_{10} < 13\text{ms}^{-1} & K_{\mathrm{T}} = 2.85W_{10} - 9.65 & \text{rough water regime} \\ W_{10} > 13\text{ms}^{-1} & K_{\mathrm{T}} = 5.9W_{10} - 49.3 & \text{breaking waves} \end{array} \tag{6.1}$$

where W_{10} is the wind speed in m s^{-1} at an elevation of 10 metres above sea-level and K_{T} is measured in cm/hr. Figure 6.1 shows the transfer velocity plotted for the three sea state regimes and also shows the rough water regime extended to high wind speeds. This extension represents the transfer velocity through direct transfer alone since the presence of bubbles from breaking waves is not accounted for. Though this approximation is not completely accurate, it does highlight the additional gas transfer induced by breaking waves. Keeling [14] also suggests, through his modelling work, that at wind-

speeds greater than approximately 10 m s^{-1} bubbles may make an important contribution to overall gas exchange. It is this additional exchange that will be explored in more detail in this chapter.

Estimating gas transfer through bubbles is not trivial. There is a complex relationship between the different gases whereas direct air-sea transfer does not possess any such complex relationship [55]. Because of this, it is important to know the history of a bubble if the gas flux is to be calculated. This can be determined through the use of a model of the evolution of sub-surface bubble clouds and this is explained in more detail in the next section.

Historically, inputs to bubble models and parameters used have mostly been based on theoretical estimates [55, 62]. They have also been limited by computational power. A novel aspect of this thesis is the use of actual measured data in the models and the ability to run these models with far greater computational power.

6.1 Bubble cloud modelling

More than one model for the evolution of sub-surface bubble clouds has been used here and each one is described in the following sections.

6.1.1 Thorpe model

Thorpe [62] established a model for bubble cloud evolution based on equations for the dynamics of bubbles described by Garrettson [107]. The model took account of bubble rise speeds, changes in hydrostatic pressure, gas flux in and out of the bubbles (for oxygen and nitrogen), and turbulence in the water. Recreating the model produced meaningful results (shown in figure 6.2) with bigger bubbles remaining near the surface and smaller bubbles penetrating deeper because of their lower rise speeds and therefore their increased ability to be dragged down by turbulence. The finer details of how the model was run are very similar to those of the second model used here and will therefore be described in the following section.

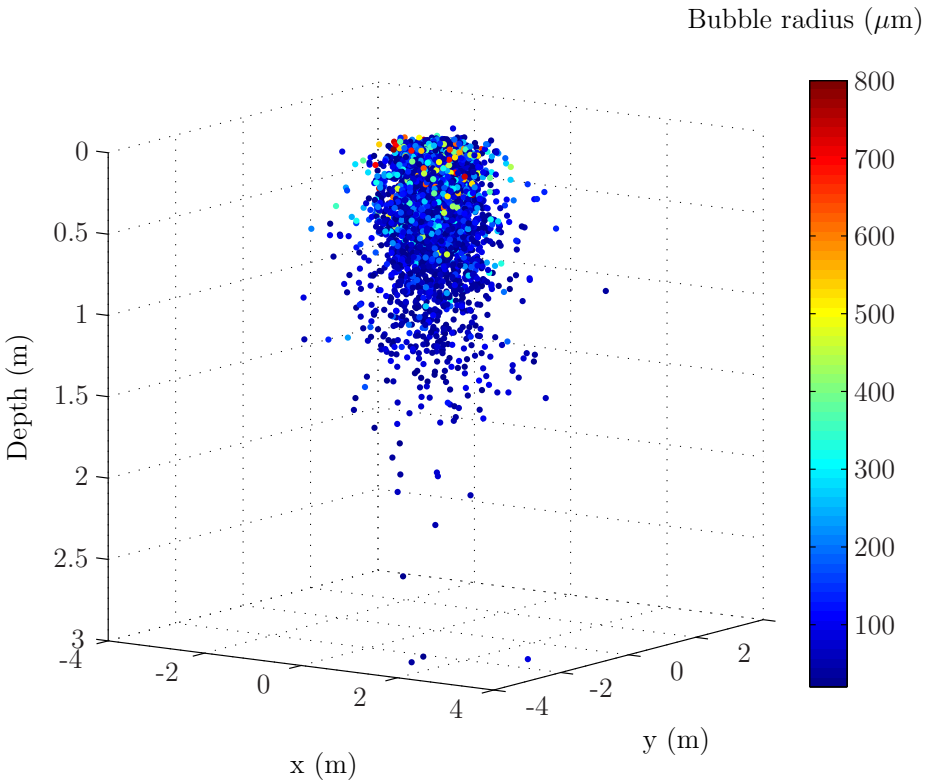

Figure 6.2: A three-dimensional view of the Thorpe model bubble cloud once steady state has been reached. Each second, 10000 bubbles ranging in radius from 10 μm to 10 mm were input at the surface. The turbulent diffusion coefficient was 0.01 m^2 s^{-1}, and water temperature was 10°C.

The key limitation in this model is the number of gases that can be represented in the flux equations. The equation for the change in mole fraction with each time step is given by

$$\frac{\mathrm{d}x_{\mathrm{m}}}{\mathrm{d}t} = \frac{3R_gT}{R_0(p_0R_0+2\sigma)}\left\{D_{\mathrm{mol},2}K_{\mathrm{ab},2}\mathrm{Nu}_2x_{\mathrm{m}}\left[(1-x_{\mathrm{m}})\left(p_0+\frac{2\sigma}{R_0}\right)-p_{\mathrm{p},2}\right]\right.$$
$$\left.-D_{\mathrm{mol},1}K_{\mathrm{ab},1}\mathrm{Nu}_1(1-x_{\mathrm{m}})\left[x_{\mathrm{m}}\left(p_0+\frac{2\sigma}{R_0}\right)-p_{\mathrm{p},1}\right]\right\}, \tag{6.2}$$

where $D_{\mathrm{mol,i}}$ are the diffusivities, $K_{\mathrm{ab,i}}$ the absorption coefficients and $\mathrm{Nu_i}$ the Nusselt numbers. The term $(1-x_{\mathrm{m}})$ is simply the mole fraction for one of the gases subtracted from the other. With equations of this form, it is not possible to include more than two gases, which is problematic when trying to gain a thorough understanding of bubble-mediated gas transfer.

The model in this form does not include the effect of Langmuir circulation, though Thorpe describes this effect elsewhere [64]. The turbulence used in this model is constant with depth.

6.1.2 Woolf and Thorpe model

Since the model of Thorpe [62] was not readily extendable for multiple gases, Woolf and Thorpe [55] took a different approach to the calculation of molar content. The molar content of each individual gas was calculated based on exchange coefficients and partial pressures, from which the new bubble radii could be calculated. This approach works very well and the four gases used by Woolf and Thorpe [55] are used throughout the rest of this chapter. The gases are nitrogen, oxygen, carbon dioxide and argon, and are the four gases with the highest volume-fraction in the composition of the atmosphere.

6.2 Gas flux model

The model developed by Woolf and Thorpe [55] is the foundation of the model used here. The model treats each bubble as an individual particle, whose motion and radius are changed and tracked throughout the model run. Each model run is broken down into small time steps and each bubble is subjected to a number of calculations (based on bubble dynamics and gas flux equations) at each time step. The theory behind these calculations is outlined in the following sections.

6.2.1 Bubble dynamics equations

There are a number of key equations used in the model which affect bubble dynamics. The pressure inside each bubble can be calculated using

$$p_{\mathrm{bub}} = p_{\mathrm{atm}} + \rho_{\mathrm{w}} g z + \frac{2\sigma}{R_0}; \tag{6.3}$$

where p_{atm} is the atmospheric pressure, $2\sigma/R_0$ is the excess pressure induced by surface tension (σ), and $\rho_{\mathrm{w}} g z$ is an approximate form [108] for the hydrostatic pressure.

Bubble rise speed is an important factor in the model and is different for hydrodynamically clean and dirty bubbles [63, 109] (see figure 6.3). A dirty bubble is a bubble covered in sufficient surface-active material for it to behave as a rigid body [55]. A clean bubble is completely free of surface-active material. The model used here assumes that the bubbles are hydrodynamically dirty since it has been shown that bubbles in sea water most typically behave as dirty bubbles [110–112]. The rise speeds for dirty bubbles are given as [63]

$$w_{\mathrm{b}} = \left(\frac{2R_0^2 g}{9\upsilon_{\mathrm{k}}} \right) [(y^2 + 2y)^{1/2} - y], \tag{6.4}$$

where υ_{k} is the kinematic viscosity and y is defined by

$$y = \frac{10.82\upsilon_{\mathrm{k}}^2}{gR_0^3}. \tag{6.5}$$

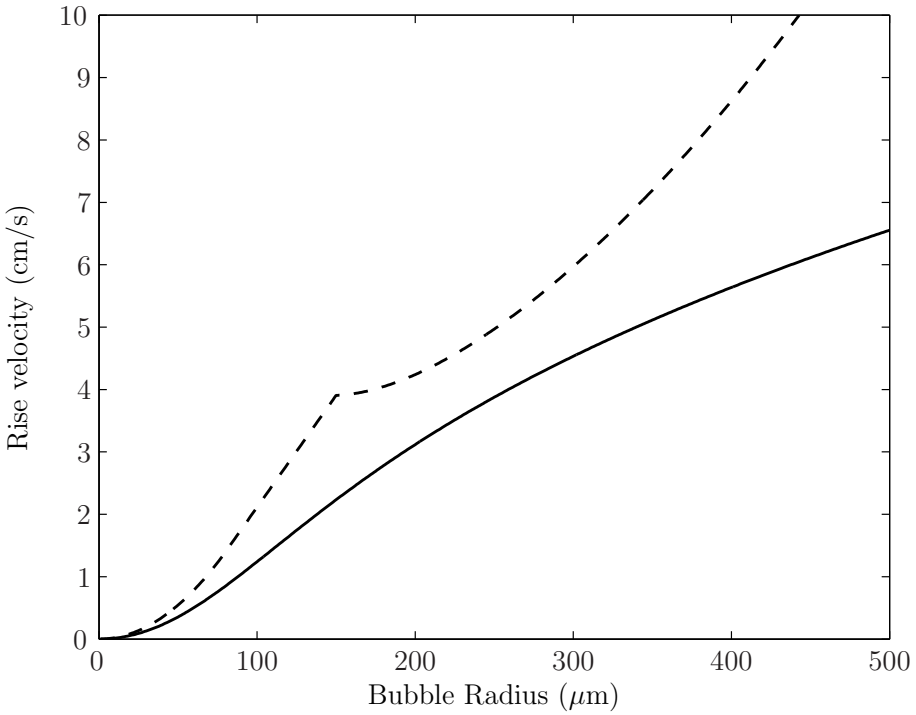

Figure 6.3: Bubble rise speeds for hydrodynamically clean (dashed line) and dirty (solid line) bubbles. The data are taken from Levich [109] and Thorpe [63].

6.2.2 Gas exchange equations

Before the gas flux across the bubble wall can be calculated, a number of parameters must first be found. The Reynolds number of each bubble and the Peclet number and Nusselt number of each gas in each bubble must be calculated. The Reynolds number gives a measure of the ratio of viscous forces to inertial forces for the flow around the bubble [113] and is the same for each gas. It is given by [61]

$$\mathrm{Re} = \frac{2R_0 w_\mathrm{b}}{v_\mathrm{k}}. \tag{6.6}$$

	Nitrogen	Oxygen	Carbon dioxide	Argon
Fraction in dry air	0.7809	0.2095	350×10^{-6}	9.3×10^{-3}
Coefficient of diffusion, D_{mol} ($\times 10^{-9} m^2 s^{-1}$)	1.8	1.7	1.3	1.7
Schmidt Number, Sc	772	818	1069	818
Solubility, S ($\times 10^{-6}$ mol $m^{-3} Pa^{-1}$)	6.29	13.0	445	14.2

Table 6.1: Standard values used for certain parameters in the model. Diffusion coefficient values are taken from Wise and Houghton [114] and Jähne *et al.* [115].

The Peclet number is another property of the interaction between a bubble and the surrounding fluid. It differs for each gas and is given by

$$\mathrm{Pe} = \frac{R_0 w_\mathrm{b}}{D_\mathrm{mol}} \tag{6.7}$$

where w_b is the bubble rise speed as defined in equation (6.4) and D_mol is the molecular diffusivity of each dissolved gas in water (values can be found in table 6.1). The Nusselt number for each bubble depends on the Reynolds number and Peclet number for each bubble. The following formulae were used (for hydrodynamically dirty bubbles),

$$\begin{aligned} &\mathrm{Nu} = 1.292\,\mathrm{Pe}^{1/9} && \mathrm{Pe} < 24.17 \\ &\mathrm{Nu} = (2/\pi)\mathrm{Pe}^{1/3} && \mathrm{Pe} > 24.17 \;\&\; \mathrm{Re} < 8.017 \\ &\mathrm{Nu} = 0.45\,\mathrm{Re}^{1/6}\mathrm{Pe}^{1/3} && \mathrm{Re} > 8.017. \end{aligned} \tag{6.8}$$

The concentration difference of each gas between the bubble and the water must also be calculated. The concentration of each gas in the water is calculated using

$$C_\mathrm{w,i} = S_\mathrm{i}\, f_\mathrm{frac,i}\, P_\mathrm{atm}\, \phi_\mathrm{sat,i}, \tag{6.9}$$

where i denotes each gas, S is the solubility, f_frac is the fraction in dry air and ϕ_sat is the saturation of each gas in the water. The concentration of each

gas in a bubble is given by

$$C_{\mathrm{bub,i}} = S_{\mathrm{i}}\, p_{\mathrm{p,i}}, \tag{6.10}$$

where p_{p} is the partial pressure in each bubble. The flux of gas into the bubble can now be calculated using

$$J_{\mathrm{bub,i}} = -4\pi R_0 D_{\mathrm{mol,i}}\, \mathrm{Nu_i}\, (C_{\mathrm{bub,i}} - C_{\mathrm{w,i}}). \tag{6.11}$$

6.2.3 Water motion equations

It is assumed that any motion of the water surrounding a bubble causes the bubble to move. The main factors effecting fluid motion are:

- The initial jet of water from a breaking wave.
- Turbulence in the water.
- Langmuir circulation.

In Woolf and Thorpe [55], the initial jet of a breaking wave was modelled by using a triangular source distribution of bubbles of the form

$$\begin{aligned} \partial n/\partial R_0 \partial z &= a(R_0)(1-2z) \quad 0 < z < 0.5\,\mathrm{m} \\ &= 0 \qquad\qquad\quad z < 0, z > 0.5\,\mathrm{m}, \end{aligned} \tag{6.12}$$

where $a(R_0)$ describes the size distribution. This approach does not attempt to model actual bubble motion resulting from the jet and, in fact, Woolf [15] describes the method as "necessarily arbitrary". Therefore the approach taken here is different. Each bubble is given an initial velocity (see section 6.4.3) which linearly reduces to zero as time progresses. The time for the velocity to reach zero should be approximately 1 second since Deane and Stokes [116] found through experimentation that the active phase of a breaking wave in which the primary plume formation occurs is on average 1 second in duration.

Turbulence is modelled through use of a Monte Carlo model. In each time step, each bubble is assigned a random motion in three dimensions. In the horizontal dimensions, each bubble is moved by a distance

$$\Delta x = v_0 \sin(\theta_{\mathrm{x}}) \tag{6.13}$$

and

$$\Delta y = v_0 \sin(\theta_{\mathrm{y}}), \tag{6.14}$$

where θ is chosen at random and v_0 is a prescribed velocity related to the turbulent diffusion coefficient and is given by

$$v_0 = \sqrt{6 K_{\mathrm{v}} \Delta t}, \tag{6.15}$$

where K_{v} is the turbulent diffusion coefficient and Δt is the time step. The vertical movement is given by

$$\Delta z = v_0 \cos(\theta_{\mathrm{z}}). \tag{6.16}$$

The depth dependent turbulent diffusion coefficient is given by

$$K_{\mathrm{v}}^{\mathrm{z}} = 0.4 K_{\mathrm{v}} z. \tag{6.17}$$

For depths less than 0.1 metres, $K_{\mathrm{v}}^{\mathrm{z}}$ is set at the value for 0.1 metres. This technique is based on previous theoretical proposals [117, 118] but adjusted here empirically in an attempt to mimic observed distributions. Quantitative values for K_{v} are outlined in section 6.4.3.

Langmuir circulation is a wind and wave driven phenomenon in which an array of vortices of alternating signs exists below the ocean surface with horizontal axes parallel with the wind direction [119]. It is beyond the scope of this PhD to model the effects of Langmuir circulation perfectly, though the realism of the gas flux model can be improved by including a simplified model for Langmuir circulation [55]. The effect is therefore modelled as a

fixed field of cells defined by the stream function

$$\Psi_{\mathrm{L}} = \Psi_0 \sin k_{\mathrm{L}} z \sin l_{\mathrm{L}} y, \tag{6.18}$$

where k_{L} and l_{L} are the vertical and horizontal repetition lengths of the cells. Ψ_0 is given by

$$\Psi_0 = \frac{V_{\mathrm{L}}}{l_{\mathrm{L}}}, \tag{6.19}$$

where V_{L} is the maximum downward or upward velocity (a user defined parameter). The horizontal velocity component can then be calculated using

$$\mathrm{d}y/\mathrm{d}t = \partial\Psi_{\mathrm{L}}/\partial z, \tag{6.20}$$

and the vertical velocity component can be calculated using

$$\mathrm{d}z/\mathrm{d}t = -\partial\Psi_{\mathrm{L}}/\partial y. \tag{6.21}$$

Quantitative estimates for these parameters are detailed in section 6.4.1.

6.2.4 Input bubble population

Deane and Stokes [116] made some pioneering measurements of breaking waves and the initial bubble size distribution they produce. They found that the spectrum exhibits two power-law scales, with an increase of slope for bubbles larger than 1 mm in radius. This is caused by larger bubbles being affected by turbulent fragmentation and smaller bubbles being created by jet and drop impacts on the wave face. The spectrum can be seen in figure 6.4. For bubbles smaller than 1 mm, the number of bubbles varies with $R_0^{-10/3}$ and for bubbles larger than 1 mm, this varies with $R_0^{-3/2}$. An upper cut-off of 10 mm was chosen as this is approximately the point at which there is less than 1 bubble m^{-3}. A lower radius cut-off of 10 μm was chosen since this was deemed sufficiently low that very few bubbles would initially be formed at this radius. Testing of the model using only the outer few radii confirmed

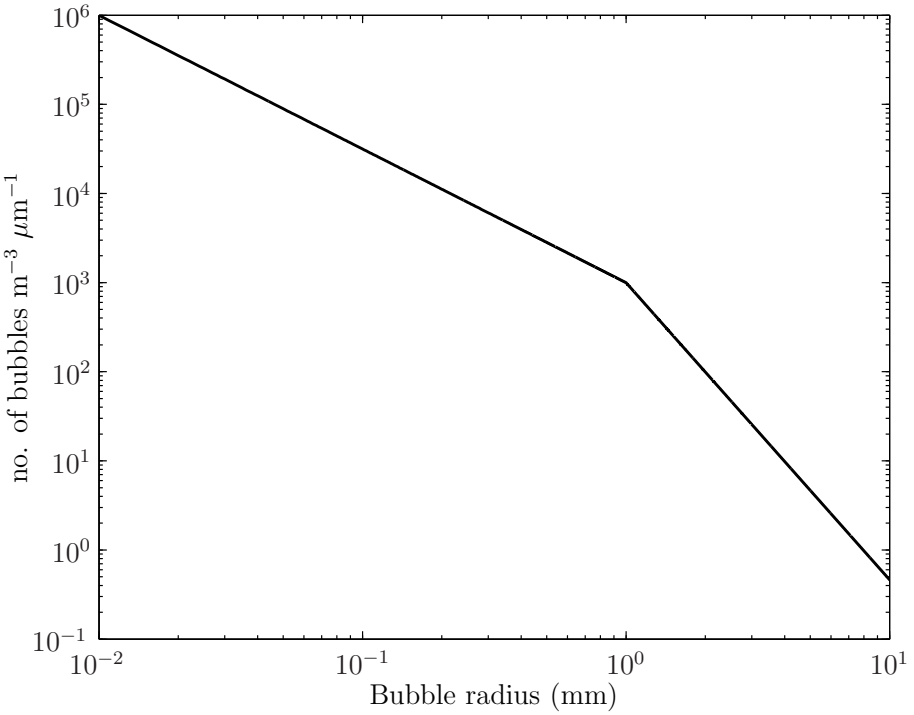

Figure 6.4: Best fit lines extrapolated for data measured under a breaking wave by Deane and Stokes [116] and used here for the initial bubble size distribution. For bubbles smaller than 1 mm, the number varies with $R_0^{-10/3}$. For bubbles larger than 1 mm, the number varies with $R_0^{-3/2}$.

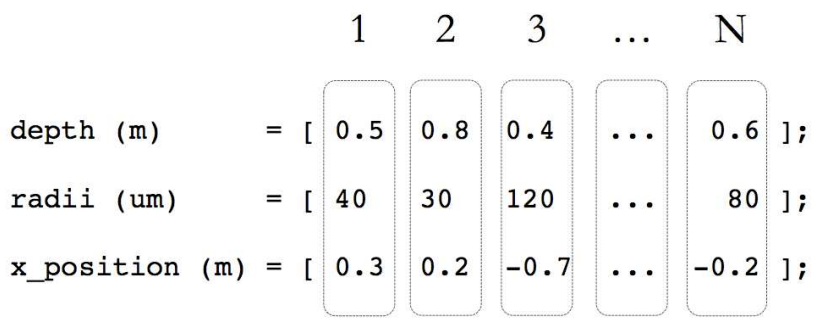

Figure 6.5: MATLAB® row vectors for some of the bubble properties, with the indices grouped to show the bubble numbering system for bubbles numbered 1 to N. The values shown here are fictional and for illustrative purposes only.

that these were viable assumptions since these tests resulted in no bubbles at the measurement depths.

The input population is spread randomly over a breaking area to simulate a breaking wave more realistically. It is also possible to change the depth at which the bubbles are inserted into the model in order to simulate surface disruption that may occur during a breaking event.

6.2.5 Modelling process

With the core equations in place, it is possible to set about modelling the evolution of the bubble cloud. The model was implemented using MATLAB®. Each bubble is modelled individually and each property of the bubbles is stored in its own vector so that first index in each vector corresponds to the properties of the first bubble, the second index to the second bubble, the third index to the third bubble and so on. Figure 6.5 portrays this in a more visual way. With the bubble properties in vectors, it is then easy to perform vector calculations for all the bubbles at the same time whilst maintaining individual bubble properties.

Each model run is split up into small time steps (see section 6.3.1 for

more details) and for each time step the following calculations are made:

- New bubbles are added to the model, if specified.
- Bubble rise speeds are calculated.
- Reynolds numbers, Peclet numbers and Nusselt numbers are calculated.
- The concentration difference and the gas flux are calculated.
- New bubble radii are calculated based on the new total number of moles in each bubble.
- Bubbles that have dissolved are removed from the simulation.
- Langmuir circulation effects, the turbulent motion of the surrounding water and the rise velocities are applied to the bubbles.
- Bubbles that have surfaced are removed from the simulation.
- New partial pressures are calculated.

Depending on the type of model run, this process is repeated until all the bubbles have either surface or dissolved (in the case of a single initial injection), or the bubble cloud has reached a steady state (in the case of repeated input of bubbles). At each step, the gas flux from each bubble is logged for reference once the model has finished.

6.3 Computational power

Computational power has vastly increased since Woolf and Thorpe [55] originally implemented their model. This section highlights some of the key aspects of progress possible with increased computational power.

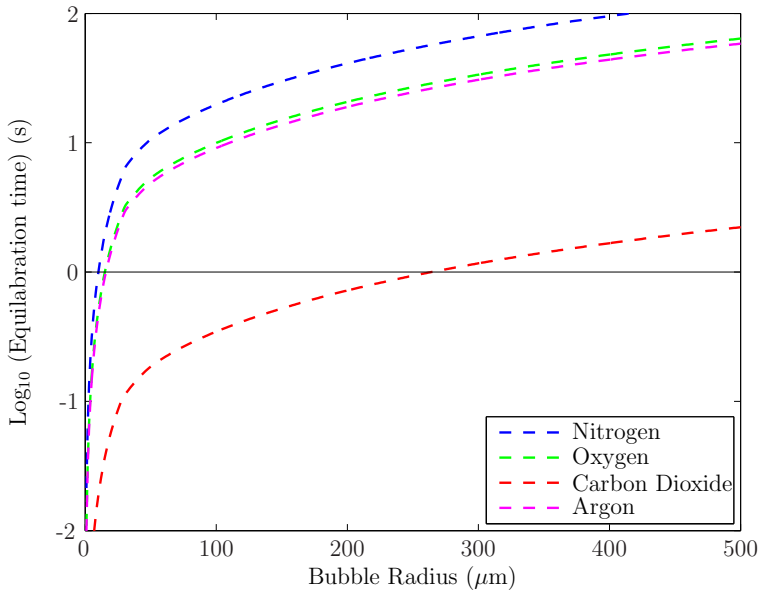

Figure 6.6: The equilibration times for the four gases for a range of bubble radii. The bubbles modelled here are hydrodynamically dirty.

6.3.1 Model time step

With the computational power available to them, Woolf and Thorpe [55] were limited to a time step of 1 second. This is problematic because of the equilibration time of the gases. In each time step, the concentration of a gas in a bubble exponentially approaches an equilibrium value with the surrounding water. The time taken for this equilibrium value to be reached is the equilibration time. Figure 6.6 shows the time taken for each gas to reach equilibrium for a range of bubble radii. It can be seen that if the time step is 1 second, carbon dioxide will equilibriate in bubbles smaller than approximately 250 μm. Therefore, Woolf and Thorpe [55] assumed that carbon dioxide would equilibriate with each time step and they set the value to that of the surrounding water. Whilst this is not an unreasonable approximation, it is not entirely accurate and with greatly increased computational power it is possible to reduce the time step to a value lower than the equilibration time of carbon dioxide in small bubbles.

6.3.2 Number of bubbles in input population

As mentioned in section 6.2.5, each bubble is treated as a separate particle. If the number of bubbles in the model is increased, so is the length of the property vectors and in turn the computational load is increased. With the computational power available today, it is possible to model millions of bubbles, although this is not an instantaneous process. Model runs typically took between 2 hours and 2 days to complete depending on the time step and number of bubbles chosen. Clearly, if many runs of the model are to be completed, minimising the time taken for the model to finish whilst still maintaining an acceptable level of accuracy is important. The total number of bubbles between 10 μm and 10 mm in the population shown in figure 6.4 is approximately 19 million bubbles. Now take for example a reduction in this number by a factor of 100. This results in an input population of approximately 200000 bubbles and can be seen in figure 6.7. When the model has finished, any resulting data is scaled up accordingly (in this case by a factor of 100). However, a problem arises for larger bubbles with a total number of less than 1. Since each bubble in the model is represented by an index, there can only be whole numbers of any bubble size. So for bubbles below the line on figure 6.7, the number must be rounded to either 1 or 0. This causes inaccuracies in the number of bubbles input to the model, though this effect is considered small since the large radii bubbles quickly rise out of the water. The resulting bubble size distributions are also affected. Whilst there is little impact on the amplitude of the distributions, quantisation of the data occurs for more bubble radii as the input population is increasingly scaled down. Figure 6.8 shows the effect of these inaccuracies. For many of the runs undertaken in the parameter study (see section 6.4) it was deemed acceptable to use a reduced input population in order to reduce processing time. However, for the final results, as many bubbles as is computationally possible are used to ensure the maximum attainable accuracy.

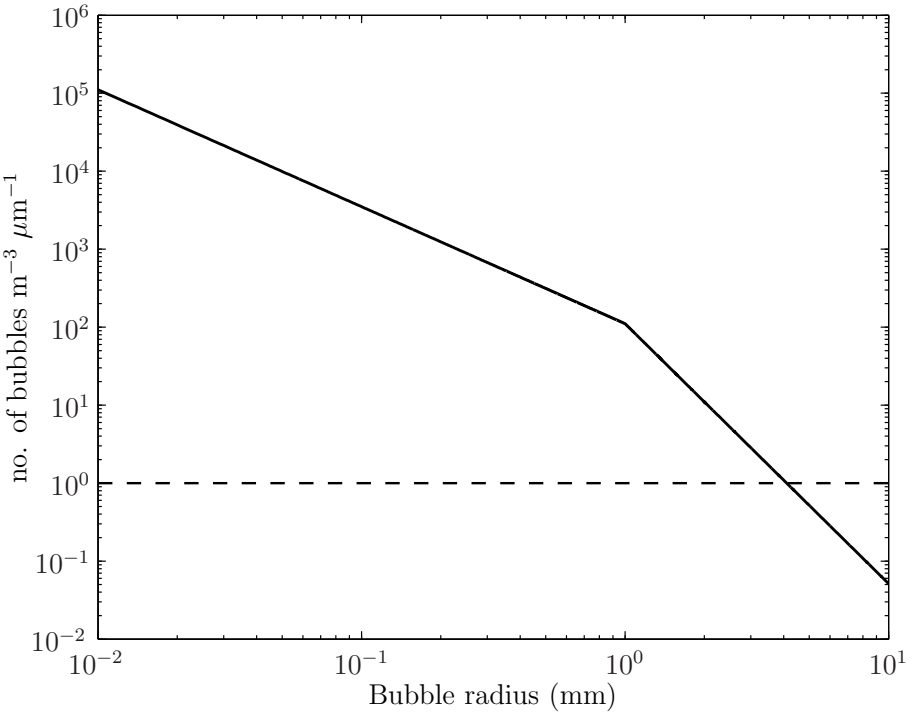

Figure 6.7: The input population taken from figure 6.4 and reduced by a factor of 100. A horizontal line drawn at y=1 marks the point below which rounding errors become significant.

6.4 Parameter study

Now that the model for bubble cloud evolution and bubble-mediated gas flux has been developed, it is important to relate it to the data measured in the Atlantic Ocean (see chapters 4 & 5). This is achieved by trying to recreate as accurately as possible the oceanic conditions that the measurement equipment experienced in the experiments and apply this to the model. Then once the model has finished, the bubble size distribution is taken and compared to that of the measured data.

Many, though not all, of the parameters in the model can be set at values measured by other experimenters in the Atlantic Ocean. The following section explains how some of these parameters were calculated.

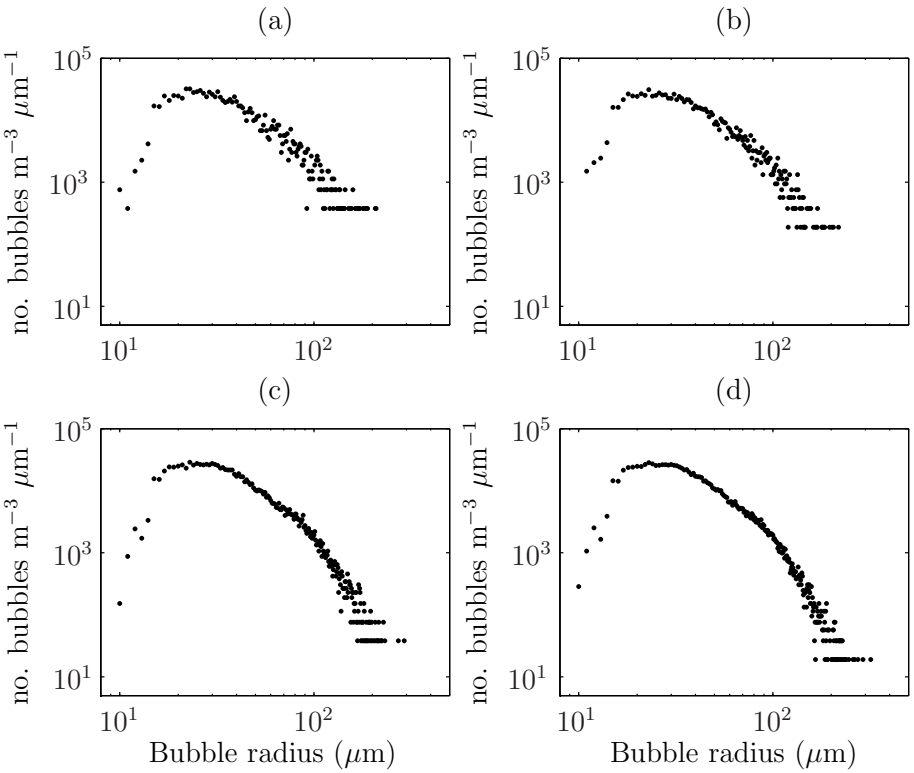

Figure 6.8: Bubble size distributions produced by four identical model runs. The number of bubbles in the input population was the only variable. (a) used 50000 bubbles for the input, (b) used 100000, (c) used 500000 and (d) used 1 million. Each time, the size distribution is scaled up by the factor with which the input population was initially scaled down.

6.4.1 Ancillary data applied to the model

The spar buoy was not the only piece of equipment being used as part of the D320 cruise. Many other measurements were being taken by many different pieces of equipment [120]. These measurements can be used to estimate some of the parameters in the model.

An autonomous atmospheric measuring system, AutoFlux [103], developed at the National Oceanography Centre, Southampton, was installed on the ship. This system measures water temperature and the mean value (17°C) from the day of measurements can be used in the model. It is deemed that, for reasons outlined in chapter 5, it is reasonable to assume that the temperature of the water by the ship is approximately equal to the temperature of the water surrounding the buoy. This assumption about the meteorological conditions is validated further by comparing wind speeds measured at the ship and near the buoy (see figure 6.9). The wind speeds can be used to estimate the scales for the Langmuir cells. Thorpe *et al.* [121] give the horizontal distance between Langmuir cells as

$$l_{\mathrm{L}} = 0.47W_{10} + 9.87, \tag{6.22}$$

where W_{10} is the wind speed corrected to 10 metres. Using a mean value for wind speed of 14 m s^{-1}, the horizontal spacing for the Langmuir cells is approximately 16 metres. The depth of the Langmuir cells is generally agreed to be approximately half the length of the horizontal spacing [122, 123], therefore a value of 8 metres is used.

It is important to decide the number of seconds to use between inputs of bubbles in the model. Data from the downward looking cameras mounted in the dome on top of the spar buoy can be used to assess the frequency of breaking waves in the measurement period. This is not an ideal approach since the cameras only operated during daylight hours and therefore switched off at 18:00 GMT, just as the sea state was building, and before many of the bubble populations were measured. However, it is possible to infer an esti-

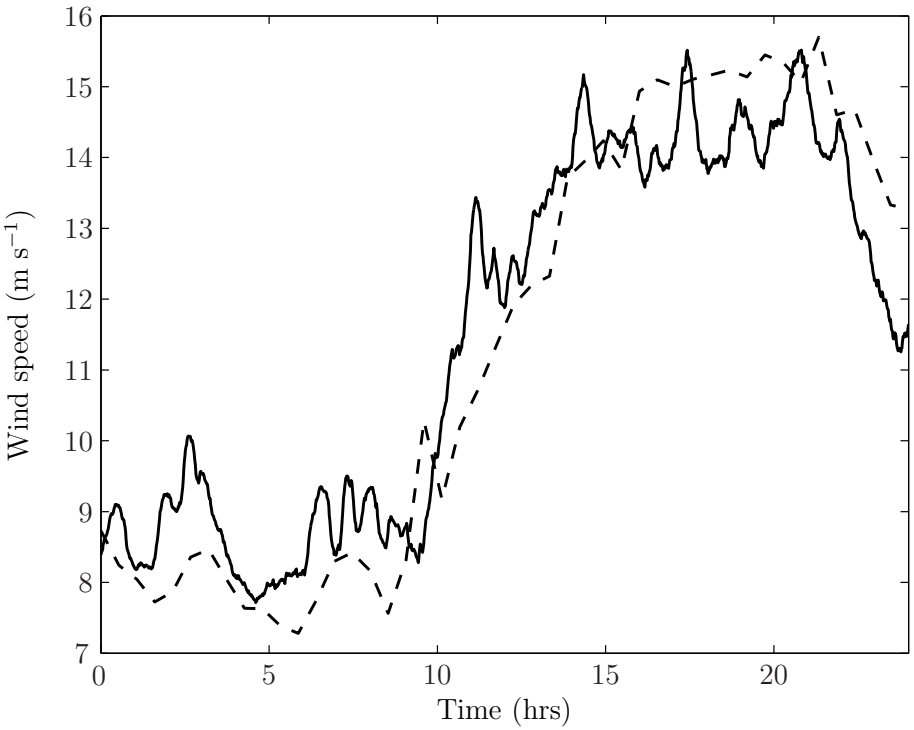

Figure 6.9: Wind speeds as measured by AutoFlux on the ship (the solid line) and the ASIS-2 buoy, located near the spar buoy (dashed line). Both datasets have been corrected to 10 metres using techniques outlined in [104]. The ASIS-2 data was kindly supplied by Professor William Drennan of RSMAS, University of Miami.

Parameter	Value	Units
Gravitational force	9.81	$m\ s^{-2}$
Kinematic viscosity	1.39×10^{-6}	$m^2\ s^{-1}$
Molar gas constant	8.314	$J\ mol^{-1}K^{-1}$
Bubble surface tension coefficient	3.6×10^{-2}	$N\ m^{-1}$
Water density	1025	$kg\ m^{-3}$
Atmospheric Pressure	101325	Pa

Table 6.2: The standard values used for some of the parameters in the model.

mate of the breaking frequency using this data. Figure 6.10 shows an example of a breaking wave caught on camera. Video data throughout the day was analysed to find the frequency of breaking waves. The results are shown in figure 6.11. The figure shows the time between breaking events decreasing as time progresses. It has been shown that breaking wave frequency is greater in developed seas than in developing seas [124] which suggests that the breaking frequency will continue to increase. The increasing wind speed is shown in figure 6.9 and the steadily increasing sea state is shown in figure 5.21. It is important to take into account the fact that only waves breaking within the field of vision of the camera could be recorded and shown in figure 6.11. Throughout the analysis, many waves could be heard breaking nearby and these would have effected the bubble populations surrounding the buoy. Also, the bubble populations shown here would likely have been the result of one or two large waves breaking within several seconds of each other. With all of these factors in mind, the time between breaking events was set to approximately 10 seconds.

6.4.2 Standard value constants

Some of the values used in the model are already displayed in table 6.1. There are many more parameters that use standard values and these are displayed in table 6.2.

(a)

(b)

Figure 6.10: Still images taken from the downward looking video camera in the dome on top of the buoy. (a) Shows the breaking wave hitting the buoy and (b) shows the sub-surface bubble clouds resulting from the breaking wave. The images were taken on 29th June 2007 at 17:58 GMT. Images courtesy of Robin Pascal of the National Oceanography Centre, Southampton.

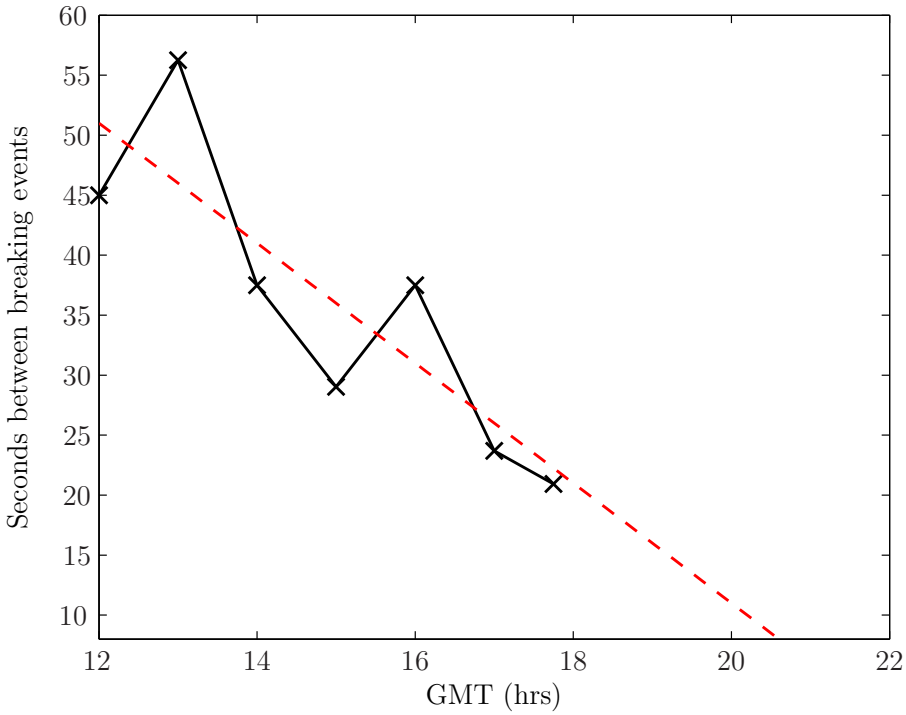

Figure 6.11: The number of seconds between each breaking event (solid black line) between noon and 18:00 on 29th June 2007, the day of measurement on the second deployment of D320. Each point on the graph represents the mean of a 15 minute sample. The dashed red line is a linear fit to the video data.

6.4.3 Unknown parameters

Many of the parameters for the model are now tied down to specific values based on either standard constants or meteorological conditions measured at the time of the experiments. The remaining parameters can be varied now in order to obtain the best fit between the measured bubble populations and the populations taken at the end of a model run. These parameters are:

- The maximum upward/downward velocity from the Langmuir circulation.
- The initial input jet velocity.

- The time for the jet velocity to reach zero after injection.
- The physical size of the breaking wave.
- The insertion depth for the bubbles.
- The turbulent diffusion coefficient.

With this many parameters to vary, and the time it takes for a standard model run (between 20 and 40 hours), it simply was not possible to run a standard automated parameter study. If each parameter is given 10 values to vary between, approximately 30 million hours of computational time (at current rates) would be required. Therefore a manual approach was taken to find the best fit with the parameters. Each parameter was varied around a starting value while the others were held constant in order to find the effect of each parameter on the resulting population. Sensible starting values for the maximum velocity from the Langmuir circulation (15 cm s^{-1}) and the turbulent diffusion coefficient (1×10^{-2} m^2 s^{-1}) could be taken from Woolf and Thorpe [55]. Deane and Stokes [116] show the active phase of a breaking wave, where primary plume formation occurs, to last for approximately 1 second and therefore this was set as the starting value for the time for the jet velocity to reach zero. A study of some relevant literature on plunging jets [125, 126] reveals an inception velocity for turbulent jets of approximately 0.8 m s^{-1} and upwards. A starting value of 1 m s^{-1} was therefore used for the initial jet velocity.

With initial values set, an extensive study was undertaken, making use of the university computer cluster, Iridis. Iridis has over 1000 processor cores and allows many jobs to be run simultaneously. Without this, the parameter study would not have been completed.

Each time a set of parameters was tested, the model would be run until the bubble cloud had reached steady state. This is when the number of bubbles in the cloud does not significantly change with each subsequent input of bubbles (see figure 6.12). Once this had been reached, bubble size distributions were taken at depths corresponding to the measured data, i.e., 1.15 metres and 2

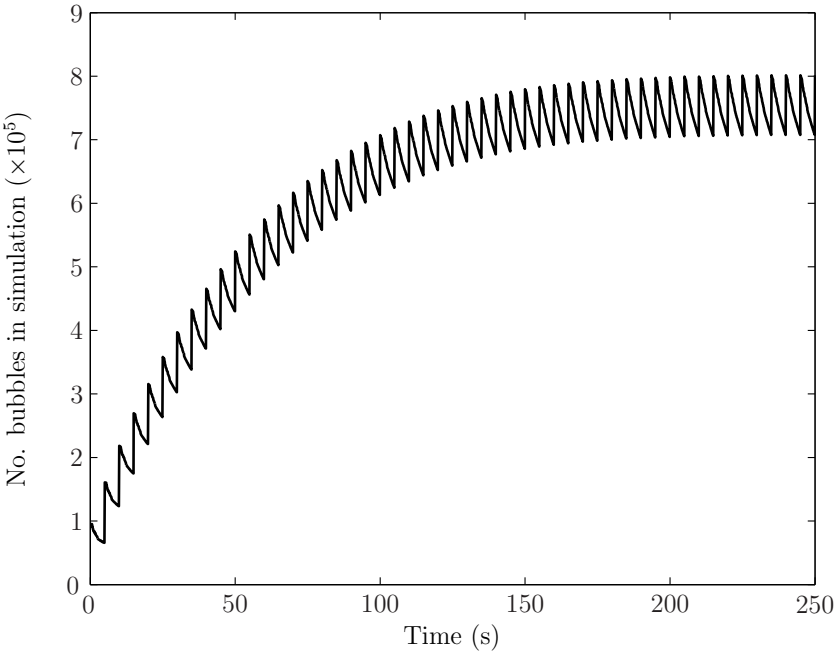

Figure 6.12: A plot of the number of bubbles in the simulation through time. The cloud has clearly reached steady state by the end of the model run. The curve is toothed because of the bubble input every 10 seconds.

metres. These could then be directly compared with the measured bubble populations (see chapter 5).

Eventually, after hundreds of hours of computational time, a set of parameters was settled upon that produced the best fit for the bubble size distributions at both depths. These results are presented in the following section.

6.5 Gas flux model results and analysis

Using the right set of parameters, some taken from ancillary data and others found through trial and error, a best fit solution between the measured data and the modelled data is now settled upon. These final results are presented in this section.

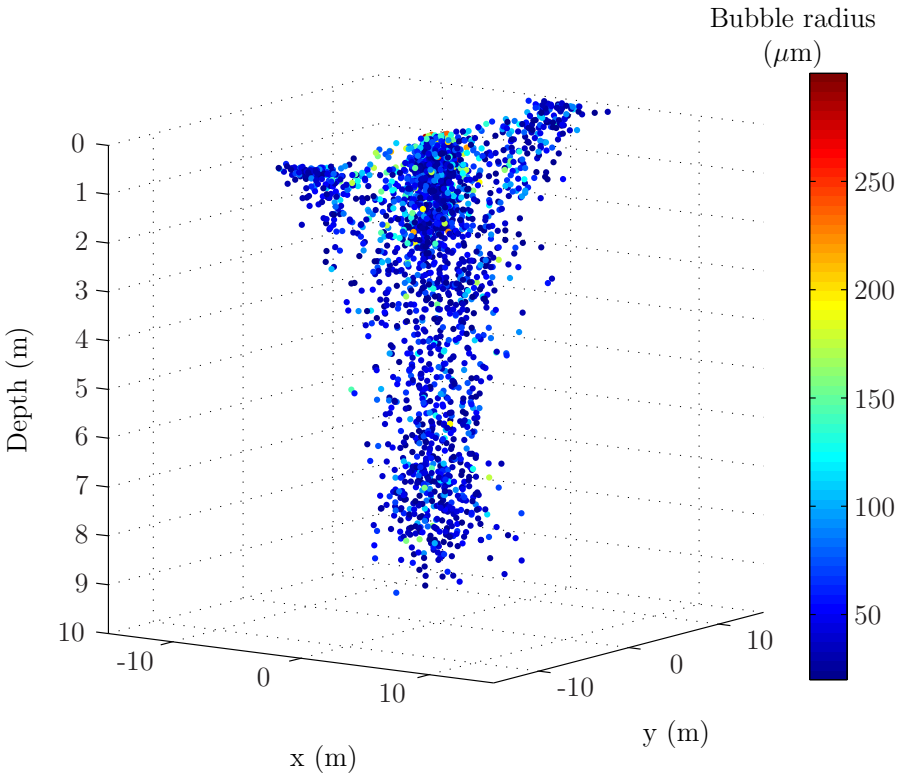

Figure 6.13: The bubble cloud at the end of the model run. The helical flow of the Langmuir cells can be seen. The population shown here is from a run with 100000 bubbles in the input population, and only 1 in every 100 bubbles is plotted. Input parameters can be seen in table 6.3.

6.5.1 Bubble size distributions

The initial step in the modelling process was to find a set of parameters that produced a best fit between the measured bubble size distributions and those resulting from the model. A comparison between these datasets can be seen in figure 6.14. The figure shows very good agreement at both depths for bubbles with radii between 16 and 187 μm. The agreement is less convincing for the larger bubbles. It was not possible to increase the number of large bubbles in the model without impacting the rest of the spectrum. It is difficult to tell whether this error is due to the number of the cycles in the low frequency acoustic pulses being too few and therefore causing errors or

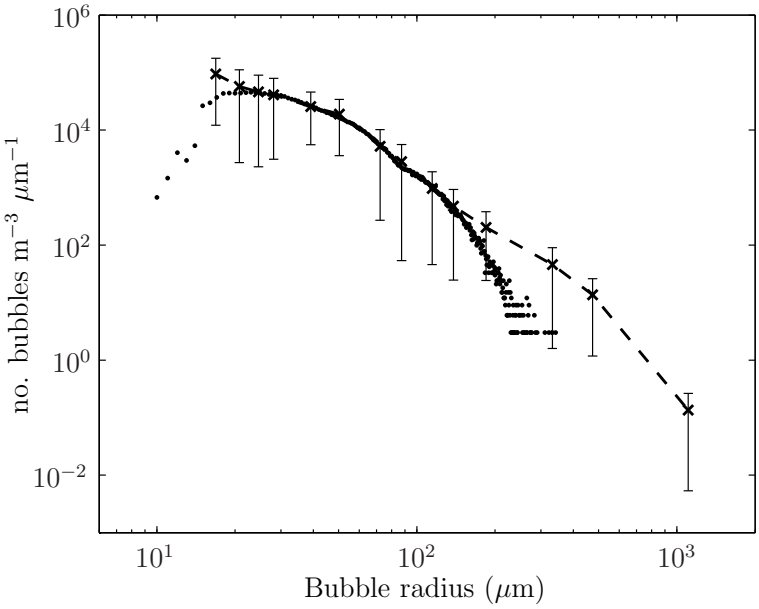

(a)

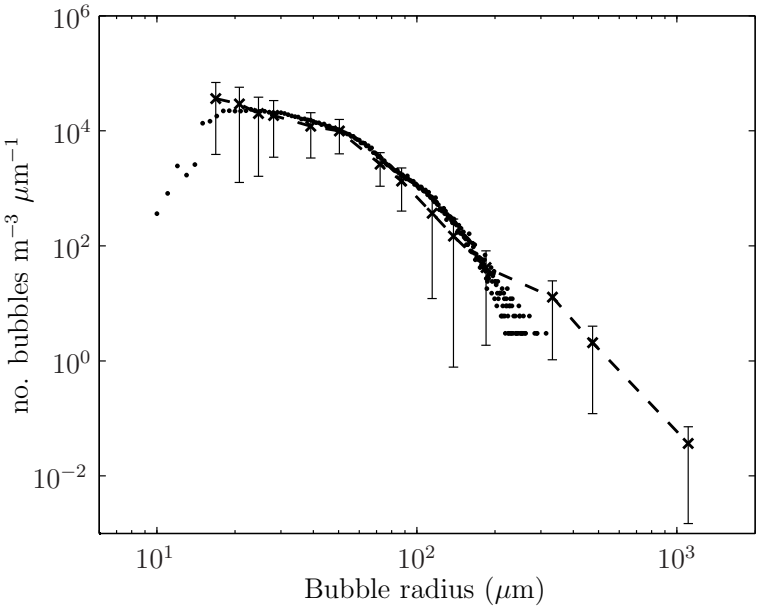

(b)

Figure 6.14: Bubble size distributions taken from the mean of the measured data (dashed line with crosses) and after the completion of the model (circles). (a) shows the distributions at 1.15 m depth and (b) shows them at 2 m depth. The uncertainty bars show one standard deviation from the mean.

whether it is something inherent in the model (in which case further investigation into the model would be required, though this is beyond the scope of this PhD). Nevertheless, the fit is very good for most of the bubble sizes, and this parameter set (see table 6.3) is used throughout this section. It is interesting to note the location of the peak in the bubble size distribution, at approximately 20 μm, agrees well with previous open ocean measurements [29, 30].

Parameter	Value	Units
Turbulent diffusion coefficient	1×10^{-2}	$m^2\ s^{-1}$
Maximum downwelling/upwelling velocity	0.185	$m\ s^{-1}$
Initial jet velocity	0.42	$m\ s^{-1}$
Length of initial jet	1.1	s
Bubble insertion depth	0.035	m
Time between breaking waves	8	s

Table 6.3: The final parameters used in the gas flux model to produce the populations shown in figure 6.14.

6.5.2 Uncertainty analysis

As is mentioned in section 5.1.5, there is uncertainty in the bubble size distributions arising from the baseline measurement. It is possible to follow this uncertainty through and assess the impact on the gas transfer coefficients. In order to do this, the best fit for the minimum and maximum uncertainty in the bubble size distributions must be found. Repeating the full procedure found in section 6.4 would take too much time and therefore a simplification is undertaken. By varying the number of bubbles in the input population for the computer model, the resulting bubble size distributions can be scaled up and down. Having run the model for a range of input populations, the best fit is taken for the minimum and maximum uncertainties in the measured results. Figure 6.15 shows the best fit found in each case. The resulting scaling of the results is followed through in section 6.5.5. It was found that a scaling down of 46% produced the best fit for the minimum bubble size distributions

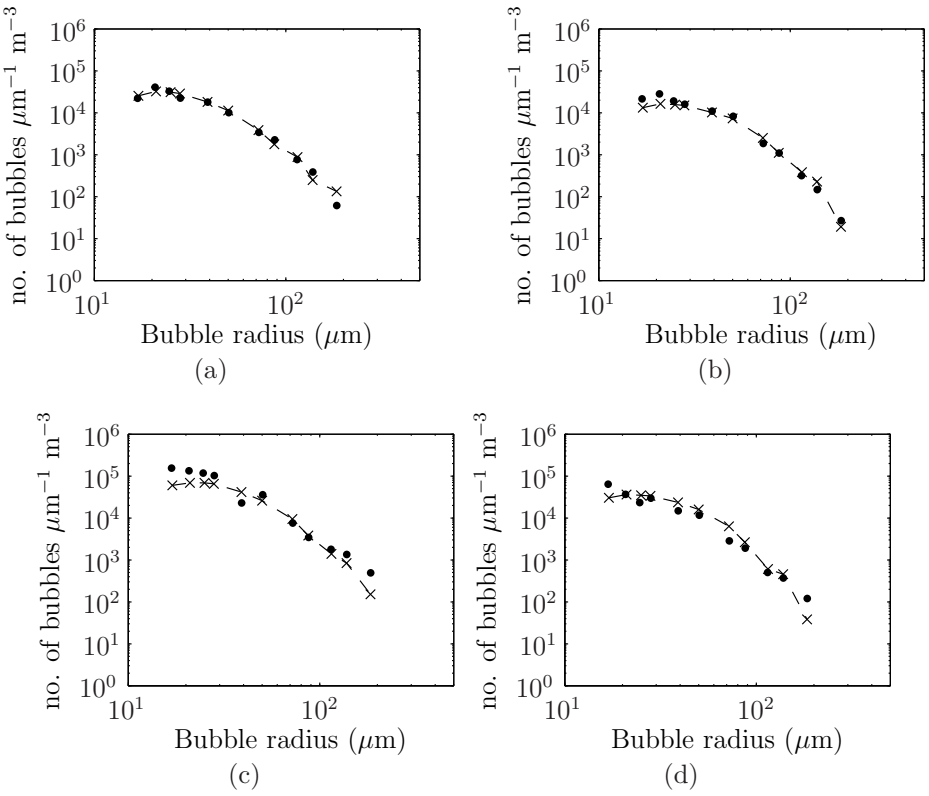

Figure 6.15: Best fits between the minimum and maximum bubble size distributions and the model results with scaled input populations. Panels (a) and (b) show the minimums and 1.15 m and 2 m depths respectively. Panels (c) and (d) show the maximums at 1.15 m and 2 m depths respectively. In each case, the black dots show the measurement uncertainty results and the dashed line shows the model results.

and a scaling up of 44% produced the best results for the maximum bubble size distributions.

6.5.3 Variation caused by rising significant wave height

The significant wave height, H_s, throughout the measurement period can be seen steadily rising in figure 5.21. This change in H_s presents an opportunity to assess what impact this makes on the gas flux. For this study, the data at 1.15 metres depth are examined in more detail. The data set is split into two parts - the first third with a mean H_s of 1.9 m and the rest of the data with a mean H_s of 3.1 m. The bubble size distributions are split into these two parts and the means are taken (shown in figure 6.16). These then represent the mean bubble size distributions at two different significant wave heights. The method found in section 6.5.2 can then be followed to find what scaling of the model bubble size distributions provides the best fit solutions. It was found that a scaling down of 45% for $H_s = 1.9$ m and a scaling up of 12% for $H_s = 3.1$ m gave the best fits. The resulting variation in the transfer velocity is shown in table 6.5.

6.5.4 Parameter sensitivity

When presenting results from a model such as this one, it is important to show the sensitivity of the model to different parameters. Figure 6.17 shows the change in the bubble size distribution when the "unknown" parameters are changed. Perturbation values were chosen as the minimum and maximum values used in the parameter study (see section 6.4.3). The change is shown at 1.15 m depth for each parameter except for the change in the breaking jet velocity since this had a significant effect on the relative magnitudes of the bubble size distributions at 1.15 and 2 metres depth. The turbulent diffusion coefficient is not shown as changing this variable did not significantly impact the bubble size distributions. This is because the Langmuir circulation plays a more dominant role in the distribution of the bubbles. As can be seen, the

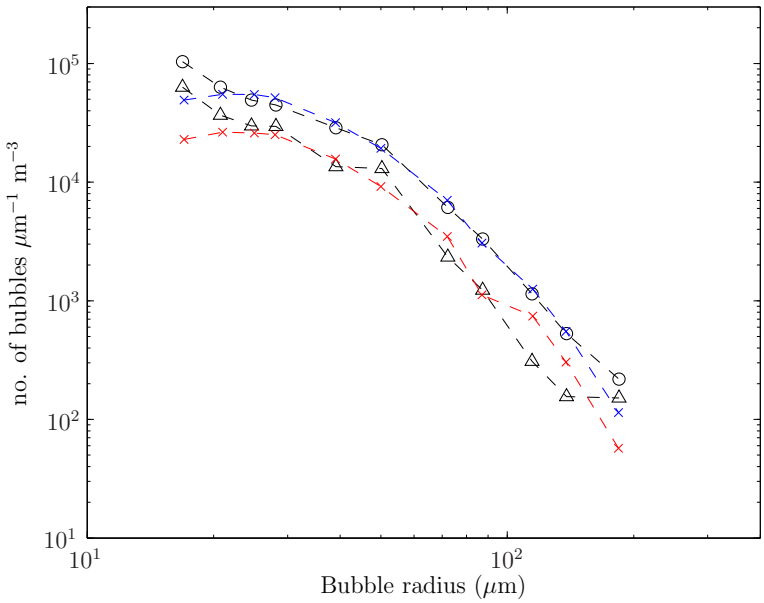

Figure 6.16: Bubble size distributions for mean significant wave heights of 3.1 m (circles) and 1.9 m (triangles). The best fits are shown in blue ($H_s = 3.1$ m) and red ($H_s = 1.9$ m).

model output is sensitive to each parameter. Therefore, if similar experiments are to be conducted in the future, effort should be made to incorporate measurements of these parameters where possible. It may also be advisable to examine the method of modelling the initial jet from the breaking wave.

6.5.5 Inference of gas flux

The main purpose of finding the best fit parameters is then to study the gas exchange associated with these bubble populations. As was explained earlier, the gas exchange between the atmosphere and ocean can be broken down into the direct transfer and the bubble mediated transfer. This is expressed by the equation [15]

$$F = K_o(C_w - C_a) + K_b[C_w - C_a(1 + \delta)], \tag{6.23}$$

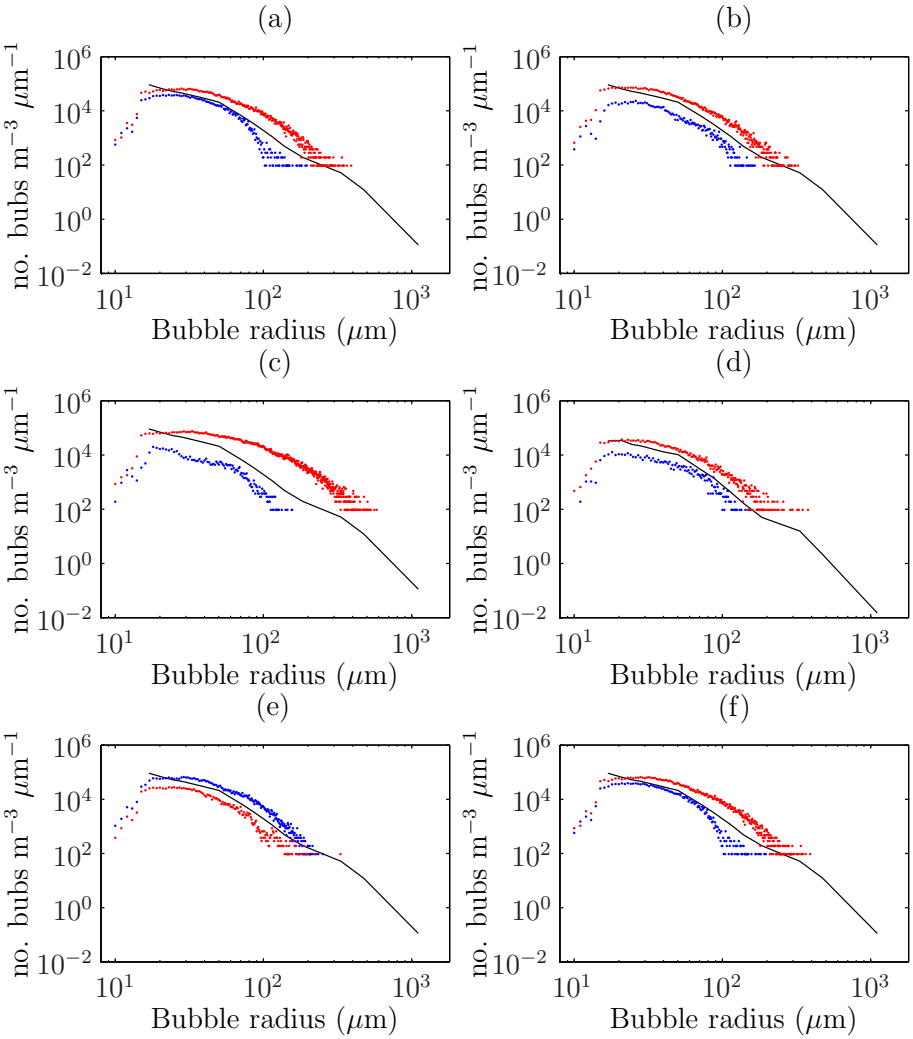

Figure 6.17: The sensitivity of the model output to varying parameters at 1.15 metres depth. In each subfigure, the solid line is the original best fit solution, the red dots represent an increase in each parameter and the blue dots represent a decrease in each parameter. Panel (a) shows the results from varying the maximum Langmuir velocity (0.1 and 0.25 m s^{-1}), panel (b) is the length of the initial jet (0.6 and 1.5 s), panels (c) and (d) are the initial jet velocity at 1.15 and 2 m respectively (0.2 and 1 m s^{-1}), panel (e) is the bubble insertion depth (0 and 0.15 m) and panel (f) is the time between breaking waves (5 and 15 s).

where F is the net air-sea flux, K_{o} is the direct transfer velocity, C_{w} is the concentration of each gas in the water, C_{a} is the concentration of each gas in air, K_{b} is the bubble mediated transfer velocity and δ is the equilibrium supersaturation. Equation (6.23) shows how the direct transfer of gas is driven by a concentration difference whereas the bubble mediated transfer is more complex. The important parameters for bubble mediated transfer are the transfer velocity, K_{b}, and the equilibrium supersaturation, δ [15], and any estimation of these parameters is of value. Woolf [15] attempts to constrain the range of values for the transfer velocity through a simplified bubble model. The model assumes that the bubble radius remains constant while gas is exchanged in and out of the bubble. Whilst this is reasonable for trace gases such as carbon dioxide, it invalidates the model for nitrogen and oxygen since a significant change in bubble radius is associated with these gas fluxes. However, it is possible to constrain values for carbon dioxide using this technique. In order to obtain a range of possible values, Woolf [15] estimates two different results based on hydrodynamically clean and dirty bubbles. By doing this, Woolf suggests that the global average for K_{b} is likely to be in the range of 2 to 10 cm h^{-1}. Woolf acknowledges that it is difficult to predict K_{b} through modelling alone which is a major strength of the results presented here, which are based on experimental data.

To obtain values for K_{b} and δ using the data from this thesis, the model is run using the set of parameters decided earlier. However, instead of running the model with a continuous input of bubbles until the cloud reaches a steady state, only a single input of bubbles is used and the model runs until all the bubbles have either surfaced or dissolved. The continuous input method mimics the observed conditions and serves to find the optimum parameters. The single input method then uses these parameters and gives the total gas flux associated with a specific input of bubbles. This enables the calculation of K_{b} and δ through repetition of the process, each time varying the saturation of each gas in the ocean. Figure 6.18 shows the results obtained using this method. Using the equation for the flux of gas out of the

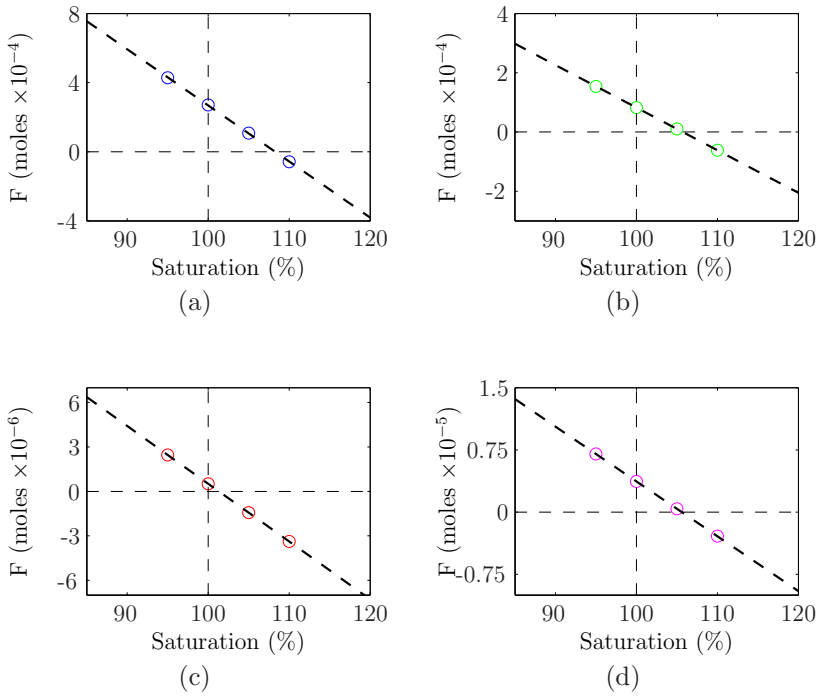

Figure 6.18: The flux of gas out of the bubbles and into the ocean from an input of bubbles as that in figure 6.4. Panel (a) shows the results for nitrogen, panel (b) shows the results for oxygen, panel (c) shows the results for carbon dioxide and panel (d) shows the results for argon. Each time, the saturation of the gas in question is varied and the resulting flux of that gas is plotted. The saturation is related to the concentration of a gas in the water through the equation $C_{\mathrm{w}} = S\, p_{\mathrm{p,w}}\, \phi_{\mathrm{sat}}$, where $p_{\mathrm{p,w}}$ is the partial pressure of a gas in water.

bubbles,

$$F_{\mathrm{b}} = K_{\mathrm{b}}[C_{\mathrm{w}} - Sp_{\mathrm{p}}(1+\delta)] \tag{6.24}$$

it is possible to extract values for K_{b} and δ from the x-axis intercept and the gradient. The equilibrium supersaturation is simply the x-intercept. The gradient is related to the transfer velocity through the equation

$$\text{gradient} = \frac{-K_{\mathrm{b}} S p_{\mathrm{p}}}{f_{\mathrm{fact}}} \tag{6.25}$$

where f_{fact} is a scaling factor to give a result equivalent to m^{-2} s^{-1}. The results shown in figure 6.18 also need to be scaled to represent more accurately the mean gas flux over the measurement period. In section 5.1.5 it is mentioned that only 198 of the 1800 measurements showed significant attenuation across a range of frequencies and were inverted to produce bubble size distributions and it is these distributions that the model is based on. Therefore, the flux values are multiplied by 198/1800 to give the mean flux over the entire measurement period. This assumes no contribution to the flux from any persistent band of bubbles that may exist at the surface. This is a valid assumption here for the following two reasons. Firstly, figure 5.31 shows very small bubble concentrations at the measurement depths. Secondly, figure 6.6 shows that for bubbles with small radii (which would be the case in a persistent band since large bubbles would rise quickly to the surface), the equilibration time is very low. Therefore the phase of active gas transfer would occur at the initial stage of a bubble plume rather than later in the bubbles' lives.

The resulting values for K_{b} and δ are presented in table 6.4. It is important to note that these values correspond to a mean wind speed of 14 m s^{-1}.

Uncertainty in the estimates of K_{b} are shown alongside the variation in K_{b} for different significant wave heights in table 6.5. The table shows a significant variation with H_{s} despite similar wind speeds for each dataset (13.7 m s^{-1} and 14.4 m s^{-1} respectively). This compliments the findings of Woolf [127], where he highlights the importance of the significant wave height as well as wind speed for the total gas transfer velocity.

The value for the transfer velocity of carbon dioxide can be compared with previous estimates made by Woolf [15]. Woolf presents an equation for the transfer velocity of carbon dioxide for dirty bubbles, given as

$$K_{\text{b}} = 2.63 \left(\frac{W_{\text{c}}}{0.01} \right) \text{cm h}^{-1}, \tag{6.26}$$

where W_c is the whitecap coverage given as [128]

$$W_c = 3.84 \times 10^{-6}(W_{10})^{3.41}. \tag{6.27}$$

Using a value of $W_{10} = 14$ m s^{-1} in equation (6.27), equation (6.26) produces a value of $K_b = 8.18$ cm h^{-1}, which is very close to the value found in this study. Further comparisons with historic estimates can be seen in table 6.4. The value of δ for carbon dioxide is higher than previous estimates although, according to Woolf [129], a large variation between instances of δ can be expected as a result of the variability of whitecapping at a single wind speed and the variability of the attenuation depth of bubble clouds. The value of K_b for oxygen predicted here is slightly higher that of Keeling [14]. Further experiments of this nature, undertaken in a range of wind speeds and significant wave heights, could provide excellent experimental support for results predicted through modelling alone.

6.6 Summary

A model of sub-surface bubble clouds and gas flux has been presented. Models were run until the bubble cloud reached steady state and the resulting bubble size distributions were compared with those measured in the Atlantic Ocean (figure 6.14). The model uses parameters taken from scientific constants, ancillary data taken on the D320 cruise and parameters found through trial and error. A set of parameters was found that produced a best fit between measured data and model results. This parameter set was then used to find values for the bubble mediated transfer velocity and equilibrium supersaturation (table 6.4).

Chapter 7 summarises the findings of this thesis and discusses the major conclusions.

	Transfer velocity, K_b, cm hr^{-1}	Equilibrium super-saturation, δ, %	Woolf & Thorpe '91 [55], δ	Woolf '93 [15], K_b	Keeling '93 [14], K_b	Keeling '93 [14], δ
Nitrogen	21.5	8.27	3.78	-	-	-
Oxygen	17.2	5.72	2.42	-	13.84	0.25
Carbon dioxide	8.1	1.32	0.0816	8.18	2.96	0.08 - 0.3
Argon	16.4	5.60	2.13	-	-	-

Table 6.4: Final values for the transfer velocity and equilibrium supersaturation resulting from the model based on measured data. Historic estimates from Woolf and Thorpe [55], Woolf [15] and Keeling [14] are also shown. All values are for a wind speed of 14 m s^{-1}.

	Measured K_b (cm hr^{-1})	Minimum K_b (cm hr^{-1})	Maximum K_b (cm hr^{-1})	K_b at $H_\mathrm{s} = 1.9$ m (cm hr^{-1})	K_b at $H_\mathrm{s} = 3.1$ m (cm hr^{-1})
Nitrogen	21.5	13.8	31.0	9.7	24.1
Oxygen	17.2	11.0	24.8	7.7	19.3
Carbon dioxide	8.1	5.2	11.7	3.7	9.1
Argon	16.39	10.5	23.6	7.4	18.4

Table 6.5: Variation in the transfer velocity for each gas owing to baseline uncertainty and change in significant wave height.

Chapter 7

Conclusions

This thesis has detailed acoustic experiments carried out on two sea trials as part of the DOGEE-SOLAS initiative. The purpose of the experiments was to measure sub-surface bubble populations in deep ocean alongside ancillary measurements such as the meteorological conditions and breaking wave intensity. These measurements add to historic data [9, 10, 26, 27, 29, 30] but also provide an accurate foundation for modelling gas flux between bubble clouds and the surrounding ocean.

The acoustic theory required for the experiments has been detailed in chapter 3. First, it is shown how attenuation can be predicted from a known bubble size distribution, which is the forward model. This is theory developed by Commander and Prosperetti [16]. It is then shown how this theory can be inverted to calculate bubble populations using attenuation measured at multiple frequencies. The mathematics involved in this are not trivial since the matrix to be inverted is ill-conditioned owing to the rising tail of the curves in the extinction cross section plots. A form of Tikhonov regularisation is used to optimise the problem and find an optimum bubble size distribution. Equations used in the calculation of volumetric backscatter strength, S_{v}, are then discussed, as is the relationship between S_{v} and bubble size distributions.

An 11 metre spar buoy was designed and built by scientists, engineers and

technicians at the National Oceanography Centre, Southampton (NOC). The buoy was designed with hydrodynamic damping in such a way that it would ride up and down with long period waves yet allow shorter period (i.e., breaking) waves to pass over it. The author developed an acoustic system, capable of measuring bubble populations and surface scatter, to be mounted on the buoy (see chapter 4). A capacitive wave wire system to measure wave height was developed by the team at NOC as well as a system of downward looking cameras to capture pictures of breaking waves as they cross the buoy. Under the supervision of Professor T. G. Leighton, student Ping-Chang Hsueh at the Institute of Sound and Vibration Research developed an optical fibre system to provide a second method of measuring sub-surface bubbles. The buoy is free floating and does not require any form of tethered cables. All systems onboard were fully autonomous and utilised timing systems to switch equipment on and off. This buoy is the first of its kind and performed very well, proving the concept of a free-floating, fully autonomous buoy, capable of measuring breaking waves and sub-surface bubble clouds.

The project was limited by a very restricted budget so that, for example, the number of channels and sensors was far less than would be desired. Also, the acoustic measurements of bubble size distributions reported in this thesis were not of the highest priority in the cruise, with the acoustic equipment broadening the capability of a spar buoy designed primarily for other sensors. This restricted the opportunity to make calibration measurements and also to remove buoy structure from the acoustic path.

Unfortunately, there was no single period of time that all of the different systems measured data simultaneously owing to problems with the wave wire logging system, a leak in the optical system housing on the second cruise, D320, and calm weather conditions for many of the other deployments. However, on the second deployment of D320, two sets of acoustic data were measured successfully. The first used an array of hydrophones to measure attenuation over a range of frequencies, 3-197 kHz. A large number of bubble size distributions were measured at two depths, which give a solid picture

of the bubble size distributions found under breaking waves and agree well with historic measurements. Acoustic data was also taken using an inverted echo sounder. This transmitted 160 kHz pulses towards the sea surface from the bottom of the buoy and measured the reflected signals. These waveforms could then be transformed into volumetric backscatter strength and give a profile of the bubble clouds as they were advected across the buoy. There is, however, a very limited amount of inverted echo sounder data because of hardware malfunctions. The data that the system did take was in a period of relatively infrequent breaking waves. Therefore the backscatter strengths are relatively low when compared to more notable measurements [42, 130].

The theory detailed in chapter 3 is used to relate the two sets of data and the attenuation data is used to calibrate the previously uncalibrated inverted echo sounder data. Once this calibration has been carried out, the mean value of S_{v} can be calculated and used to scale the bubble size distributions with depth, giving far more information about the sub-surface bubble clouds. At present there are some limitations in this method since attenuation of the acoustic signal is not accounted for. There are techniques to incorporate this effect [101] but this was deemed beyond the scope of this PhD.

A model for the evolution of bubble clouds and the associated gas flux was developed to incorporate ancillary data measured on the D320 cruise. Parameters within the model were then adjusted to produce a resultant bubble population that matched the measurements made by the acoustic attenuation system. This forms a set of parameters based on measurements made in the open ocean. These are then used to find the gas flux associated with breaking waves in the measured conditions and comparisons are drawn with previous estimates. Values for the bubble mediated transfer velocity, K_{b}, and the equilibrium supersaturation, δ, are presented for nitrogen, oxygen, carbon dioxide and argon. This represents the first time that these parameters have been estimated from experimental work and forms a key role in improving our understanding of air-sea gas transfer. Furthermore, owing to the variation in significant wave height throughout the measurement period,

it was possible to calculate gas transfer velocities for two different values of significant wave height.

This thesis reports success in both open ocean measurements and also gas flux modelling, linking the two to provide an insightful estimate of bubble-mediated gas flux between the atmosphere and the ocean.

Appendices

Appendix A

Derivation of scattering and backscattering cross sections

The difference of 4π between the scattering and backscattering cross sections arises from the definitions of each of them. Foldy [82] presents a method for deriving the scattering cross section and Medwin and Clay [81] present a definition for the backscattering cross section.

A.1 Scattering cross section

The scattering cross section is derived by considering a single scatterer with a plane incident wave defined by

$$\psi_0(\mathbf{r}) = A_1 \exp[-i\mathbf{k}_0 \cdot \mathbf{r}], \tag{A.1}$$

where A_1 is the amplitude, $\mathbf{k}_0$ is the wavenumber and $\mathbf{r}$ is the observer position. When a single scatterer is introduced, the field becomes

$$\psi(\mathbf{r}) = \psi_0(\mathbf{r}) + g_1\psi_0(\mathbf{r}_1)\frac{\mathrm{e}^{-i\mathbf{k}_0|\mathbf{r}-\mathbf{r}_1|}}{|\mathbf{r}-\mathbf{r}_1|}, \tag{A.2}$$

where g_1 is the scattering strength. A value proportional to the energy flux per unit area in the scattered field is given by

$$\mathcal{F} = \psi_{\rm s}^* \nabla \psi_{\rm s} - \psi_{\rm s} \nabla \psi_{\rm s}^*, \tag{A.3}$$

where $\psi_{\rm s}$ is the second term on the right hand side of equation (A.2). Using the definition

$$E(\mathbf{r}, \mathbf{r}_1) = \frac{{\rm e}^{-i\mathbf{k}_0|\mathbf{r}-\mathbf{r}_1|}}{|\mathbf{r}-\mathbf{r}_1|}, \tag{A.4}$$

the components of equation (A.3) become

$$\begin{aligned}
\psi_{\rm s}^* &= g_1^* \psi_0^* E^*(\mathbf{r}, \mathbf{r}_1) && \text{(A.5)}\\
\nabla\psi_{\rm s} &= g_1 \psi_0(\mathbf{r}_1) \nabla E(\mathbf{r}, \mathbf{r}_1) && \text{(A.6)}\\
\psi_{\rm s} &= g_1 \psi_0 E(\mathbf{r}, \mathbf{r}_1) && \text{(A.7)}\\
\nabla\psi_{\rm s}^* &= g_1^* \psi_0^*(\mathbf{r}_1) \nabla E^*(\mathbf{r}, \mathbf{r}_1). && \text{(A.8)}
\end{aligned}$$

Using equations (A.5) to (A.8), equation (A.3) becomes

$$\begin{aligned}
\mathcal{F} &= g_1^* \psi_0^* E^* g_1 \psi_0(\mathbf{r}_1) \nabla E - g_1 \psi_0 E g_1^* \psi_0^*(\mathbf{r}_1) \nabla E^* \\
&= g_1 g_1^* \psi_0(\mathbf{r}_1) \psi_0^*(\mathbf{r}_1) [E^* \nabla E - E \nabla E^*]. && \text{(A.9)}
\end{aligned}$$

Since

$$\begin{aligned}
\psi_0(\mathbf{r}_1)\psi_0^*(\mathbf{r}_1) &= A_1\, {\rm e}^{-i\mathbf{k}_0\cdot\mathbf{r}} A_1^*\, {\rm e}^{+i\mathbf{k}_0\cdot\mathbf{r}} \\
&= A_1\, A_1^* \\
&= |A_1|^2, && \text{(A.10)}
\end{aligned}$$

the flux per unit area becomes

$$\mathcal{F} = |g_1|^2 |A_1|^2 [E^* \nabla E - E \nabla E^*]. \tag{A.11}$$

Since

$$\nabla E = \left(\frac{-1}{R}\right)\left(\frac{1}{R} + ik_0\right)(\mathbf{r} - \mathbf{r}_1)E, \tag{A.12}$$

and

$$\nabla E^* = \left(\frac{-1}{R}\right)\left(\frac{1}{R} - ik_0\right)(\mathbf{r} - \mathbf{r}_1)E^*, \tag{A.13}$$

where $R = |\mathbf{r} - \mathbf{r}_1|$,

$$\begin{aligned} E^*\nabla E - E\nabla E^* &= \frac{\mathrm{e}^{ik_0R}}{R}\frac{\mathrm{e}^{-ik_0R}}{R}\left(\frac{-1}{R}\right)\left(\frac{1}{R} + ik_0\right)(\mathbf{r} - \mathbf{r}_1)\ldots \\ &\quad \ldots - \frac{\mathrm{e}^{-ik_0R}}{R}\frac{\mathrm{e}^{ik_0R}}{R}\left(\frac{-1}{R}\right)\left(\frac{1}{R} - ik_0\right)(\mathbf{r} - \mathbf{r}_1) \\ &= \left[\frac{1}{R^2}\left(\frac{-1}{R}\right)\left(\frac{1}{R} + ik_0\right)\ldots\right. \\ &\quad \left.\ldots - \frac{1}{R^2}\left(\frac{-1}{R}\right)\left(\frac{1}{R} - ik_0\right)\right](\mathbf{r} - \mathbf{r}_1) \\ &= \left[\frac{-1}{R^4} - \frac{ik_0}{R^3} + \frac{1}{R^4} - \frac{ik_0}{R^3}\right](\mathbf{r} - \mathbf{r}_1) \\ &= -\frac{2ik_0}{R^3}(\mathbf{r} - \mathbf{r}_1). \end{aligned} \tag{A.14}$$

Using equation (A.14), the flux per unit area becomes

$$\begin{aligned} \mathcal{F} &= -|g_1|^2|A_1|^2\frac{2ik_0}{R^3}(\mathbf{r} - \mathbf{r}_1) \\ &= -|g_1|^2|A_1|^2\frac{2ik_0}{R^3}R\,\mathbf{e}_\mathrm{r}, \end{aligned} \tag{A.15}$$

where

$$\mathbf{e}_\mathrm{r} = \frac{(\mathbf{r} - \mathbf{r}_1)}{|\mathbf{r} - \mathbf{r}_1|}. \tag{A.16}$$

In order to find the total flux, equation (A.15) is integrated over a sphere (with surface area = A_s) whose centre is at the position of the scatterer,

which gives

$$\begin{aligned}
\mathcal{F}_{\text{tot}} &= \iint_{A_\text{s}} |\mathcal{F}|\, R^2 \sin\theta \, \mathrm{d}\theta\mathrm{d}\phi \\
&= \iint_{A_\text{s}} -2ik_0|g_1|^2|A_1|^2 \frac{1}{R^2} R^2 \sin\theta \, \mathrm{d}\theta\mathrm{d}\phi \\
&= ik_0|g_1|^2|A_1|^2(-2) \iint_{A_\text{s}} \sin\theta \, \mathrm{d}\theta\mathrm{d}\phi \\
&= 4\pi ik_0|g_1|^2|A_1|^2 \times (-2). \qquad \text{(A.17)}
\end{aligned}$$

It can be seen that the 4π arises from the integration over the area of the sphere, since the scattered wave is spherical.

The scattering cross section is defined as the ratio of time-averaged power loss due to scattering to the intensity of the incident acoustic beam. It is therefore necessary to calculate the flux per unit area in the incident wave, given by

$$\mathcal{F}_0 = \psi_0^* \nabla\psi_0 - \psi_0 \nabla\psi_0^*, \qquad \text{(A.18)}$$

the components of which are

$$\begin{aligned}
\psi_0^* &= A_1^* \mathrm{e}^{i\mathbf{k}_0\cdot\mathbf{r}} && \text{(A.19)} \\
\nabla\psi_0 &= -i\mathbf{k}_0 A_1^* \mathrm{e}^{-i\mathbf{k}_0\cdot\mathbf{r}} && \text{(A.20)} \\
\psi_0 &= A_1^* \mathrm{e}^{-i\mathbf{k}_0\cdot\mathbf{r}} && \text{(A.21)} \\
\nabla\psi_0^* &= i\mathbf{k}_0 A_1^* \mathrm{e}^{i\mathbf{k}_0\cdot\mathbf{r}}. && \text{(A.22)}
\end{aligned}$$

This leads to

$$\begin{aligned}
\mathcal{F}_0 &= A_1^* \mathrm{e}^{i\mathbf{k}_0\cdot\mathbf{r}}(-i\mathbf{k}_0 A_1^* \mathrm{e}^{-i\mathbf{k}_0\cdot\mathbf{r}}) - A_1^* \mathrm{e}^{-i\mathbf{k}_0\cdot\mathbf{r}}(i\mathbf{k}_0 A_1^* \mathrm{e}^{i\mathbf{k}_0\cdot\mathbf{r}}) \\
&= -i\mathbf{k}_0 A_1 \, A_1^* - i\mathbf{k}_0 A_1 \, A_1^* \\
&= -2i\mathbf{k}_0 |A_1|^2. \qquad \text{(A.23)}
\end{aligned}$$

Let $\mathbf{k}_0 = k_0 \mathbf{e}_\text{k}$, where $\mathbf{e}_\text{k}$ is a unit vector in the direction of propagation.

Integrating over unit area gives

$$\begin{aligned}\mathcal{F}_{0,\text{tot}} &= \iint_{A_0} (-2ik_0)|A_1|^2 \,\mathrm{d}A_1 \\ &= -2ik_0|A_1|^2. \end{aligned} \tag{A.24}$$

The scattering cross section can now be shown by dividing equation (A.17) by equation (A.24) to give

$$\begin{aligned}\Omega_{\text{scat}} &= \frac{4\pi ik_0|g_1|^2|A_1|^2 \times (-2)}{ik_0|A_1|^2 \times (-2)} \\ &= 4\pi|g_1|^2. \end{aligned} \tag{A.25}$$

This assumes omnidirectional scattering, i.e., g_1 is constant.

A.2 Backscattering cross section

In order to compare the scattering cross section to the backscattering cross section, it is important to look at the case where the scattering is not omnidirectional, i.e., the scattering strength depends on the solid angle, giving $g_1(\theta, \phi, f)$. In this case we have

$$\psi_0 = A_1 \exp^{-i\mathbf{k}_0 \cdot \mathbf{r}}, \tag{A.26}$$

and

$$\psi_\text{s} = g_1(\theta, \phi, f)\psi_0(\mathbf{r}_1)E(\mathbf{r}, \mathbf{r}_1). \tag{A.27}$$

This leads to

$$|\psi_0| = |A_1|, \tag{A.28}$$

and

$$\begin{aligned}|\psi_\text{s}| &= |g_1(\theta, \phi, f)|\,|\psi_0|\,|E| \\ &= |g_1(\theta, \phi, f)|\,|A_1|\,\frac{1}{R}. \end{aligned} \tag{A.29}$$

Thus

$$|g_1(\theta, \phi, f)| = \frac{R\,|\psi_\mathrm{s}|}{|\psi_0|} \tag{A.30}$$

Clay and Medwin [83] define the backscattering cross section as

$$\Omega_{\mathrm{b-s}} = \left(\frac{P_{\mathrm{b-s}}}{P_{\mathrm{pi}}}\right)^2 R^2, \tag{A.31}$$

where $P_{\mathrm{b-s}}$ is the backscattered pressure at the receiver and P_{pi} is the pressure of the incident wave at the receiver. From equations (A.30) and (A.31) it can be seen that the non-omnidirectional backscattering cross section is given by

$$\Omega_{\mathrm{b-s}}(\theta, \phi, f) = |g_1(\theta, \phi, f)|^2 = \frac{R^2|\psi_\mathrm{s}|^2}{|\psi_0|^2}. \tag{A.32}$$

Since scattering from bubbles can be considered omnidirectional [131, 132], g_1 is constant giving

$$\Omega_{\mathrm{b-s}} = |g_1|^2. \tag{A.33}$$

Now from equations (A.25) and (A.33) it can easily be seen that

$$\Omega_{\mathrm{b-s}} = \frac{\Omega_{\mathrm{scat}}}{4\pi}. \tag{A.34}$$

Bibliography

[1] P. Falkowski, R. J. Scholes, E. Boyle, J. Canadell, D. Canfield, J. Elser, N. Gruber, K. Hibbard, P. Hogberg, S. Linder, F. T. Mackenzie, B. Moore, T. Pedersen, Y. Rosenthal, S. Seitzinger, V. Smetacek, and W. Steffen. The global carbon cycle: A test of our knowledge of Earth as a system. *Science*, 290(5490):291–296, 2000.

[2] U. Siegenthaler and J. L. Sarmiento. Atmospheric carbon-dioxide and the ocean. *Nature*, 365(6442):119–125, 1993.

[3] M. Stuiver. Atmospheric carbon-dioxide and carbon reservoir changes. *Science*, 199(4326):253–258, 1978.

[4] P. P. Tans, I. Y. Fung, and T. Takahashi. Observational constraints on the global atmospheric CO_2 budget. *Science*, 247(4949):1431–1438, 1990.

[5] P. S. Liss and L. Merlivat. Air-sea gas exchange rates: introduction and synthesis. In P. Buat-Ménard, editor, *The role of air-sea exchange in geochemical cycling*, pages 113–128. D.Reidel Publishing Company, Dordrecht, Holland, 1986.

[6] D. W. R. Wallace and C. D. Wirick. Large air sea gas fluxes associated with breaking waves. *Nature*, 356(6371):694–696, 1992.

[7] D. M. Farmer, C. L. McNeil, and B. D. Johnson. Evidence for the importance of bubbles in increasing air sea gas flux. *Nature*, 361(6413):620–623, 1993.

[8] T. G. Leighton, S. D. Meers, and P. R. White. Propagation through nonlinear time-dependent bubble clouds and the estimation of bubble populations from measured acoustic characteristics. *Proceedings of the Royal Society of London, Series A (Mathematical, Physical and Engineering Sciences)*, 460(2049):2521–2550, 2004.

[9] N. Breitz and H. Medwin. Instrumentation for insitu acoustical measurements of bubble spectra under breaking waves. *Journal of the Acoustical Society of America*, 86(2):739–743, 1989.

[10] B. D. Johnson and R. C. Cooke. Bubble populations and spectra in coastal waters - photographic approach. *Journal of Geophysical Research-Oceans and Atmospheres*, 84(NC7):3761–3766, 1979.

[11] A. L. Walsh and P. J. Mulhearn. Photographic measurements of bubble populations from breaking wind-waves at sea. *Journal of Geophysical Research-Oceans*, 92(C13):14553–14565, 1987.

[12] G. Rojas and M. R. Loewen. Fiber-optic probe measurements of void fraction and bubble size distributions beneath breaking waves. *Experiments in Fluids*, 43(6):895–906, 2007.

[13] I. M. Brooks, M. J. Yelland, R. C. Upstill-Goddard, P. D. Nightingale, S. Archer, E. d'Asaro, R. Beale, C. Beatty, B. Blomquist, A. A. Bloom, B. J. Brooks, J. Cluderay, D. G. H. Coles, J. Dacey, M. DeGrandpre, J. Dixon, W. M. Drennan, J. Gabriele, L. Goldson, N. Hardman-Mountford, M. K. Hill, M. Horn, P. C. Hsueh, B. Huebert, G. de Leeuw, T. G. Leighton, M. Liddicoat, J. J. N. Lingard, C. McNeil, J. B. McQuaid, B. I. Moat, G. Moore, C. Neill, S. J. Norris, S. O'Doherty, R. W. Pascal, J. Prytherch, M. Rebozo, E. Sahlee, M. Salter, U. Schuster, I. Skjelvan, H. Slagter, M. H. Smith, P. D. Smith, M. Srokosz, J. A. Stephens, P. K. Taylor, M. Telszewski, R. Walsh, B. Ward, D. K. Woolf, D. Young, and H. Zemmelink. Physical exchanges at the air–

sea interface: UK-SOLAS field measurements. *Bulletin of the American Meteorological Society*, 90:629–644, 2009.

[14] R. F. Keeling. On the role of large bubbles in air-sea gas-exchange and supersaturation in the ocean. *Journal of Marine Research*, 51(2):237–271, 1993.

[15] D. K. Woolf. Bubbles and the air-sea transfer velocity of gases. *Atmosphere-Ocean*, 31(4):517–540, 1993.

[16] K. W. Commander and A. Prosperetti. Linear pressure waves in bubbly liquids - comparison between theory and experiments. *Journal of the Acoustical Society of America*, 85(2):732–746, 1989.

[17] J. B. Keller and I. I. Kolodner. Damping of underwater explosion bubble oscillations. *Journal of Applied Physics*, 27:1152–1161, 1956.

[18] J. B. Keller and M. Miksis. Bubble oscillations of large-amplitude. *Journal of the Acoustical Society of America*, 68(2):628–633, 1980.

[19] R. Duraiswami, S. Prabhukumar, and G. L. Chahine. Bubble counting using an inverse acoustic scattering method. *Journal of the Acoustical Society of America*, 104(5):2699–2717, 1998.

[20] E.J. Terrill and W.K. Melville. A broadband acoustic technique for measuring bubble size distributions: Laboratory and shallow water measurements. *Journal of Atmospheric and Oceanic Technology*, 17(2):220–239, 2000.

[21] W. K. Melville, E. Terrill, and F. Veron. Bubbles and turbulence under breaking waves. *Natural Physical Processes Associated with Sea Surface Sound*, pages 135–145, 1997.

[22] E. J. Terrill, G. Lada, and W. K. Melville. Surf zone bubble populations. In T. G. Leighton, G. J. Heald, H. Griffiths, and G. Griffiths,

editors, *Acoustical Oceanography*, volume 23 of *Proceedings of the Institute of Acoustics*, pages 212–219. Bath University Press, 2001.

[23] K. W. Commander and R. J. Mcdonald. Finite-element solution of the inverse problem in bubble swarm acoustics. *Journal of the Acoustical Society of America*, 89(2):592–597, 1991.

[24] P. C. Hansen. Numerical Tools for Analysis and Solution of Fredholm Integral-Equations of the 1st Kind. *Inverse Problems*, 8(6):849–872, 1992.

[25] P.C. Hansen. *Rank-deficient and discrete ill-posed problems: numerical aspects of linear inversion.* Society for Industrial Mathematics, Philadelphia, PA, 1998.

[26] G. B. Deane and M. D. Stokes. Air entrainment processes and bubble size distributions in the surf zone. *Journal of Physical Oceanography*, 29(7):1393–1403, 1999.

[27] A. D. Phelps, D. G. Ramble, and T. G. Leighton. The use of a combination frequency technique to measure the surf zone bubble population. *Journal of the Acoustical Society of America*, 101(4):1981–1989, 1997.

[28] S. D. Meers, T. G. Leighton, J. W. L. Clarke, G. J. Heald, H. A. Dumbrell, and P. R. White. The importance of bubble ring-up and pulse length in estimating the bubble distribution from propagation measurements. In T. G. Leighton, G. J. Heald, H. Griffiths, and G. Griffiths, editors, *Acoustical Oceanography*, volume 23 of *Proceedings of the Institute of Acoustics*, pages 235–241. Bath University Press, 2001.

[29] D. M. Farmer and S. Vagle. Waveguide propagation of ambient sound in the ocean-surface bubble layer. *Journal of the Acoustical Society of America*, 86(5):1897–1908, 1989.

[30] A.D. Phelps and T.G. Leighton. Oceanic bubble population measurements using a buoy-deployed combination frequency technique. *IEEE Journal of Oceanic Engineering*, 23(4):400–410, 1998.

[31] D. G. H. Coles and T. G. Leighton. Autonomous spar-buoy measurements of bubble populations under breaking waves in the sea of the hebrides. In *Underwater Acoustic Measurements: Technologies & Results*, pages 543–548, Crete, Greece, 2007.

[32] S. Baldy. Bubbles in the close vicinity of breaking waves - statistical characteristics of the generation and dispersion mechanism. *Journal of Geophysical Research-Oceans*, 93(C7):8239–8248, 1988.

[33] D. M. Farmer, S. Vagle, and A. D. Booth. A free-flooding acoustical resonator for measurement of bubble size distributions. *Journal of Atmospheric and Oceanic Technology*, 15(5):1132–1146, 1998.

[34] S. Vagle and D. M. Farmer. A comparison of four methods for bubble size and void fraction measurements. *IEEE Journal of Oceanic Engineering*, 23(3):211–222, 1998.

[35] D. M. Farmer, S. Vagle, and D. Booth. Reverberation effects in acoustical resonators used for bubble measurements. *Journal of the Acoustical Society of America*, 118(5):2954–2960, 2005.

[36] T. G. Leighton, D. G. Ramble, A. D. Phelps, C. L. Morfey, and P. P. Harris. Acoustic detection of gas bubbles in a pipe. *Acustica*, 84(5):801–814, 1998.

[37] T. G. Leighton, P. R. White, C. L. Morfey, J. W. L. Clarke, G. J. Heald, H. A. Dumbrell, and K. R. Holland. The effect of reverberation on the damping of bubbles. *Journal of the Acoustical Society of America*, 112(4):1366–1376, 2002.

[38] V. L. Newhouse and P. M. Shankar. Bubble-size measurements using the nonlinear mixing of 2 frequencies. *Journal of the Acoustical Society of America*, 75(5):1473–1477, 1984.

[39] J. Y. Chapelon, P. M. Shankar, and V. L. Newhouse. Ultrasonic measurement of bubble cloud size profiles. *Journal of the Acoustical Society of America*, 78(1):196–201, 1985.

[40] P. M. Shankar, J. Y. Chapelon, and V. L. Newhouse. Fluid pressure measurement using bubbles insonified by two frequencies. *Ultrasonics*, 24:333–336, 1986.

[41] D. Koller, Y. Li, P. M. Shankar, and V. L. Newhouse. High-speed bubble sizing using the double frequency technique for oceanographic applications. *IEEE Journal of Oceanic Engineering*, 17(3):288–291, 1992.

[42] M. V. Trevorrow. Measurements of near-surface bubble plumes in the open ocean with implications for high-frequency sonar performance. *Journal of the Acoustical Society of America*, 114(5):2672–2684, 2003.

[43] M. V. Hall. A comprehensive model of wind-generated bubbles in the ocean and predictions of the effects on sound-propagation at frequencies up to 40 Khz. *Journal of the Acoustical Society of America*, 86(3):1103–1117, 1989.

[44] P. H. Dahl. The contribution of bubbles to high-frequency sea surface backscatter: A 24-h time series of field measurements. *Journal of the Acoustical Society of America*, 113(2):769–780, 2003.

[45] P. H. Dahl, W. J. Plant, B. Nutzel, A. Schmidt, H. Herwig, and E. A. Terray. Simultaneous acoustic and microwave backscattering from the sea surface. *Journal of the Acoustical Society of America*, 101(5):2583–2595, 1997.

[46] P. S. Liss. Gas transfer: experiments and geochemical implications. *Air-sea exchange of gases and particles*, pages 241–298, 1983.

[47] B. Jähne, K. O. Münnich, R. Bosinger, A. Dutzi, W. Huber, and P. Libner. On the parameters influencing air-water gas exchange. *Journal of Geophysical Research*, 92(C2):1937–1949, 1987.

[48] P. D. Nightingale, G. Malin, C. S. Law, A. J. Watson, P. S. Liss, M. I. Liddicoat, J. Boutin, and R. C. Upstill-Goddard. In situ evaluation of air-sea gas exchange parameterizations using novel conservative and volatile tracers. *Global Biogeochemical Cycles*, 14(1):373–387, 2000.

[49] R. Wanninkhof and W. R. McGillis. A cubic relationship between air-sea CO_2 exchange and wind speed. *Geophysical Research Letters*, 26(13):1889–1892, 1999.

[50] R. Wanninkhof. Relationship between wind speed and gas exchange over the ocean. *Journal of Geophysical Research-Oceans*, 97(C5):7373–7382, 1992.

[51] R. Wanninkhof, K. F. Sullivan, and Z. Top. Air-sea gas transfer in the Southern Ocean. *Journal of Geophysical Research-Oceans*, 109(C8):C08S19, 2004.

[52] E. J. Bock, T. Hara, N. M. Frew, and W. R. McGillis. Relationship between air-sea gas transfer and short wind waves. *Journal of Geophysical Research-Oceans*, 104(C11):821–825, 1999.

[53] B. Jähne and E. C. Monahan, editors. *Measurement of gas transfer, whitecap coverage, and brightness temperature in a surf pool: An overview of WABEX-93*, Air-Water Gas Transfer: Selected Papers from the Third International Symposium on Air-Water Gas Transfer. AEON Verlag and Studio, 1995.

[54] L. Merlivat and L. Memery. Gas exchange across an air-water interface: experimental results and modeling of bubble contribution to transfer. *Journal of Geophysical Research*, 88(C1):707–724, 1983.

[55] D. K. Woolf and S. A. Thorpe. Bubbles and the air-sea exchange of gases in near-saturation conditions. *Journal of Marine Research*, 49(3):435–466, 1991.

[56] H. C. Broecker, J. Petermann, and W. Siems. The influence of wind on CO_2 exchange in a wind-wave tunnel, including the effects of monolayers. *Journal of Marine Research*, 36:595–610, 1978.

[57] B. Jähne and KO Münnich. Measurements of gas exchange and momentum transfer in a circular wind-water tunnel. *Tellus*, 31:329, 1979.

[58] P. S. Liss, P. W. Balls, F. N. Martinelli, and M. Coantic. The effect of evaporation and condensation on gas transfer across an air-water interface. *Oceanol. Acta*, 4:129–138, 1981.

[59] L. Memery and L. Merlivat. Modeling of gas flux through bubbles at the air-water-interface. *Tellus Series B-Chemical and Physical Meteorology*, 37(4-5):272–285, 1985.

[60] T. Takahashi, R. A. Feely, R. F. Weiss, R. H. Wanninkhof, D. W. Chipman, S. C. Sutherland, and T. T. Takahashi. Global air-sea flux of CO_2: An estimate based on measurements of sea-air pCO_2 difference. *Proceedings of the National Academy of Sciences*, 94(16):8292–8299, 1997.

[61] A. Graham. Aeration due to breaking waves. Part II: Fluxes. *Journal of Physical Oceanography*, 34(5):1008–1018, 2004.

[62] S. A. Thorpe. A model of the turbulent diffusion of bubbles below the sea-surface. *Journal of Physical Oceanography*, 14(5):841–854, 1984.

[63] S. A. Thorpe. On the clouds of bubbles formed by breaking wind-waves in deep water, and their role in air-sea gas transfer. *Philosophical Transactions of the Royal Society of London A (Mathematical and Physical Sciences)*, 304(1483):155–210, 1982.

[64] S. A. Thorpe. The effect of langmuir circulation on the distribution of submerged bubbles caused by breaking wind-waves. *Journal of Fluid Mechanics*, 142(MAY):151–169, 1984.

[65] T. G. Leighton. *The Acoustic Bubble*. Academic Press, London, 1994.

[66] T. G. Leighton. Acoustic bubble detection - I: The detection of stable gas bodies. *Environmental Engineering*, 7(3):9–16, 1994.

[67] T. G. Leighton. From seas to surgeries, from babbling brooks to baby scans: The acoustics of gas bubbles in liquids. *International Journal of Modern Physics B*, 18(25):3267–3314, 2004.

[68] T.G. Leighton. What is ultrasound? *Progress in Biophysics and Molecular Biology*, 93(1-3):3–83, 2007.

[69] T. G. Leighton, A. D. Phelps, D. G. Ramble, and D. A. Sharpe. Comparison of the abilities of eight acoustic techniques to detect and size a single bubble. *Ultrasonics*, 34(6):661–667, 1996.

[70] T. G. Leighton, D. G. Ramble, and A. D. Phelps. The detection of tethered and rising bubbles using multiple acoustic techniques. *Journal of the Acoustical Society of America*, 101(5):2626–2635, 1997.

[71] T. G. Leighton and G. B. N. Robb. Preliminary mapping of void fractions and sound speeds in gassy marine sediments from subbottom profiles. *Journal of the Acoustical Society of America*, 124(5):EL313–EL320, 2008.

[72] A. O. Maksimov and T. G. Leighton. Transient processes near the acoustic threshold of parametrically-driven bubble shape oscillations. *Acta Acustica*, 87(3):322–332, 2001.

[73] A. D. Phelps and T. G. Leighton. High-resolution bubble sizing through detection of the subharmonic response with a two-frequency excitation technique. *Journal of the Acoustical Society of America*, 99(4):1985–1992, 1996.

[74] A. D. Phelps and T. G. Leighton. The subharmonic oscillations and combination-frequency subharmonic emissions from a resonant bubble: Their properties and generation mechanisms. *Acta Acustica*, 83(1):59–66, 1997.

[75] D. G. Ramble, A. D. Phelps, and T. G. Leighton. On the relation between surface waves on a bubble and the subharmonic combination-frequency emission. *Acustica*, 84(5):986–988, 1998.

[76] T. G. Leighton and G. J. Heald. Very high frequency coastal acoustics. In H. Medwin, editor, *Acoustical Oceanography: Sound in the Sea*, pages 518–547. Cambridge University Press, New York, 2005.

[77] M. A. Ainslie and T. G. Leighton. Near resonant bubble acoustic cross-section corrections, including examples from oceanography, volcanology, and biomedical ultrasound. *Journal of the Acoustical Society of America*, (in press), 2009.

[78] I. B. Andreeva. Scattering of sound by air bladders of fish in deep sound-scattering ocean layers. *Sov. Phys. Acoust*, 10(1):17–20, 1964.

[79] D. E. Weston. Sound propagation in the presence of bladder fish. In *Underwater Acoustics: Proceedings of an Institute at the Imperial College of Science and Technology of the University of London, July 31-August 11, 1961*, page 55. Pennsylvania State University; distributed by Plenum Press, New York, 1963.

[80] A. N. Tikhonov and V. Y. Arsenin. *Solution of ill-posed problems*. Wiley, New York, 1977.

[81] H. Medwin and C. S. Clay. *Fundamentals of acoustical oceanography*. Applications of modern acoustics. Academic Press, Boston, 1998.

[82] L. L. Foldy. The multiple scattering of waves. I. General theory of isotropic scattering by randomly distributed scatterers. *Physical Review*, 67(3-4):107–119, 1945.

[83] C. S. Clay and H. Medwin. *Acoustical Oceanography: Principals and Applications*. Wiley, New York, 1977.

[84] T. G. Leighton, S. D. Meers, M. D. Simpson, Clarke, J. W. L., G. T. Yim, P. R. Birkin, Y. E. Watson, P. R. White, G. J. Heald, H. A. Dumbrell, R. L. Culver, and S. D. Richards. The Hurst Spit experiment: The characterisation of bubbles in the surf zone using multiple acoustic techniques. In T. G. Leighton, G. J. Heald, H. Griffiths, and G. Griffiths, editors, *Acoustical Oceanography*, volume 23 of *Proceedings of the Institute of Acoustics*, pages 227–234. Bath University Press, 2001.

[85] J. W. L. Clarke and T. G. Leighton. A method for estimating time-dependent acoustic cross-sections of bubbles and bubble clouds prior to the steady state. *Journal of the Acoustical Society of America*, 107(4):1922–1929, 2000.

[86] V. A. Akulichev, V. A. Bulanov, and S. A. Klenin. Acoustic sensing of gas-bubbles in the ocean medium. *Soviet Physics Acoustics-Ussr*, 32(3):177–180, 1986.

[87] N. G. Pace, A. Cowley, and A. M. Campbell. Short pulse acoustic excitation of microbubbles. *Journal of the Acoustical Society of America*, 102(3):1474–1479, 1997.

[88] H. R. Suiter. Pulse length effects on the transmissivity of bubbly water. *Journal of the Acoustical Society of America*, 91(3):1383–1387, 1992.

[89] M. Minnaert. On musical air-bubbles and sounds of running water. *Philisophical Magazine*, 16:235–248, 1933.

[90] P. E. Doust and J. F. Dix. The impact of improved transducer matching and equilisation techniques on the accuracy and validity of underwater measurements. In T. G. Leighton, G. J. Heald, H. Griffiths, and G. Griffiths, editors, *Acoustical Oceanography*, volume 23 of *Proceedings of the Institute of Acoustics*, pages 100–109, 2001.

[91] T. G. Leighton, D. C. Finfer, E. J. Grover, and P. R. White. An acoustical hypothesis for the spiral bubble nets of humpback whales and the implications for whale feeding. *Acoustics Bulletin*, 22(1):17–21, 2007.

[92] C. E. Blenkinsopp and J. R. Chaplin. Void fraction measurements in breaking waves. *Proceedings of the Royal Society a-Mathematical Physical and Engineering Sciences*, 463(2088):3151–3170, 2007.

[93] A. Cartellier and J. L. Achard. Local phase detection probes in fluid fluid 2-phase flows. *Review of Scientific Instruments*, 62(2):279–303, 1991.

[94] G. B. Deane. Sound generation and air entrainment by breaking waves in the surf zone. *Journal of the Acoustical Society of America*, 102(5):2671–2689, 1997.

[95] J. F. Claerbout. *Fundamentals of geophysical data processing*. McGraw-Hill, 1976.

[96] D. M. Farmer, R. C. Teichrob, C. J. Elder, and D. G. Sieberg. Novel acoustical instrumentation for the study of ocean surface processes. In *OCEANS'90. 'Engineering in the Ocean Environment'. Conference Proceedings*, pages 1–17, 1990.

[97] E. Lamarre and W. K. Melville. Sound-speed measurements near the ocean surface. *The Journal of the Acoustical Society of America*, 96:3605, 1994.

[98] W. K. Melville, E. Terrill, and L. Ding. Field measurements of air entrainment by breaking waves. In *Proc. of the Third Int. Symp. on Air-Water Gas Transfer*, pages 285–295, 1995.

[99] S. Stanic, J. Caruthers, R. Goodman, E. Kennedy, and B. Brown. Attenuation measurements across surface-ship wakes and computed bubble distributions and void fractions: A tribute to the contributions by Ralph Goodman on oceanic bubbles. *The Journal of the Acoustical Society of America*, 125:2611, 2009.

[100] E. J. Terrill, W. K. Melville, and D. Stramski. Bubble entrainment by breaking waves and their influence on optical scattering in the upper ocean. *Journal of Geophysical Research*, 106(C8):16815–16823, 2001.

[101] S. Vagle and D. M. Farmer. The measurement of bubble-size distributions by acoustical backscatter. *Journal of Atmospheric and Oceanic Technology*, 9(5):630–644, 1992.

[102] I. N. Didenkulov, S. I. Muyakshin, and D. A. Selivanovsky. Bubble counting in the subsurface ocean layer. In T. G. Leighton, G. J. Heald, H. Griffiths, and G. Griffiths, editors, *Acoustical Oceanography*, volume 23 of *Proceedings of the Institute of Acoustics*, pages 220–226. Bath University Press, 2001.

[103] M. J. Yelland, R. W. Pascal, P. K. Taylor, and B. I. Moat. AutoFlux: an autonomous system for the direct measurement of the air-sea fluxes of CO_2, heat and momentum. *Journal of Operational Oceanography*, 2(1):15–23, 2009.

[104] S. D. Smith. Coefficients for sea-surface wind stress, heat-flux, and

wind profiles as a function of wind-speed and temperature. *Journal of Geophysical Research-Oceans*, 93(C12):15467–15472, 1988.

[105] W. Lauterborn. *Cavitation and Inhomogeneities in Underwater Acoustics*. Springer, Berlin, 1980.

[106] P. L. Atkinson. Effect of air bubble solution on air-sea gas-exchange. *Journal of Geophysical Research*, 78(6):962–968, 1973.

[107] G. A Garrettson. Bubble transport-theory with application to upper ocean. *Journal of Fluid Mechanics*, 59(JUN5):187–206, 1973.

[108] T. G. Leighton, D. C. Finfer, and P. R. White. The problems with acoustics on a small planet. *Icarus*, 193(2):649–652, 2008.

[109] V. G. Levich. *Physico-Chemical Hydrodynamics*. Englewood Cliffs, Prentice Hall, NY, 1962.

[110] R. M. Detsch. Dissolution of 100-1000 μm diameter air bubbles in reagent grade water and seawater. *Journal of Geophysical Research*, 95(C6), 1990.

[111] R. M. Detsch. Small air bubbles in reagent grade water and seawater 1. Rise velocities of 20 to 1000 μm diameter bubbles. *Journal of Geophysical Research*, 96(C5), 1991.

[112] I. A. Harris and R. M. Detsch. Small air bubbles in reagent grade water and seawater: 2. Dissolution of 20-500 μm diameter bubbles at atmospheric pressure. *Journal of Geophysical Research*, 96(C5):8907–8910, 1991.

[113] O. Reynolds. An experimental investigation of the circumstances which determine whether the motion of water shall be direct or sinuous, and of the law of resistance in parallel channels. *Philosophical Transactions of the Royal Society of London*, 174:935–982, 1883.

[114] D. L. Wise and G. Houghton. The diffusion coefficients of ten slighty soluble gases in water at 10-60 °C. *Chem. Eng. Sci.*, 21:999–1010, 1966.

[115] B. Jähne, G. Heinz, and W. Dietrich. Measurement of the diffusion-coefficients of sparingly soluble gases in water. *Journal of Geophysical Research-Oceans*, 92(C10):10767–10776, 1987.

[116] G. B. Deane and M. D. Stokes. Scale dependence of bubble creation mechanisms in breaking waves. *Nature*, 418(6900):839–844, 2002.

[117] J. R. Gemmrich and D. M. Farmer. Near-surface turbulence and thermal structure in a wind-driven sea. *Journal of Physical Oceanography*, 29(3):480–499, 1999.

[118] S. A. Thorpe, T. R. Osborn, D. M. Farmer, and S. Vagle. Bubble clouds and langmuir circulation: observations and models. *Journal of Physical Oceanography*, 33(9):2013–2031, 2003.

[119] S. A. Thorpe. Langmuir circulation. *Annual Review of Fluid Mechanics*, 36:55–79, 2004.

[120] R. Upstill-Goddard *et al.* UK-SOLAS Cruise Report: RRS Discovery Cruise D320, 16 June - 18 July, 2007: DOGEE-II: air-sea gas exchange in the Atlantic Ocean. Technical report, Open Research Group, School of Marine Science and Technology, University of Newcastle upon Tyne, 2007.

[121] S. A. Thorpe, M. S. Cure, A. Graham, and A. J. Hall. Sonar observations of langmuir circulation and estimation of dispersion of floating particles. *Journal of Atmospheric and Oceanic Technology*, 11(5):1273–1294, 1994.

[122] S. Leibovich. The form and dynamics of langmuir circulations. *Annual Review of Fluid Mechanics*, 15:391–427, 1983.

[123] J. A. Smith. Observed growth of langmuir circulation. *Journal of Geophysical Research-Oceans*, 97(C4):5651–5664, 1992.

[124] A. Callaghan, G. de Leeuw, L. Cohen, and C. D. O'Dowd. Relationship of oceanic whitecap coverage to wind speed and wind history. *Geophysical Research Letters*, 35(23):5, 2008.

[125] P. D. Cummings and H. Chanson. An experimental study of individual air bubble entrainment at a planar plunging jet. *Chemical Engineering Research and Design*, 77(A2):159–164, 1999.

[126] D. A. Ervine, E. McKeogh, and E. M. Elsawy. Effect of turbulence intensity on the rate of air entrainment by plunging water jets. *Proceedings of the Institution of Civil Engineers Part 2-Research and Theory*, 69(JUN):425–445, 1980.

[127] D. K. Woolf. Parametrization of gas transfer velocities and sea-state-dependent wave breaking. *Tellus*, 57(2):87–94, 2005.

[128] E. C. Monahan and I. Ó. Muircheartaigh. Optimal power-law description of oceanic whitecap coverage dependence on wind speed. *Journal of Physical Oceanography*, 10(12):2094–2099, 1980.

[129] D. K. Woolf. Bubbles and their role in gas exchange. In P. S. Liss and R. A. Duce, editors, *The Sea Surface and Global Change*, pages 173–205. Cambridge University Press, 1997.

[130] M. V. Trevorrow. The use of moored inverted echo sounders for monitoring meso-zooplankton and fish near the ocean surface. *Canadian Journal of Fisheries and Aquatic Sciences*, 62(5):1004–1018, 2005.

[131] V. C. Anderson. Sound scattering from a fluid sphere. *The Journal of the Acoustical Society of America*, 22:426, 1950.

[132] H. Medwin and colleagues. *Sound in the Sea: From Ocean Acoustics to Acoustical Oceanography*. Cambridge University Press, UK, 2005.